

AD-A007 334

NON-LINEAR FRACTURE MECHANICS: NEW
THEORIES OF SOLID PROPELLANT RESPONSE
AND FRACTURE BEHAVIORS

Kenneth W. Bills, Jr., et al

Aerojet Solid Propulsion Company

Prepared for:

Shock Hydrodynamics, Incorporated
Naval Weapons Center

February 1975

DISTRIBUTED BY:

NTIS

National Technical Information Service
U. S. DEPARTMENT OF COMMERCE

Naval Weapons Center

AN ACTIVITY OF THE NAVAL MATERIAL COMMAND

R. G. Freeman, III, RAdm., USN Commander

G. L. Hollingsworth Technical Director

FOREWORD

Reliability and service life prediction has become an important phase in the research and development efforts of the propulsion community and is vital to the logistics and procurement schedule of missiles. Unfortunately, predictive techniques are very limited and only crude predictions can be made. Several reasons for the backward state of affairs include the statistical nature of the propellant properties, the variability of the environment, the translation of the various environmental factors into engineeringly meaningful loads, and the understanding of the process of propellant failure.

The work described in this report was undertaken under an NWC contract to Aerojet Solid Propulsion Company under Contract Number N00123-72-C-2293 as part of the Naval Air Systems Command Task F31332301, on Mechanical Integrity of Solid Propellant Rocket Motors, to the Naval Weapons Center. The work described in this report also augments and supplements work being performed in a fundamental research under the Naval Ordnance Systems Command Task, R0240201, Physical Chemistry of Filled and Unfilled Elastomers. This work was undertaken in order to develop a better understanding of the failure process in solid rocket motors and to examine methods by which the known nonlinear behavior of propellant in failure can be described. This is important in developing useful engineering tools for the prediction of failure. Under this program a new theory that is potentially useful and amendable to an engineering prediction was developed. In addition a number of nonlinear effects that have an effect upon the predicted stress state, failure propagation were discovered.

This report is a facsimile of the report prepared by Aerojet Solid Propulsion Company.

Released by
WILLIAM S. McEWAN, *Head*
Chemistry Division
6 August 1974

Under authority of
HUGH W. HUNTER, *Head*
Research Department

NWC Technical Publication 5684

Published by
Collation
First printing

3181	ESTABLISHMENT/AVAILABILITY CODES	Instruction	UNCLASIFIED	ACQUISITION FOR
AVAIL. S&C/CF SERIAL			Write Section	
			Ext. Section	
			<input type="checkbox"/>	
			<input type="checkbox"/>	
			<input checked="" type="checkbox"/>	

Research Department
Cover, 75 leaves
255 unnumbered copies

UNCLASSIFIED

SECURITY CLASSIFICATION OF THIS PAGE(When Data Entered)

(U) *Non-linear Fracture Mechanics: New Theories of Solid Propellant Response and Fracture Behaviors*, by Kenneth W. Bills, Jr., Aerojet Solid Propulsion Company and Paul J. Blatz, Whittaker Corporation. China Lake, Calif., Naval Weapons Center, February 1975. 150 pp. (NWC TP 5684, publication UNCLASSIFIED.)

(U) Non-linear fracture mechanics is a newly developing analytical method for the treatment of fracture behaviors in composite solid propellants. The work presented here was designed to show the need for these concepts and the material behaviors that must be taken into account by the theory.

(U) An empirically derived relation forms the fundamental point of departure for the non-linear fracture criterion. In addition, a non-linear strain energy function was investigated as the initial effort in developing the required analytical relations.

16/ UNCLASSIFIED

SECURITY CLASSIFICATION OF THIS PAGE(When Data Entered)

PREFACE

This report summarizes the experimental efforts conducted by Mr. Kenneth W. Bills, Jr. at the Aerojet Solid Propulsion Company and the theoretical studies of Dr. Paul J. Blatz at Shock Hydrodynamics.

We wish to express our deep appreciation to Dr. Arnold Adicoff, the Navy Project Engineer, for his kind support and infinite patience.

In addition, the many long hours given by Mr. Chris Fulton of Shock Hydrodynamics and Mrs. Phyllis Uyemura of Aerojet Solid Propulsion Company are gratefully acknowledged.

TABLE OF CONTENTS

	<u>Page No.</u>
INTRODUCTION	1
SUMMARY	2
New Theory of Propellant Response Behavior	6
CHALLENGING GRIFFITH	7
Mixed Boundary Problem	7
Effect of Strain Rate at the Crack Tip	11
SUPPORTING GRIFFITH	23
Strength-Modulus Relation for Creep-to-Failure Data	23
Tests of Crack Depth Dependence	29
Conclusions	33
FACTORS TO BE TAKEN INTO ACCOUNT IN DEVELOPING A FRACTURE THEORY	35
Basic Failure Mechanisms	35
Effect of Dewetting Upon the Criterion of Failure	51
Loading Path Dependence	55
Independence of Filler Content	62
Strong Time Dependence	62
Characterization of Material Fracture	66
Dependence of Low-Strain Moduli on Dewetting	71
THEORY - INTRODUCTION	73
Basic Response Processes	73
Technical Background	73

TABLE OF CONTENTS (CONT.)

	<u>Page No.</u>
ANALYTICAL DEVELOPMENT	77
Generating the Physical Model	77
Choosing the Strain Energy Function	77
Parameter Determination	79
Stress-Strain Relations	84
EXPERIMENTAL EVALUATION OF CHARACTERIZATION PARAMETERS	86
Atmospheric Pressure Tests	87
Superimposed Hydrostatic Pressure Tests	98
MODIFICATION OF THE THEORY	103
REFERENCES	R-1
APPENDIX A - Viscoelastic Fracture of Solid Propellant	A-1
APPENDIX B - Effects of Propellant Dewetting	B-1

LIST OF FIGURES

<u>Figure No.</u>		<u>Page No.</u>
1	Griffith Crack Specimen	8
2	Effect of Loading History Upon the Shape of the Crack Tip	9
3	Loading Traces for Crack Tip Tests on Rubber Dental Dam	10
4	Tear Contours in a Notched Strip Biaxial Specimen of Polyurethane Propellant at -65°F	12
5	Effect of Rate of Loading Upon Crack Tip Geometry	13
6	Mid-Section of Double-Notched Tensile Specimen	14
7	Strength vs Crack Depth in ANB-3066 Propellant at 110°F	16
8	Strength vs Crack Depth in ANB-3066 Propellant at 77°F	17
9	Strength vs Crack Depth in ANB-3066 Propellant at 0°F	18
10	Strength vs Crack Depth in ANB-3066 Propellant at -40°F	19
11	Strength vs Crack Depth in ANB-3066 Propellant at -110°F	20
12	Strength vs Crack Depth in ANB-3066 Propellant at Various Test Temperatures	21
13	Effect of Superimposed Pressure on Constant Stress to Failure Data for a CTPB Propellant	24
14	Normalized Failure Stress and Modulus Curves for CTPB Propellant	26
15	Superposition of Normalized Moduli and Failure Stress Data	28
16	Results of Constant Load-to-Failure Tests of Specimens Notched on One Side	30

LIST OF FIGURES (CONT.)

<u>Figure No.</u>		<u>Page No.</u>
17	Fracture Initiation Data for Double Notched Specimens of ANB-3066 Propellant	32
18	Circular Shaped Bubbles Created from Failures in Hydrostatic Tension	36
19	Oval Shaped Bubbles Created from Failures in Combined Tension and Shear	37
20	Oval Shaped Bubbles Created Near the End of a Glass-Encased Propellant Grain	38
21	Fernlike Pattern of Propagating Interface Cracks	39
22	Dense Fernlike Pattern of Interface Cracks	40
23	Photomicrograph of a Cross-Section of ANP-2915-5 Polyurethane Propellant	42
24	Schematic of Binder Ligament Between Two Vacuoles	43
25	Jagged Cracks in a Grain Fin Slot	44
26	Multiple Jagged Cracks in a 5" Subscale Grain	45
27	Non-Linear Propagation of Radial Cracks	46
28	Photoelastic Stress Patterns in Stretched Binder Specimens with Crack	48
29	Deviation of Growing Crack from Axis of Symmetry	49
30	Long Crack Formed at an Intermediate Propagation Rate	50
31	Dewetting in Uniaxial Tension	52
32	Dewetting Behavior Under Equal Biaxial Tension	53
33	Schematic Representation of Dewetting Bands in a Biaxially Strained Specimen	54

LIST OF FIGURES (CONT.)

<u>Figure No.</u>		<u>Page No.</u>
34	Dewetting in a Notched Specimen Undergoing Shear Deformation	56
35	Schematic Representation of Path Dependency	57
36	Bauschinger Effect in Strip-Biaxial Tear Specimen	59
37	Effect of Pre-Strain on the Failure Envelope for a CTPB Propellant Tested Under 800 psi Pressure at -75°F	61
38	Master Plot of the Stress-at-Break for an HTPB Polymer - Equivalents Ratio 60/40	63
39	Master Plots of the Stress-at-Break for an HTPB Polymer - Equivalents Ratio 70/30	64
40	Master Plots of the Stress-at-Break for an HTPB Polymer - Equivalents Ratio 80/20	65
41	Strength of Unextracted SBR at an Extension Rate of 5 min ⁻¹	67
42	Shape of the Crack Tip at Failure Initiation for a Polyurethane Propellant at -65°F	68
43	Shape of Crack Where the Initial Razor Cut was Slightly Canted	69
44	Failure Initiation Ahead of the Crack Tip in a Polyurethane Propellant at -65°F	70
45	Stress-Strain Curve for a Polyurethane Binder Filled with 80 wt. % Glass Beads	72
46	Fracture-Controlled Dilatation of Aerojet CTPB Propellant	88
47	Fracture-Controlled Dilatation of Aerojet CTPB Propellant	89
48	Fracture-Controlled Dilatation of Aerojet CTPB Propellant	90

LIST OF FIGURES (CONT.)

<u>Figure No.</u>		<u>Page No.</u>
49	Fracture-Controlled Dilatation of Aerojet CTPB Propellant	91
50	Fracture-Controlled Dilatation of Aerojet CTPB Propellant	92
51	Fracture-Controlled Simple Tensile Behavior of Aerojet CTPB Propellant	93
52	Fracture-Controlled Simple Tensile Behavior of Aerojet CTPB Propellant	94
53	Fracture-Controlled Simple Tensile Behavior of Aerojet CTPB Propellant	95
54	Fracture-Controlled Simple Tensile Behavior of Aerojet CTPB Propellant	96
55	Fracture-Controlled Simple Tensile Behavior of Aerojet CTPB Propellant	97
56	Fracture-Controlled Dilatation of Aerojet CTPB Propellant Under Superimposed Hydrostatic Pressure	100
57	Fracture-Controlled Dilatation of Aerojet CTPB Propellant Under Superimposed Hydrostatic Pressure	101
58	Fracture-Controlled Dilatation of Aerojet CTPB Propellant Under Superimposed Hydrostatic Pressure	102
59	Fracture-Controlled Dilatation of Aerojet CTPB Propellant	104

LIST OF TABLES

<u>Table No.</u>		<u>Page No.</u>
I	Bauschinger Effect in Tear Specimens of a CTPB Propellant at 77°F	60
II	Parameter Evaluations from Tests at 77°F and 0 psig	87
III	Parameter Evaluations from Tests at 77°F and 0 psig	98

LIST OF SYMBOLS

a	Radius of rigid filler particle
a_p	The time-pressure shift function
a_T	The time-temperature shift function
A	Constant
A_0	Original specimen cross-sectional area
A_n	Net cross-sectional area of specimen at the notch
b	Radius of spherical unit cell
B	Constant
C	Crack length
E	Elastic tensile modulus
E_e	Equilibrium relaxation modulus
E_g	Glassy modulus
$E(\xi)$	Relaxation modulus
$f(\xi_f)$	An unspecified function of the time to failure under constant stress
$g(\xi_f)$	An unspecified function of the time to failure under constant stress
G	Shear modulus
G_e	Effective shear modulus after vacuole formation
$h(\tau)$	Is a distribution function of relaxation times
I_ϵ	The first strain invariant
II_ϵ	The second strain invariant
III_ϵ	The third strain invariant

LIST OF SYMBOLS (CONT.)

J	Dilatation ratio
k	Proportionality constant
K	Bulk modulus
K_e	Effective bulk modulus after vacuole formation
m	A constant defining interactions between adjacent cells
$M =$	$\frac{2}{3} \tau_{vf} / (hGmk^{1/m})$
n	Constant that measures strain hardening or softening
\dot{J}	Power input to sample
P	Applied hydrostatic pressure
q	An empirical shift constant
S	Mechanically applied unit force on uniaxial tensile specimen
U_1	The total strain energy
U_3	The total surface energy
V^+	Volume of the undeformed specimen
W	Strain energy density
α	A constant defining the dependence of force-pressure coefficient upon strain
α	Subscripts defining directions of maximum principal strain
β	An exponent that determines the measure of dilatation
γ	Measure of porosity due to dewetting
Γ	Specific surface energy per unit area of new surface
δ	The fraction of unbonded area around filler particle
Δ	Measure of relative strain dilatation

LIST OF SYMBOLS (CONT.)

ϵ	Strain
$\dot{\epsilon}_a$	Overall apparent strain rate on test specimen
$\dot{\epsilon}_c$	Effective strain at the crack tip
ϵ_α	Principal strains
λ	Stretch ratio measured in testing
λ_α	Principal stretch ratios
v_f	Volume fraction of filler particles
ξ	Reduced time of the test
ξ_f	Reduced time to failure under constant stress
σ	Radius of curvature at the crack tip
σ_g	Glassy strength of the material
σ_{max}	Maximum stress at the crack tip
σ_0	Stress applied along the outer boundaries of a test specimen
$\bar{\sigma}_\alpha$	Principal Piola stress
σ_α	Principal Cauchy stress
$\sigma(\xi_f)$	Applied constant stress on specimen
σ_∞	Stress below which failure will not occur
τ	Is a relaxation time
ϕ	The constant area between the filler particle and the binder matrix, whether bonded or unbonded

INTRODUCTION

Non-linear fracture mechanics* is a newly developing analytical method for the treatment of fracture behaviors in composite solid propellants. It stands in contrast to the well known linear-elastic fracture mechanics of Griffith (2) and the linear-viscoelastic fracture mechanics of Williams (3). These latter theories assume progressive fracturing of a single crack, with small strains in the body away from the crack tip. The non-linear theory includes non-linear viscoelasticity with its permanent memory effects, non-progressive fracturing of cracks, and finite strains away from the crack tip.

The study presented here was designed to illustrate the inadequacies of the linear theories and the fundamental requirements of the non-linear one. An empirically derived relation forms the fundamental point of departure for the non-linear fracture criterion. In addition, a non-linear strain energy function was investigated as the initial effort in developing the required analytical relations.

The objectives of the following report are:

1. To define the key characteristics in the fracture processes of solid propellants.
2. To summarize existing mathematical concepts for non-linear material response and failure.
3. To make recommendation for future studies.

*Suggested as a contrast to G. R. Irwin's article, "Linear Fracture Mechanics in Relation to Visco-elastic Materials" (1).

SUMMARY

The empirical observations and the practical relationships derived from them represent the majority of the report. The last part of the report covers a newly developed theory of propellant response.

Empirical Fracture Studies

Fracture initiation and the trajectory of crack propagation in solid propellants are important to the prediction of motor service life (4 and 5). However, past experience with solid propellants has given ample evidence that solid propellants do not follow the classical relations. Partially recognizing this, Fulbright and Miller (6) have recommended the dissection of motors to complete their failure analyses.

At ASPC, the first challenge to the linear-elastic concept (Griffith) involved a problem of mixed boundaries. Here, the classical criteria require a unique relationship between displacements of the crack boundary and those at the specimen boundary. But, it is shown that the shape of the crack tip has a very strong dependence upon the past loading history of the test specimen. Thus, there is not a unique relation between the displacements at the crack and the specimen boundaries.

As an added demonstration of this effect, it is shown that notching a uniaxial tensile specimen may actually increase its apparent strength. This effect is attributed to the increased strain rate at the crack tip.

In a later section of this report, it is shown that a major modification of the classical criterion can be used to fit solid propellant fractures. The observed failure relation is:

$$\sigma(\xi_f) - \sigma_\infty = \frac{k\Gamma^{1/2}}{c^{1/2}} [E(\xi_f/q) - E_e]^{1/2} \quad (1)$$

This relation holds for creep-to-failure tests and states that the maximum principal stress difference, $\sigma(\xi_f) - \sigma_\infty$, is proportional to the square root of the modulus difference, $[E(\xi_f/q) - E_e]^{1/2}$. Equation (1) reduces to Griffith's criterion when the propellant is glassy.

The free surface energy, Γ , is a constant that holds over the entire range from glassy to rubbery behaviors.

A unique feature of Equation (1) is the constant, q , that is used to define the "effective-time" of the relaxation modulus, $E(\xi_f/q)$. This constant causes the entire plot of the relaxation modulus to be shifted along the time axis.

All modes of testing and past loading histories can be made to fit Equation (1) through either linear (7 to 10) or non-linear (11 and 12) cumulative damage analyses; whichever applies to the material behavior.

Thus, Equation (1), combined with cumulative damage analyses, provides an empirical basis for the required non-linear fracture criterion. Note: this relation is not considered to be the final one, but it will be employed until a better criterion is established.

Verifications of Equation (1) involved constant load and constant rate failure testing of specimen with various crack depths, C. Both tests gave the required agreements, although the constant load tests evinced specimen distortions at the higher loads and crack depths.

A number of factors must be taken into account in developing the relevant non-linear fracture criterion. These are listed in a special section of this report.

The basic mechanism of fracture in propellant binders seems to be initiation in tension, with propagation occurring under the peeling action of combined tensile and shear deformations.

Crack propagation mechanisms in propellants vary considerably on going from low to high rates. At low propagation rates a great number of initiation sites are generated, with cracks emanating from each of them. However, unlike the classical process, the cracks deviate from their expected paths of propagation following curved trajectories. As the cracks turn, the rate of tearing diminishes and the crack eventually stops. Later, the individual cracks are joined (rather raggedly) by separate tearing actions between them, leading to an overall gross crack. A similar process, but with special differences, also occurs at the propellant/liner bond interface.

At high propagation rates, where the propellant is glassy, the classical fracture processes are obtained.

Thus, the rates of crack propagation determine the number of initiation sites, the extent of energy dissipation, the trajectory of the moving crack tip, and the appearance of the fractured surfaces.

A primary point, of relevance to Equation (1), is the observation that dewetting effects define the mode of propellant fractures. It is observed that when at least one loading axis undergoes tensile deformation the failure mode will be a uniaxial one and will follow a maximum principal stress failure criterion.

Even shear failures were found to be accompanied by dewetting effects of the type seen in uniaxial tensile testing. The dewetting patterns were observed to be rotated with respect to the specimen axis, as expected.

Loading-path dependence, was demonstrated for three different loading histories. One involved thermal-strain paths and the remaining two were variations of the Bauschinger effect (14).

In the first case, it is shown that different failure elongations will be obtained depending upon the order of straining the specimen and varying the environmental temperature.

The Bauschinger effect entails a temporary shift of the stress-strain coordinate axes. In propellants this "temporary set" is readily accomplished. All that needs to be done is to hold the specimen under a deformation for a period of time. This produces marked stress relaxation effects that are seen as major shifts in the coordinate stress-strain axes.

The first tests measured the effects of putting a specimen into 5% compressive strain prior to crack-failure testing, in notched strip-biaxial tensile specimens. The previous load history gave a 24% decrease in the failure deformation and a 15% decrease in the average failure stress.

The second set of tests involved a pre-loading in stress relaxation under a 10% tensile strain. Then, without allowing recovery, the specimens were tested-to-failure under a superimposed pressure. The resulting improvement in the failure envelope showed that the shift in the strain coordinate was considerable, up to the full-extent of the pre-strain.

This path dependency of solid propellants obviously necessitates stress-strain constitutive relations that: (1) Have a permanent memory; (2) allow for propellant dewetting; and (3) include finite deformations. The theoretical studies of Blatz are included in this report as one approach to the required response analyses. A separate approach by Farris (12 and 13) is directed at the same goal.

The importance of dewetting to solid propellant failure mechanisms has been considered by Lindsey (15), Robinson (16) and Knauss (17). Although we agree in principle, we find that the exact role of dewetting is not clear. This is best seen from a series of tests with several different HTPB binder formulations. It was found that the tensile strength was independent of filler content; at least, for filler fractions varying from 50 to 76.3 vol. %. A few data points indicate that this independence of filler-content may extend to the unfilled binder.

We also considered binder crosslinking and showed that propellant binders form a special class that distinguishes them from the well known elastomers. In conventional rubbers the crosslinking is much greater than that used in solid propellant binders. The works of Bueche and Dudek (18, 19 and 20) have shown that failure in highly crosslinked elastomers exhibits little time-dependence, while the very lightly crosslinked propellant binders should exhibit considerable time, or strain rate, dependence. Similarly, their data suggest that propellant failure behaviors should be nearly independent of binder crosslinking.

In the characterization of solid propellant fracture processes we find a number of difficulties. It is shown, for example, that fracture initiation testing can be associated with a large radius of curvature at the crack tip. This becomes great enough in some cases to reduce the local stress field, causing failure initiation to occur at a point away from the crack tip.

Equation (1) requires a careful evaluation of the relaxation moduli. But, as noted by Francis (21), the relaxation modulus is strongly affected by the strain level. Also, Adicoff and Lepie (22) showed that dewetting under strain causes the propellant to depart from thermorheological simplicity.

Thus, we concluded that the relaxation moduli be obtained at the lowest possible strain levels (i.e. below about 0.25%). Here the moduli values are the largest and the effects noted by Adicoff and Lepie are minimized.

New Theory of Propellant Response Behavior

A non-linear strain energy function has been proposed to represent both the response behavior and fracture behavior of a CTPB propellant in various stress fields and under superimposed hydrostatic pressures. The strain energy function includes two features which are novel and useful. First, a generalized strain measure proposed by Seth (22) is used to represent elastic non-linearity. Secondly, to account for load-unload hysteresis, the elastic parameters have been allowed to depend upon an additional field variable, which is the area fraction of dewetted solids; this field variable is controlled by the Griffith power balance. The theory in its present form contains five parameters.

The theory has been checked on Aerojet propellant, on simple tensile data at 77°F from 0.05 min⁻¹ to 1.25 min⁻¹ and under superimposed pressures from 0 psig to 500 psig. The theory provides excellent correlation with the loading data.

In a general homogeneous stress field, as experienced in a motor, the dewetting field will be non-uniform and the extent of dewetting will depend on the entire load-unload history. The ultimate goal of this program is to develop a finite element program, into which is coupled the Griffith criterion, and which will predict the instantaneous state of dewetting of a rocket motor at any time during its thermomechanical history.

CHALLENGING GRIFFITH

There seem to be many circumstances where the Griffith Failure Criterion is not obeyed by solid propellants. The following discussion considers only one of these circumstances; namely, the mixed boundary assumption of the Griffith criterion. A particular example of the mixed boundary problem is shown by the effects of strain rate at the crack tip.

Mixed Boundary Problem

One of the fundamental features of Griffith's Criterion (2) is the definition of the conditions of stress, stress intensity, or energy that exists at the crack tip. An unobtrusive assumption of these analyses is that there is a unique relation between the geometry of the crack tip and the loadings imposed on the boundaries of the overall specimen. Our experience with rubbers and solid propellants clearly shows this to be a mixed boundary problem where the loadings on the crack boundary are not uniquely defined by those on the exterior.

This problem may be simply reviewed in terms of the Griffith model shown in Figure 1. Here, a crack of length $2C$ is included in a simple tensile specimen that is loaded only along its upper and lower boundaries.

The Griffith criterion specifically defines the maximum stress at the crack tip, σ_{\max} , in terms of σ_0 as follows:

$$\sigma_{\max} = \left(\sigma_0 \left[1 + 2 \sqrt{\frac{E}{\rho}} \right] \right) \quad (2)$$

Where ρ is the radius of the crack tip

σ_0 is the stress applied along the boundaries of the uniaxial specimen

Variations in ρ form the basis for the non-singular boundary relationships mentioned above.

Since ρ is usually an experimentally inaccessible quantity, the theoreticians have generally used classical elasticity, or viscoelasticity, to define the local strain energy. This approach has the built-in assumption that there is a singular relation between ρ and the boundary displacements of the test specimen.

Figure 2 contains photographs of a cut in a thin piece of rubber dental dam. Figure 2a shows the specimen after it had been loaded and a notch cut into it (note: the crack spontaneously arrested itself after propagating a short distance). Figure 2b is a photograph of the crack after the specimen had been unloaded and reloaded to approximately the same load level as seen the first time, Figure 3. The very large change in the radius of the crack tip, ρ , is clearly evident from the two photographs.

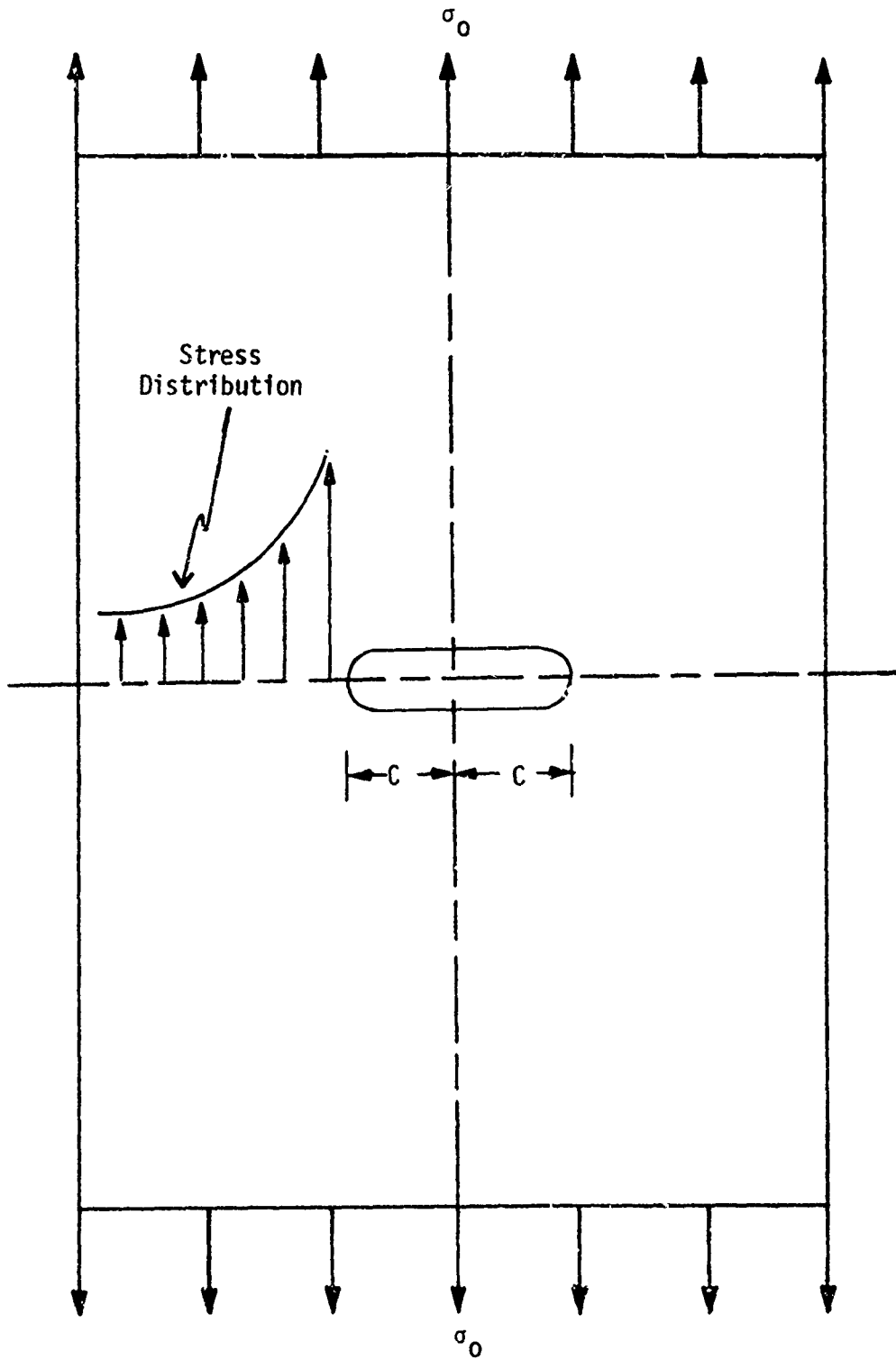
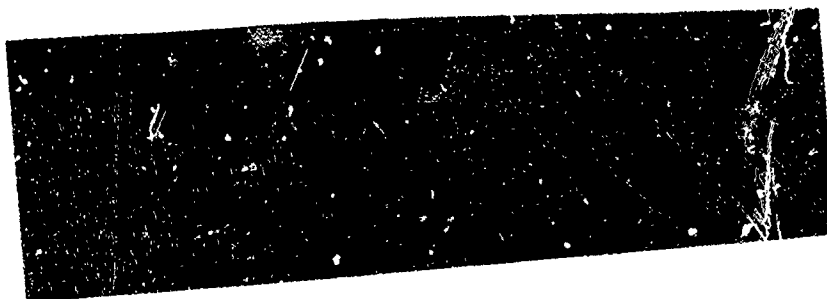
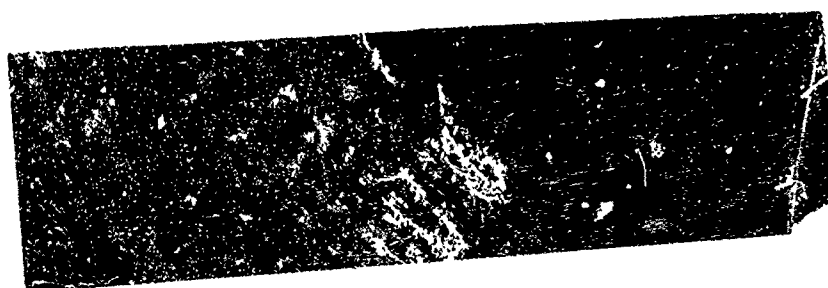


Figure 1. Griffith Crack Specimen



a. Cut while under load.



b. Specimen after unloading and reloading.

Figure 2. Effect of Loading History Upon the Shape of the Crack Tip

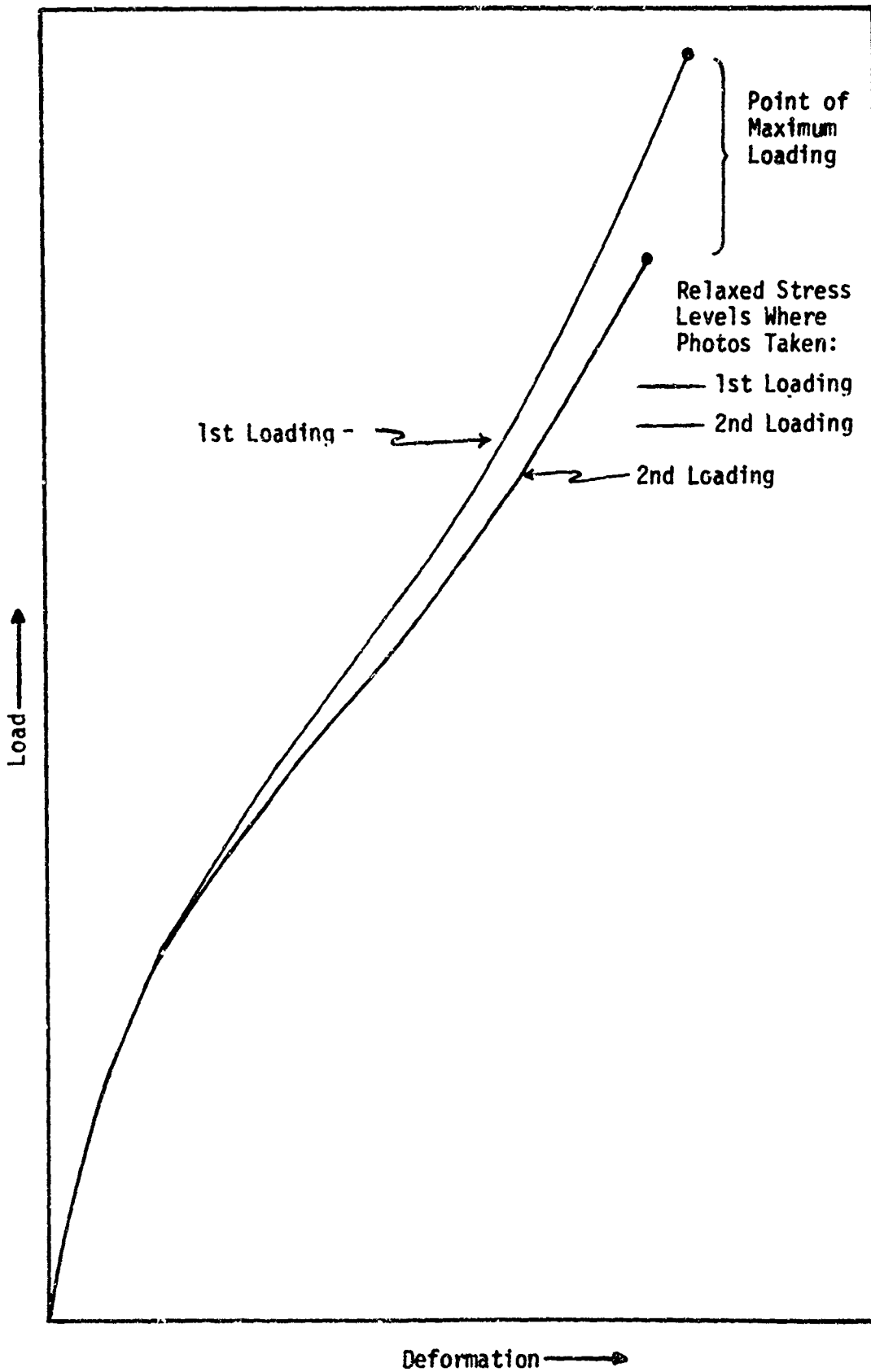


Figure 3. Loading Traces for Crack Tip Tests on Rubber Dental Dam

This behavior is confirmed for solid propellants as shown in Figure 4. This test was performed at -65°F and involves a specimen that was repeatedly loaded to cause fatigue. Figure 4a shows the virgin specimen at the point of failure initiation. Figure 4b shows the same conditions for the fatigued specimen.

Andrews (24) was the first to observe this mixed boundary effect.

Bills (25) made the additional observation that the rate of the second loading was the primary factor determining the shape of the reloaded crack, Figure 5. A low rate of loading is required to produce the large crack tip radius noted above, see Figure 5b. But, as Bills observed, the unloaded, pre-notched rubber specimen has a very sharp crack tip, Figure 5a. Thus, a very high rate of loading should preserve the sharp crack; which it does, Figure 5c. In fact, rapid pulling of the sharp crack was observed to reduce rubber specimen strength by about a factor of 10.

Another effect of strain rate upon crack tip geometry and specimen strength (in a solid propellant) is clearly demonstrated next.

Effect of Strain Rate at the Crack Tip

The mixed boundary effect was demonstrated in ANB-3066 propellant (CTPB). The double-notched tensile specimen, shown in Figure 6, was used; the notches being razor blade cuts made in a single pass (to prevent double-cutting and rounding of the crack tip). Five different notch depths were used: 0, 1/32, 1/16, 3/32 and 1/8 in.

The tests were conducted at a low crosshead rate, so that the very sharp notch effect shown in Figure 4a was not expected. Instead, reduced cross-section should experience higher strain rates with a concomitant increase in the apparent strength (based on the net specimen cross-section). The overall specimen had a width of 0.5 in. Hence, the maximum crack depth of 1/8 in. reduced the specimen to 0.25 in., or half its original cross-section. All of the failure data are reported in terms of the stress-at-rupture, which is defined in terms of the net cross-sectional area.

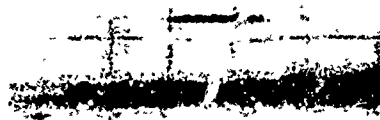
The local strain rate at the crack tip, $\dot{\epsilon}_c$, may be crudely estimated as follows:

$$\dot{\epsilon}_c \approx \frac{A_0}{A_n} \dot{\epsilon}_a \quad (2)$$

Where $\dot{\epsilon}_a$ is the overall apparent strain rate on the specimen

A_0 is the original cross-sectional area of the specimen

A_n is the net cross-section at the notch

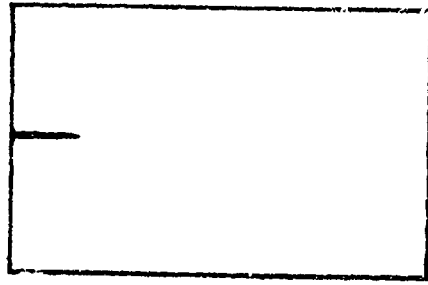


a. Initial Tear Contour, Displacement 0.07 in.

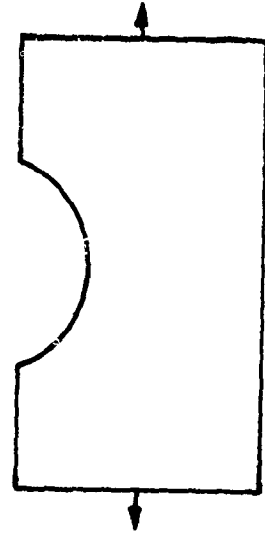


b. Tear Contour after Fatigue, Displacement 0.30 in.

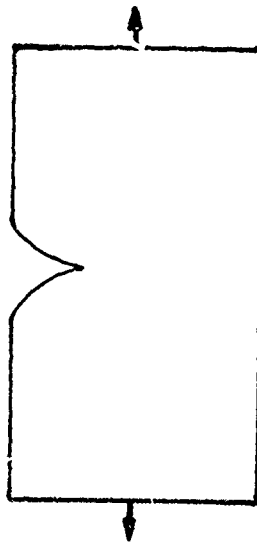
Figure 4. Tear Contours in a Notched Strip Biaxial Specimen of Polyurethane Propellant at -65°F



a. Unloaded specimen with cut on one side.



b. Shape of cut after a low rate of loading.



c. Shape of tear tip upon rapid loading.

Figure 5. Effect of Rate of Loading Upon Crack Tip Geometry

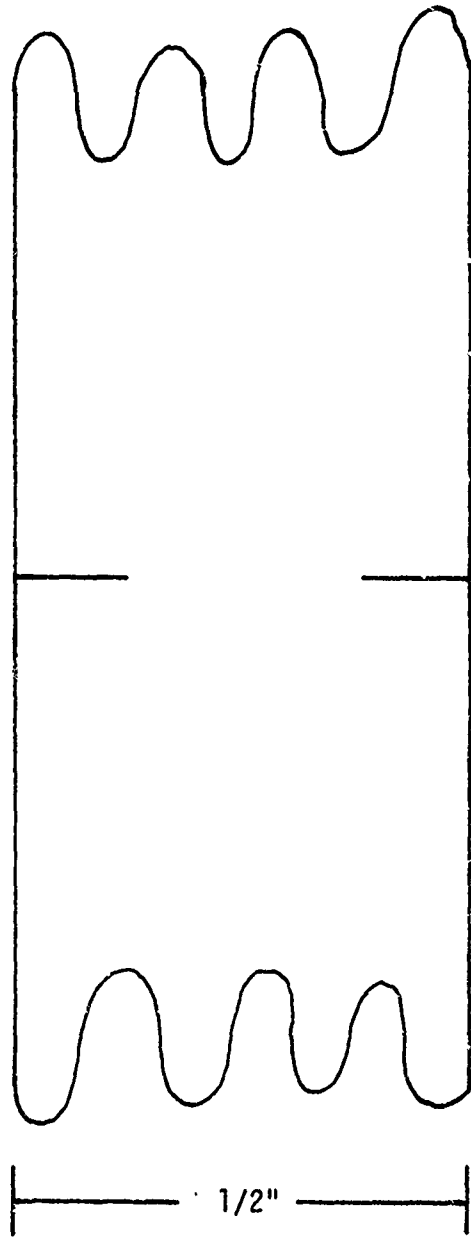


Figure 6. Mid-Section of Double-Notched Tensile Specimen

Thus, we estimate that the notched specimens should experience changes in strain rate up to a factor of about 2, for the 1/8 in. notch depth. At 77° and 110°F, the strain rate effects are quite small, so we expected little sensitivity to crack depth. Actually, the 110°F data gave the expected results (Figure 7), while the 77°F tests showed more sensitivity to crack depth at 1/8 in. than was predicted, Figure 8.

The 0° and -40°F test results were quite sensitive to the crack depth, as expected; Figures 9 and 10. Similarly, at -110°F little sensitivity to strain rate was expected since this temperature is near the glassy temperature of the propellant; none was observed, Figure 11.

A large statistical variation was obtained in the -110°F testing, however. This is to be expected since glassy materials are more notch-sensitive; and our methods of preparation could not be precise. This becomes abundantly clear when one considers that the razor blades must drive some of the oxidizer particles ahead of it and into the cuts making them more ragged, and effectively deeper, than intended.

Variations in the test data may also arise from material property gradients in the carton of propellant, from which the specimens were cut.

Figure 12 was prepared to summarize the previous data. It should be clear from these results that the crack merely acts like a strain rate magnifier, as previously stated.

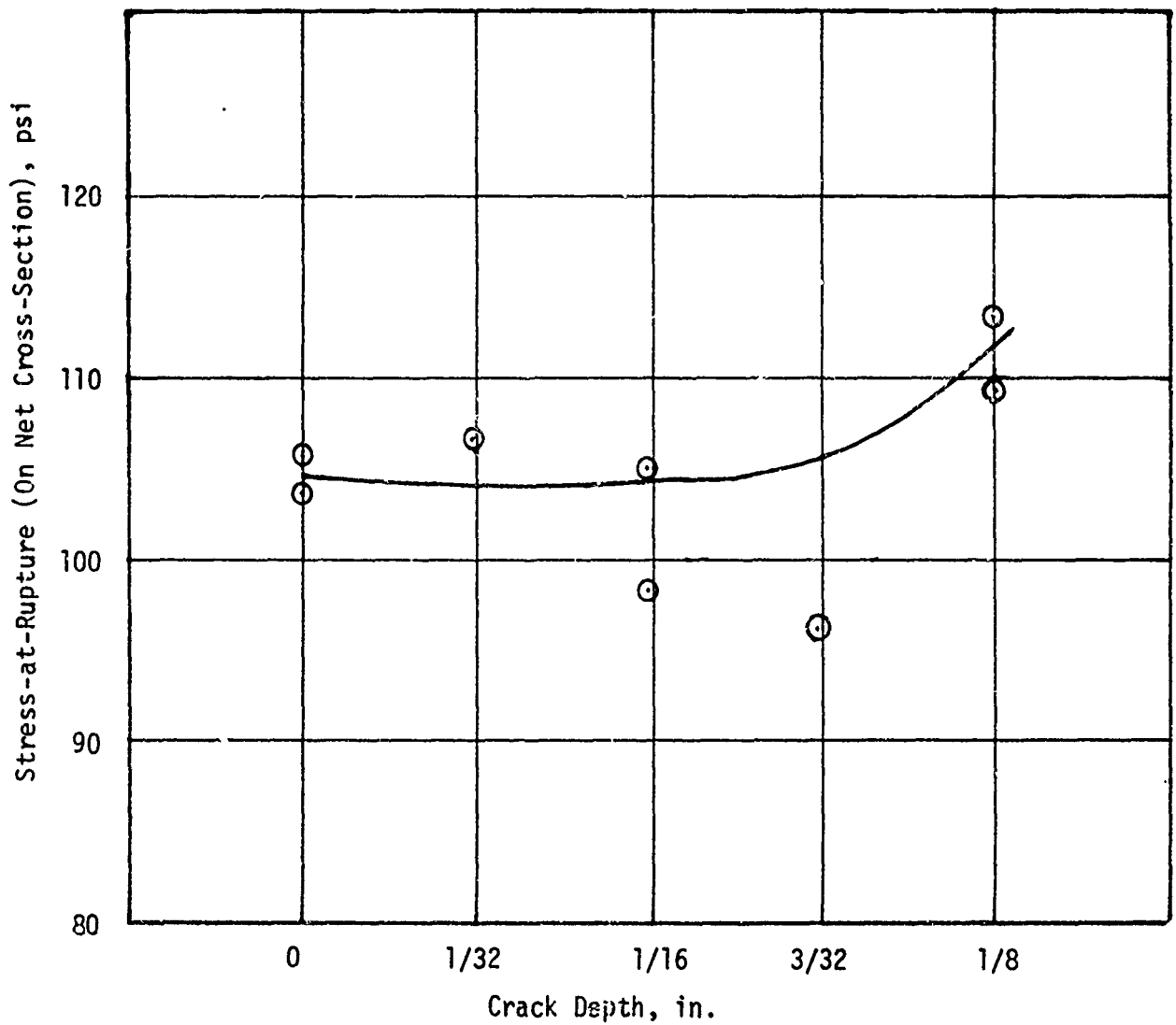


Figure 7. Strength vs Crack Depth in ANB-3066
Propellant at 110°F
(Double-Notched Specimens)

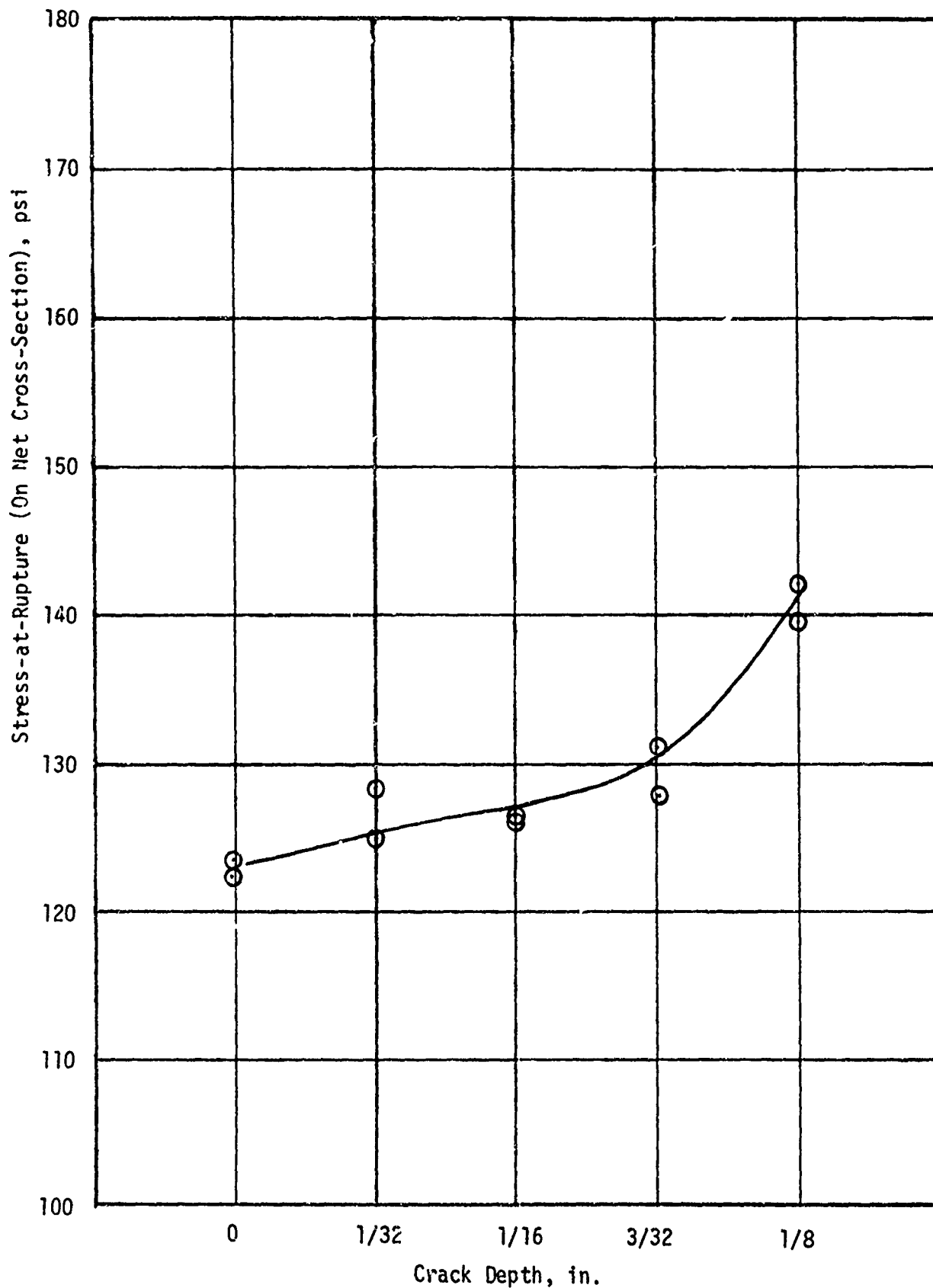


Figure 8. Strength vs Crack Depth in ANB-3066 Propellant at 77°F (Double-Notched Specimens)

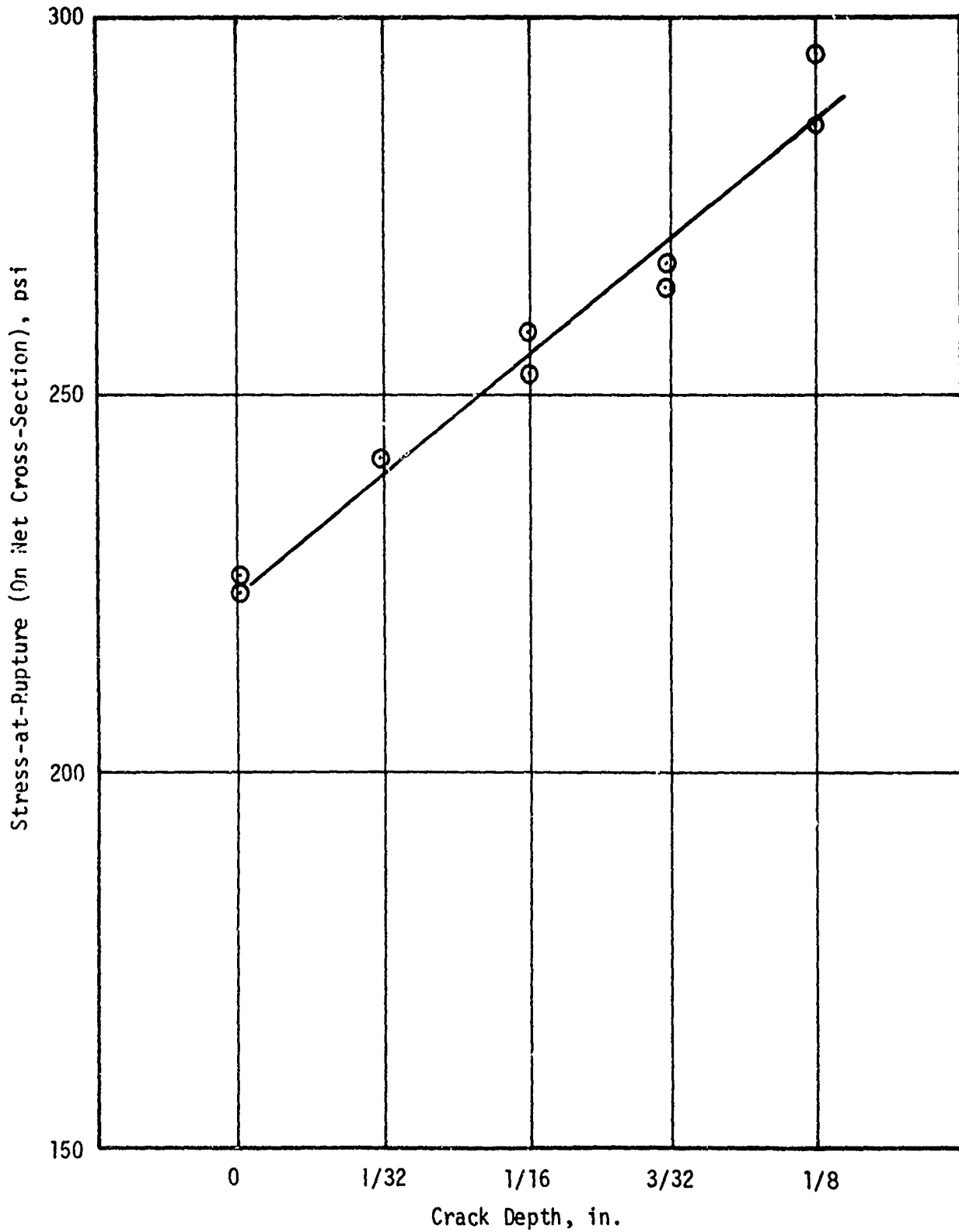


Figure 9. Strength vs Crack Depth in ANB-3066 Propellant at 0°F (Double-Notched Specimens)

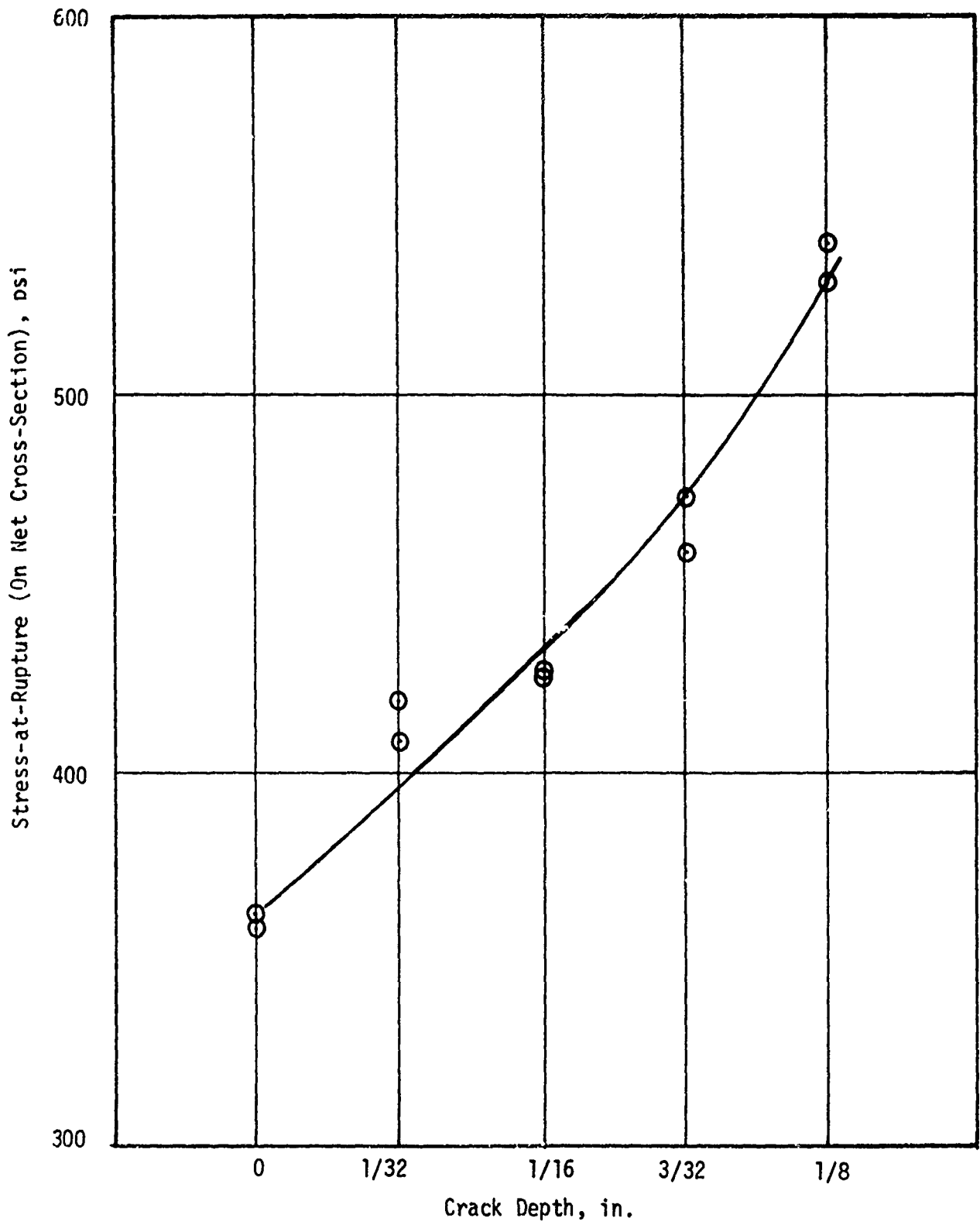


Figure 10. Strength vs Crack Depth in ANB-3066 Propellant at -40°F (Double-Notched Specimens)

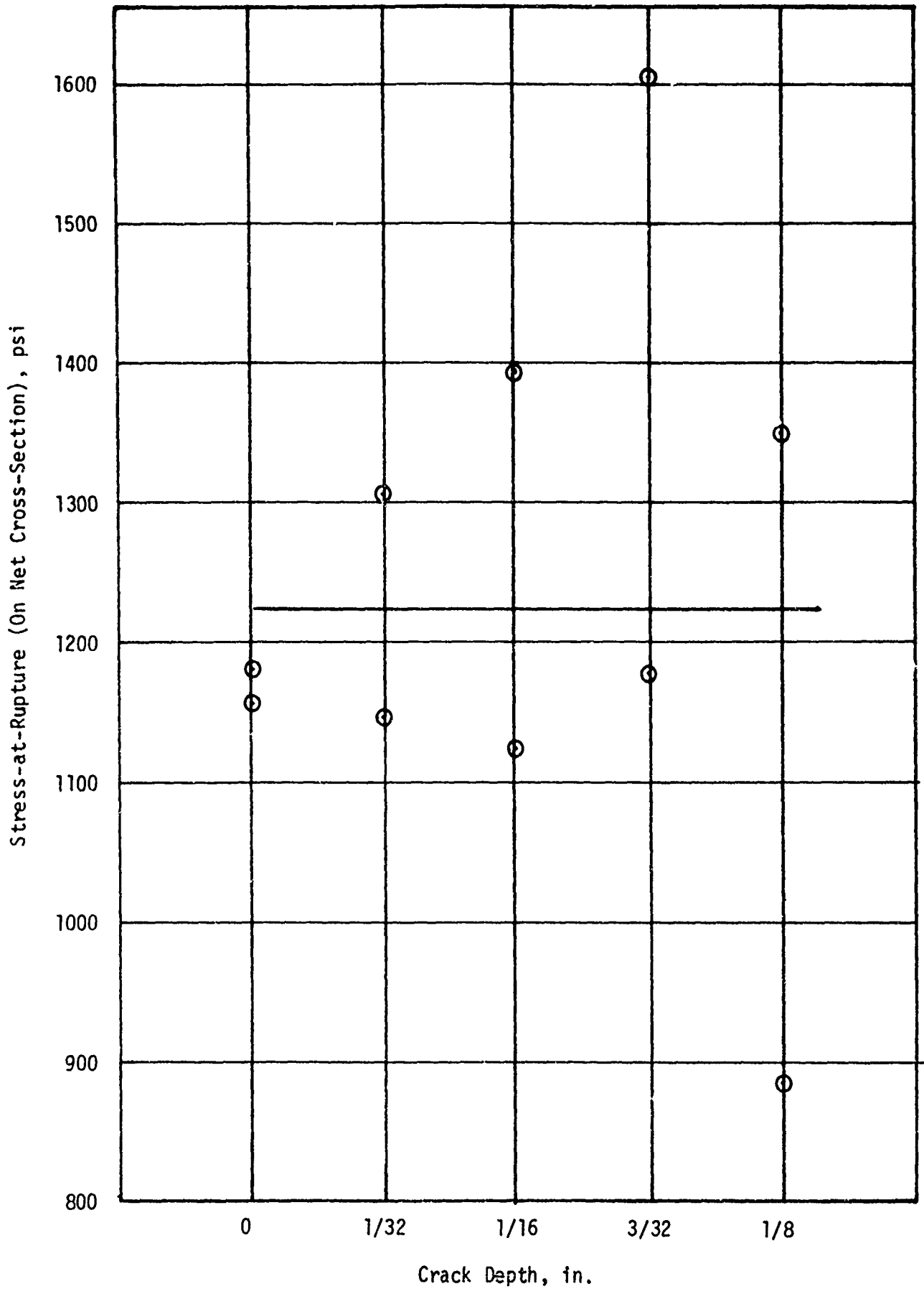


Figure 11. Strength vs Crack Depth in ANB-3066 Propellant at -110°F (Double-Notched Specimens)

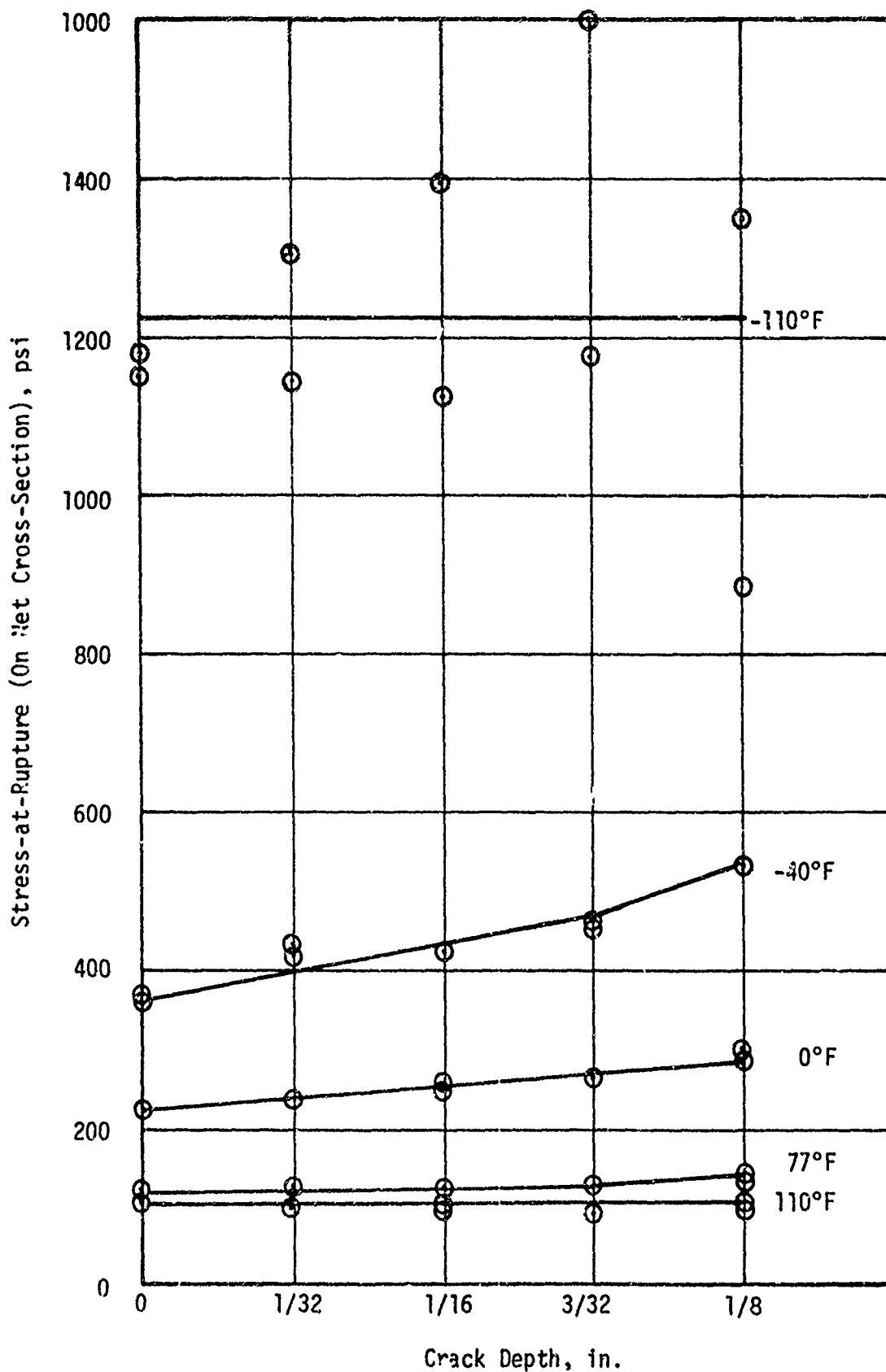


Figure 12. Strength vs Crack Depth in ANB-3066 Propellant at Various Test Temperatures (Double-Notched Specimens)

SUPPORTING GRIFFITH

The negative impressions given in the previous section must be dispelled somewhat, since there are conditions where a Griffith-type failure criterion seem to apply to propellant failure data.

A completely empirical failure criterion, that reduces to the Griffith relation when the propellant is glassy, is described next. Then, using that relation the effects of crack depth in propellant specimens are considered.

Strength-Modulus Relation for Creep-to-Failure Data

In the course of a number of Navy-Sponsored programs (7 to 11), Bills demonstrated that propellants seem to follow a maximum principal stress failure criterion. According to this approach, the real criterion is the time-to-failure of a specimen when held under a constantly applied "true" stress (creep). For testing conditions other than creep, the data were converted to the "equivalent" creep condition by means of a linear cumulative damage relation (26).

A typical failure curve is shown in Figure 13. The curve was obtained from uniaxial tests performed under superimposed hydrostatic pressures, which required shifting the failure data along the time axis by a time-pressure shift factor, a_p . As shown in Reference 9, data from strip-biaxial and poker chip tests fall on this failure curve. The poker chip specimens were tested at Rocketdyne and contained a center-mounted stress gage that easily measured the local stresses and the time-to-failure initiation.

The curve given in Figure 13 may be described mathematically as follows:

$$\sigma(\xi_f) - \sigma_\infty = f(\xi_f) \quad (4)$$

Where $\sigma(\xi_f)$ is the applied true stress expressed as a function of ξ_f

ξ_f is the reduced time to failure under the applied stress

σ_∞ is the stress below which failure will not occur

$f(\xi_f)$ is a descriptive function of ξ_f that need not be defined at this time

The reduced time, ξ_f , is defined by the relation

$$\xi_f = t_f / a_T a_p \quad (5)$$

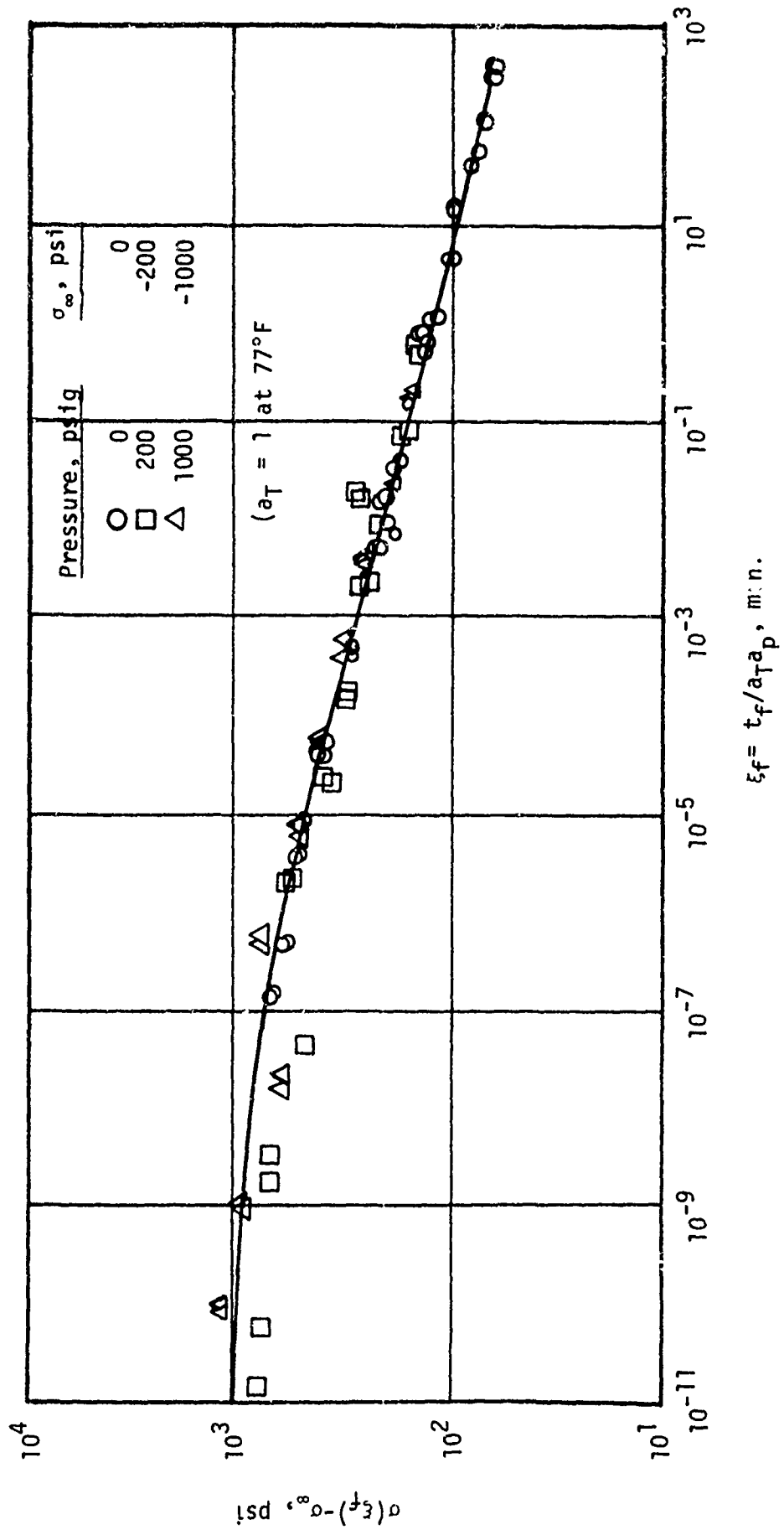


Figure 13. Effect of Superimposed Pressure on Constant Stress to Failure Data for a CTPB Propellant

Where t_f is the time to failure under a constant stress

a_T is the time-temperature shift factor

This relation may be normalized with respect to the glassy properties upon division by σ_g , to give:

$$\frac{\sigma(\xi_f) - \sigma_\infty}{\sigma_g} = g(\xi_f) \quad (6)$$

Where σ_g is the strength in the glassy region

and

$$g(\xi_f) = f(\xi_f)/\sigma_g \quad (7)$$

The relaxation modulus, $E(\xi)$, may be represented by the following well known relation.

$$E(\xi) = E_e + (E_g - E_e) \int_{-\infty}^{\infty} h(\tau) e^{-\xi/\tau} d \ln \tau \quad (8)$$

Where E_e is the equilibrium relaxation modulus

E_g is the glassy modulus

$h(\tau)$ is a distribution function of relaxation times

τ is a relaxation time

ξ is the reduced time of the test

After noting that $E_g \gg E_e$, Equation (8) can be rearranged to give the following normalized relaxation modulus

$$\frac{E(\xi) - E_e}{E_g} = \int_{-\infty}^{\infty} h(\tau) e^{-\xi/\tau} d \ln \tau \quad (9)$$

The normalized curves for relaxation moduli and the failure stress are plotted on the same time scale in Figure 14. The most notable points to be made are, that the two curves have different slopes in the transition region, and they are greatly separated along the time coordinate.

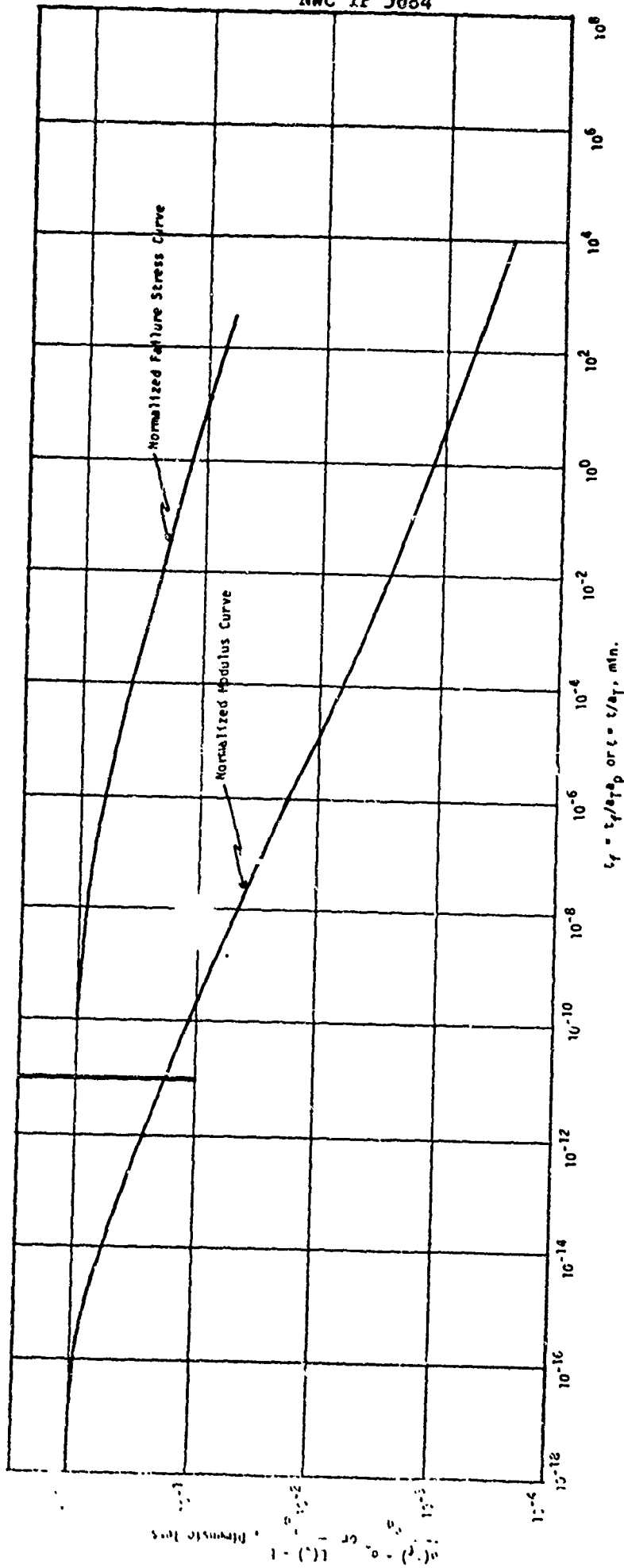


Figure 14. Normalized Failure Stress and Modulus Curves for CTPB Propellant

Taking the square-root of the relaxation modulus data and shifting the curve along the time-axis permitted the fit shown in Figure 15. Here, the modified relaxation modulus data are seen to fall within the data scatter of the creep-failure data.

The superposition of the two curves in Figure 15 permits the following equality

$$\frac{\sigma(\epsilon_f) - \sigma_\infty}{\sigma_g} = \left[\frac{E(\epsilon_f/q) - E_e}{E_g} \right]^{1/2} \quad (10)$$

Where $E(\epsilon_f/q)$ is the relaxation modulus taken at the time ϵ_f/q

q is an empirical constant that shifts the entire relaxation modulus curve

The value of q for these data was found to be about 3×10^6 . This is typical of past data where values of 10^8 were obtained.

This relation can be simplified after noting that Griffith's criteria for glassy material gives

$$\sigma_g = \frac{k\Gamma^{1/2}}{C^{1/2}} E_g^{1/2} \quad (11)$$

Where k is an empirical constant

r is the free surface energy per unit area of new surface

C is the length of an internal crack in the specimen

Inserting Equation (11) into (10) and rearranging gives

$$\sigma(\epsilon_f) - \sigma_\infty = \frac{k\Gamma^{1/2}}{C^{1/2}} [E(\epsilon_f/q) - E_e]^{1/2} \quad (12)$$

Equation (12) becomes a viscoelastic fracture criterion that includes the Griffith relation as a special case. Furthermore, the Griffith constants in the glassy region should apply over the entire viscoelastic time-scale.

The most unique feature of Equation (12) is the empirical, time-shift factor q . It was used originally by Halpin (27) and given a physical interpretation by him. We doubt that interpretation, but acknowledge the usefulness of the factor.

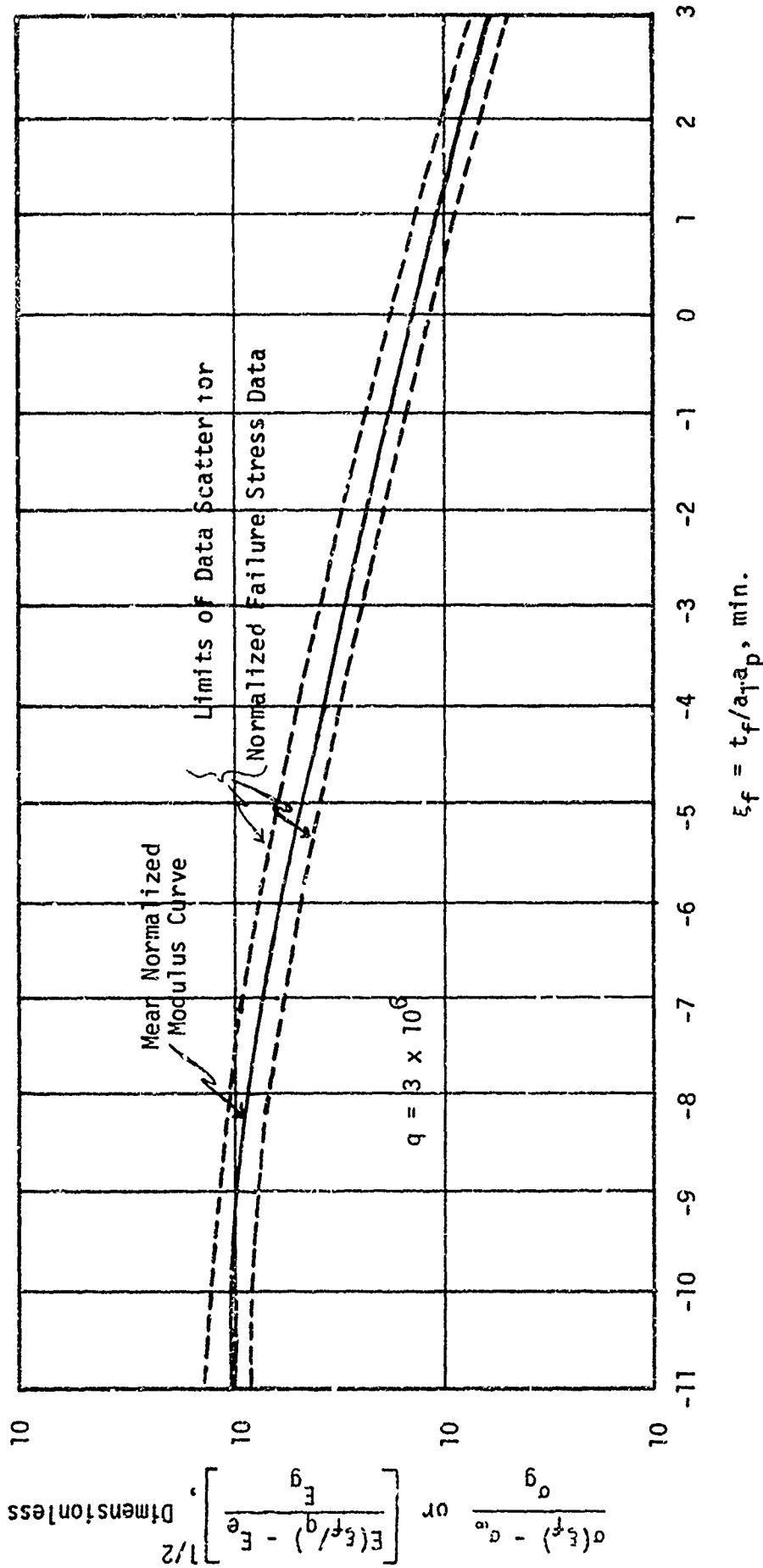


Figure 15. Superposition of Normalized Moduli and Failure Stress Data

$$\frac{\sigma(\xi_f)}{\sigma_0} \text{ or } \left[\frac{E(\xi_f/q) - E_0}{E_0} \right]^{1/2}, \text{ Dimensionless}$$

Recently, Schapery (28 and 29) developed a theoretical failure theory that is close to that of Equation (12). The major discrepancy is in the exponent, $1/2$, on the modulus. In Schapery's analysis this exponent has a value of $1/2(n+1)$; where n is a constant. Our experimental data support the possibility that Schapery's relation could be correct.

On the other hand, Blatz, using the concepts of viscoelasticity, and the power balance concepts of Griffith developed a relation that yields a square root relation (exponent equal to $1/2$) on the modulus. The work is summarized in Appendix A of this report.

Tests of Crack Depth Dependence

Two tests of our viscoelastic failure criterion were conducted. The first was a rough preliminary effort using constant load-to-failure tests on specimens that were notched on one side. The second set of tests was designed to eliminate some of the testing errors (specimen distortions and inaccurate time measurements obtained in the first experiments. As shown below, both experiments qualitatively support our empirical failure criterion

From Equation (12) it is seen that a plot of $[\sigma(\xi_f) - \sigma_\infty]C^{1/2}$ (13) versus $\log \xi_f$ should provide a direct means for evaluating crack depth dependence.

Constant Load-to-Failure Testing of Notched Specimens

Creep-to-failure tests were made at 77°F on specimens with razor cuts of $0, 1/16, 1/8, 1/4$ in., and under initial stresses of 45, 55, 65, 90 and 100 psi, based on the net cross-sectional area (after the cuts were made).

The test results are shown in Figure 16. For the notched specimens, the data are plotted as $\log [\sigma(\xi_f) - \sigma_\infty]C^{1/2}$ versus $\log t_f$. Although there is a considerable scatter in the data, they show a general consistency with all of the results falling along the same curve.

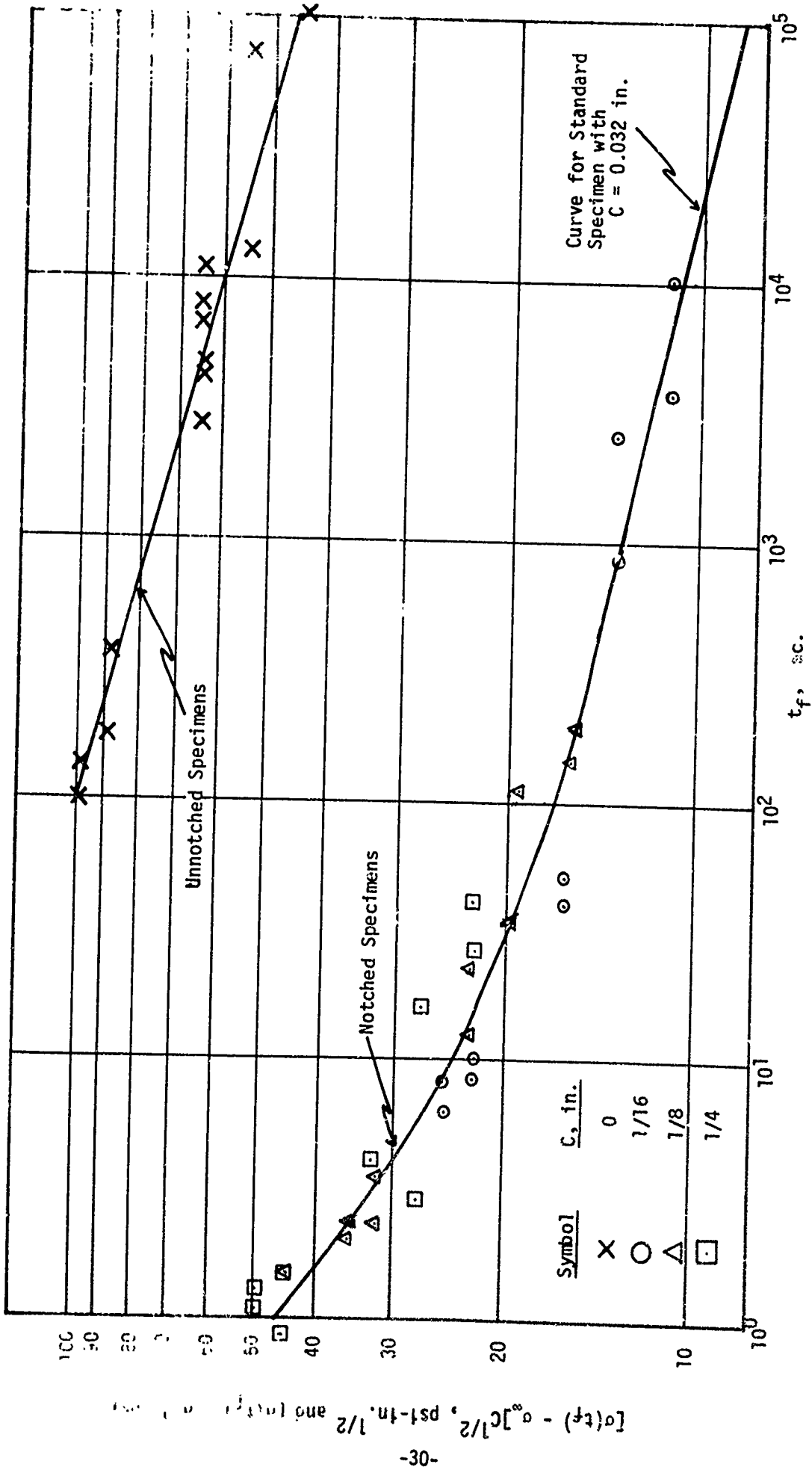


Figure 16. Results of Constant Load-to-Failure Tests of Specimens Notched on One Side

The notched specimen data show a strong upward curvature which is mostly associated with the larger stresses and the deepest cracks (1/4"). Therefore, we interpreted the curvature to be an artifact of specimen distortion and to the inaccuracies of measuring failure times below 10 sec.

Results of the unnotched specimen tests are plotted as $\log [\sigma(\xi_f) - \sigma_\infty]$ versus $\log t_f$. They follow a straight line, as expected. When these data are shifted vertically downward until they superpose upon those of the notched specimens, we can obtain an estimate for the basic flaw size in the unnotched specimen. The dashed line in Figure 15 represents the vertically shifted curve. The crack size represented by this shift is about 0.032 in. (800 μ).

Constant Rate Testing of Double-Notched Specimens

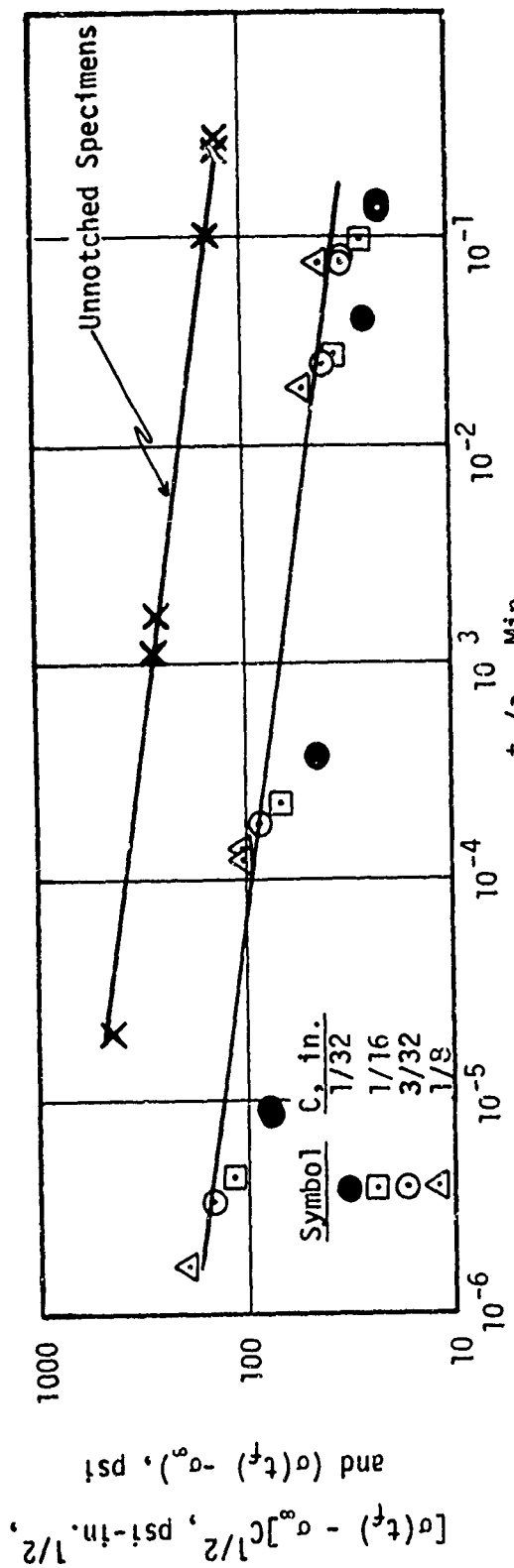
To minimize specimen distortion in this testing, we used the double-notched specimen described previously, Figure 6. To minimize the time measurement errors, we conducted all of the tests under a constant displacement rate of 2 in./min. Also, the tests were conducted in duplicate at -40° , 0° , 77° and 110°F .

The notches were cut into both sides of the specimens using single passes of a razor blade, with notch depths of 1/32, 1/16, 3/32, and 1/8 in. In this planning we made a mistake. The smallest notch was found to be of the same depth as the naturally occurring flaw. At the same time, when we cut into the specimen we force oxidizer particles to "snow-plow" ahead of the razor blade effectively cutting deeper than planned. We estimate that the effective crack was about 1/16" deeper than intended.

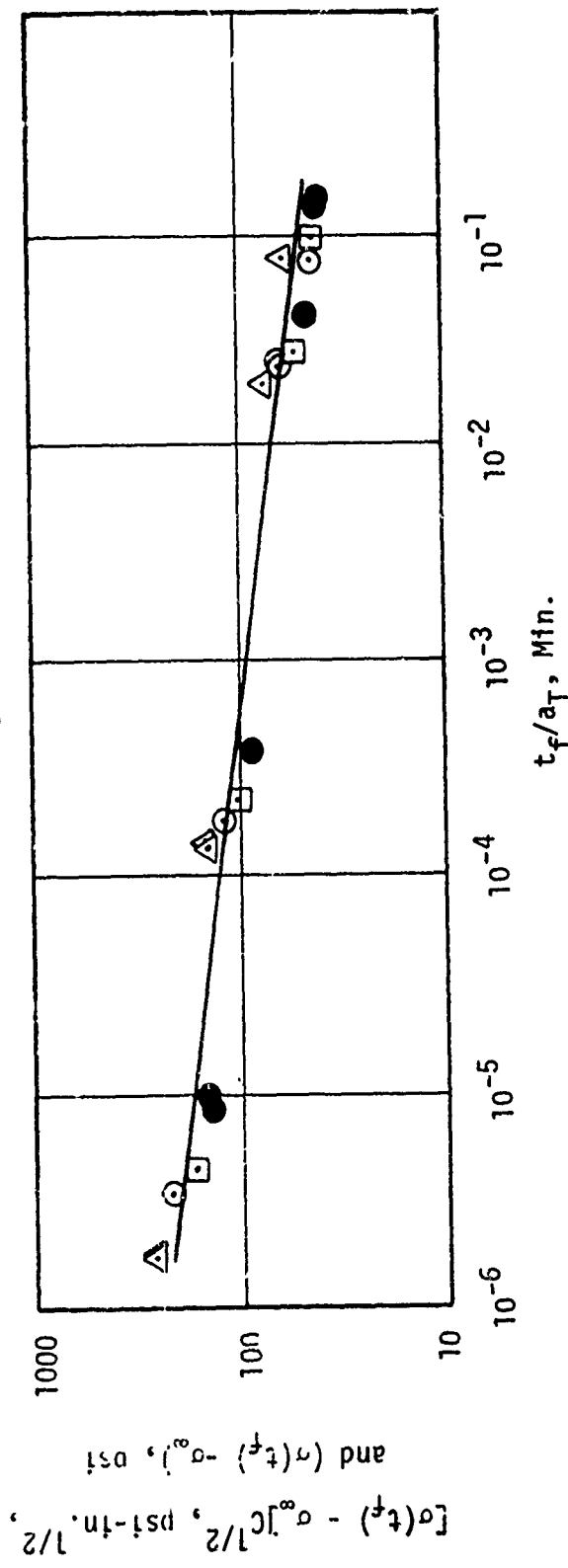
The experimental data were reduced to give "equivalent" constant stress-to-failure values through the use of linear cumulative damage analyses (3 and 6). This is a correction on the time-to-failure that varied from 0.15 to 0.58 for these results. The a_T values were taken from past data on ANB-3066 propellant.

Figure 17a contains a plot of the reduced data given as $\log [\sigma(\xi_f) - \sigma_\infty]C^{1/2}$ versus $\log t_f/a_T$. Also included in Figure 17a are the failure results for the unnotched specimens. The slope of the best straight line through these data was used to project a line through the fracture data.

Comparing the actual data with the drawn line, in Figure 17a, shows marked discrepancies for those specimens with shallow cracks. This, we feel, is due to the specimen preparation (as noted above) and to the relatively equal sizes of the shallowest crack and the inherent flaws (both about 1/32 in.).



a. Original Data Plots



b. Data Corrected to Include 1/16 in. Additional Crack Depth

Figure 17. Fracture Initiation Data for Double Notched Specimens of ANB-3066 Propellant

Figure 17b was prepared on the assumption that our specimen preparation actually produced cracks that were 1/16 in. greater than planned. The results are good, seemingly, justifying our preliminary assumption of the flaw size.

In spite of the experimental difficulties the initial results certainly give support to the fracture relation (12), and justify further investigations of the approach. Admittedly, these tests should be performed again: under circumstances where the specimens and the cracks, can be made larger to eliminate the sensitivity to specimen preparations.

Conclusions

From these results we concluded:

(1) That the crack depth dependency is about as Griffith had predicted, even under viscoelastic conditions.

(2) That a constant value of Γ may characterize propellant failures over the entire range of temperature and time conditions where propellants are normally used. This is not expected to hold for those conditions where the propellant changes its physical state (i.e. crystallinity) or chemical make-up within the range of test temperatures.

(3) Reduction of the failure data to an "equivalent" creep-to-failure test may take into account crack initiation under many complex loading histories. Admittedly, this is mainly an extension of our own vast experience with linear cumulative damage testing. But, once we have clarified the role of crack depth dependence the past experience becomes totally applicable.

(4) Future work should be directed at the evaluations of Γ and its use in predicting failures under various loading conditions.

(5) The effects of "dull" or rounded crack tips needs to be explored and corrections included in the basic relation.

(6) The strain-level dependence of the modulus may be a problem when evaluating the constancy of Γ in Equation (12). This point is discussed briefly in a later section.

FACTORS TO BE TAKEN INTO ACCOUNT IN DEVELOPING A FRACTURE THEORY

Developing an accurate failure criterion for solid propellants will be a fantastically complex undertaking since a number of intricate processes are simultaneously operating. Our recent studies have clarified the roles of a number of these processes, as described below.

Basic Failure Mechanisms

Here we shall consider the initiation and propagation of fractures in solid propellants and their weak binders.

It is concluded that solid propellants will initiate fractures in hydrostatic tension, but propagation requires a shear (distortion) component. Furthermore, propagation of the cracks is such as to make them turn and stop, necessitating new cracks to be initiated. The consequence of this behavior is that we have a "stick-slip" situation with many failure initiation sites.

These features are described next.

Failure in Propellant Binders

The failure processes in a propellant are best considered in terms of the binder itself. Consider, first, a simple poker chip specimen with a soft transparent binder bonded to a glass plate. With this specimen we can view failures as they occur.

Figure 18 is a photograph of this specimen after failure initiation in the binder. The failures are seen to be like gas bubbles in a liquid. The bubbles do not seem to propagate significantly after their initial appearance (although they may elongate somewhat as the specimen is stretched). Instead, there seems to be a tendency to initiate new failure sites.

Propagation of these failures clearly requires an additional driving factor. We found this in a test where a poker chip specimen experienced combined tension and shear. As shown by the photograph in Figure 19 the bubbles have grown in the direction of the shear component. The same failure result was obtained in a clear liner that was bonded to a glass-encased 5 in. dia. grain, Figure 20.

When the bubbles form under conditions of combined tension and shear, there is a peeling action in the direction of the shear. In the motor this is seen as long tubular separations that wander in fern-like patterns, Figures 21 and 22. The fern-like pattern will continue to grow, since the end stress condition (combined radial tension and axial shear) moves along with the leading edge of the growing crack.



Figure 18. Circular Shaped Bubbles Created from Failures
in Hydrostatic Tension



Figure 19. Oval Shaped Bubbles Created from Failures in
Combined Tension and Shear



Figure 20. Oval Shaped Bubbles Created Near the End of
a Glass-Encased Propellant Grain



Figure 21. Fernlike Pattern of Propagating Interface Cracks



Figure 22. Dense Fernlike Pattern of Interface Cracks

This mechanism of crack propagation is directly relevant to propellant failure processes. The close packing of oxidizer particles, Figure 23, produces local poker chip-type conditions, which Leon and McClintock (30) have shown to produce stress levels up to twice those imposed on the overall specimen. Failure is induced in the propellant at low elongations through bubble formation in the binder or through failure of the oxidizer-binder bond (usually called dewetting in the industry). This initial failure is not catastrophic to the propellant, so it will continue to elongate expanding the vacuoles previously formed.

If we concentrate on the dewetting behavior at a crack tip the vacuoles become very highly elongated, as shown in Figure 24. At the same time, the contiguous vacuoles experience strong shearing forces due to the geometries of their boundaries. As stated previously, this shearing action propagates the cracking process between the vacuoles. An artifact of this behavior is seen through the microscope, where these ligaments appear to be flowing (shearing action) like a viscous liquid.

Localized vacuole formation has many implications in the propellant failure process, including a marked effect upon the radius of curvature of the crack tip. This is discussed further in a later section.

Appearance of Real Cracks

Two distinct failure processes may be defined for solid propellants. They are defined by their propagation rates, with the low rate processes giving jagged cracks, while those at very high rates yield brittle-type failures.

All observations of inner-bore grain cracking under low deformation rates, have shown multiple tear initiations. This is easily seen in the early stages of these failures when the inner-bore frequently develops minute cracks. As shown in Figures 25 and 26 these tiny cracks propagate a short distance, then turn from their original trajectories and stop. The final joining of these short tears yields the jagged cracks shown.

(1) Low Propagation Rates

All observations of inner-bore grain cracking have shown multiple tear initiations. This is easily seen in early stages when the inner-bore frequently develops minute cracks. As shown in Figures 24 and 25 these tiny cracks propagate a short distance, then turn from their original trajectories and stop. The final joining of these short tears yields the jagged cracks shown.

Non-linear propagation of grain cracks also occur in the radial direction, Figure 27. Here, a 6 in. diameter, cylindrically perforated, grain was failed by internal pressurization. Figure 27 is a photograph of the central cross-section of the grain.

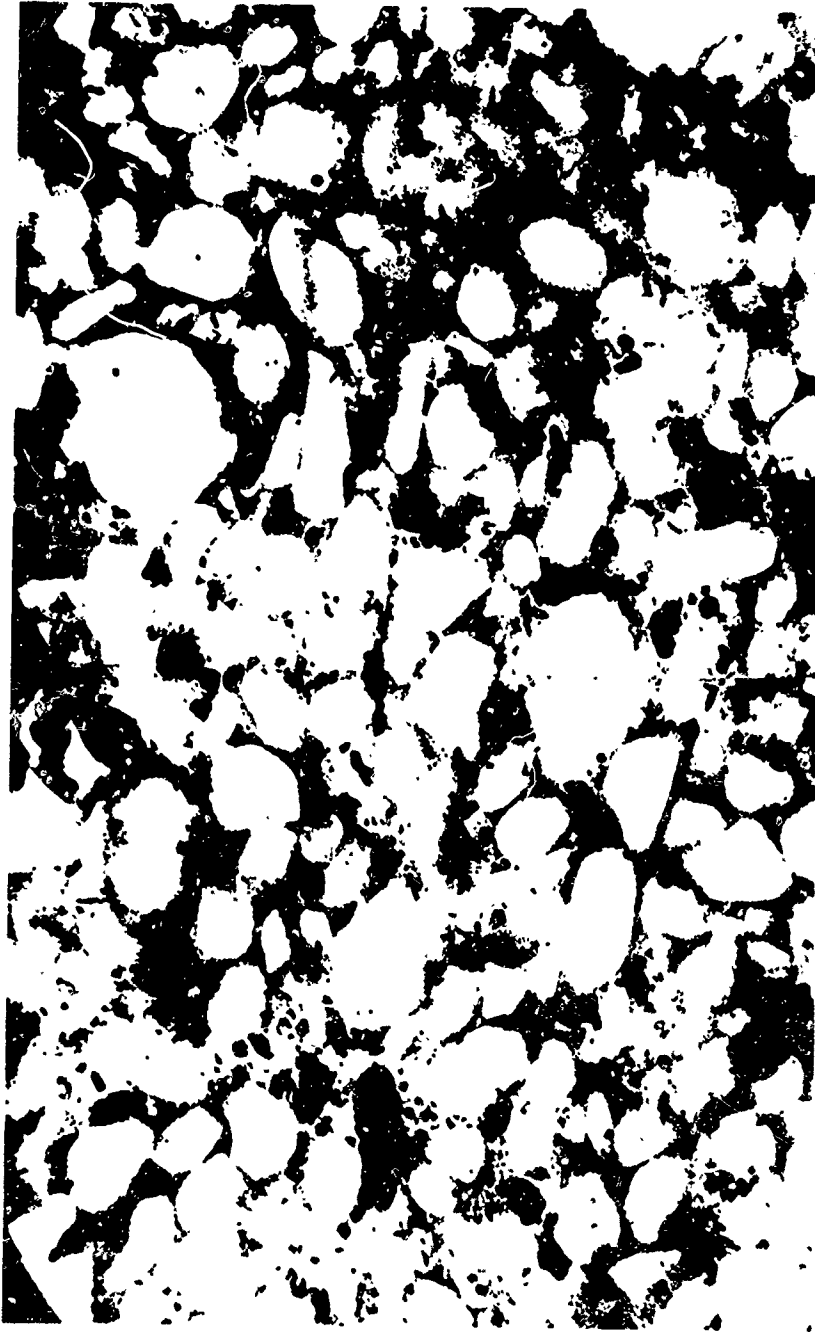


Figure 23. Photomicrograph of a Cross-Section of
ANP-2915-5 Polyurethane Propellant
(55 Diameters)

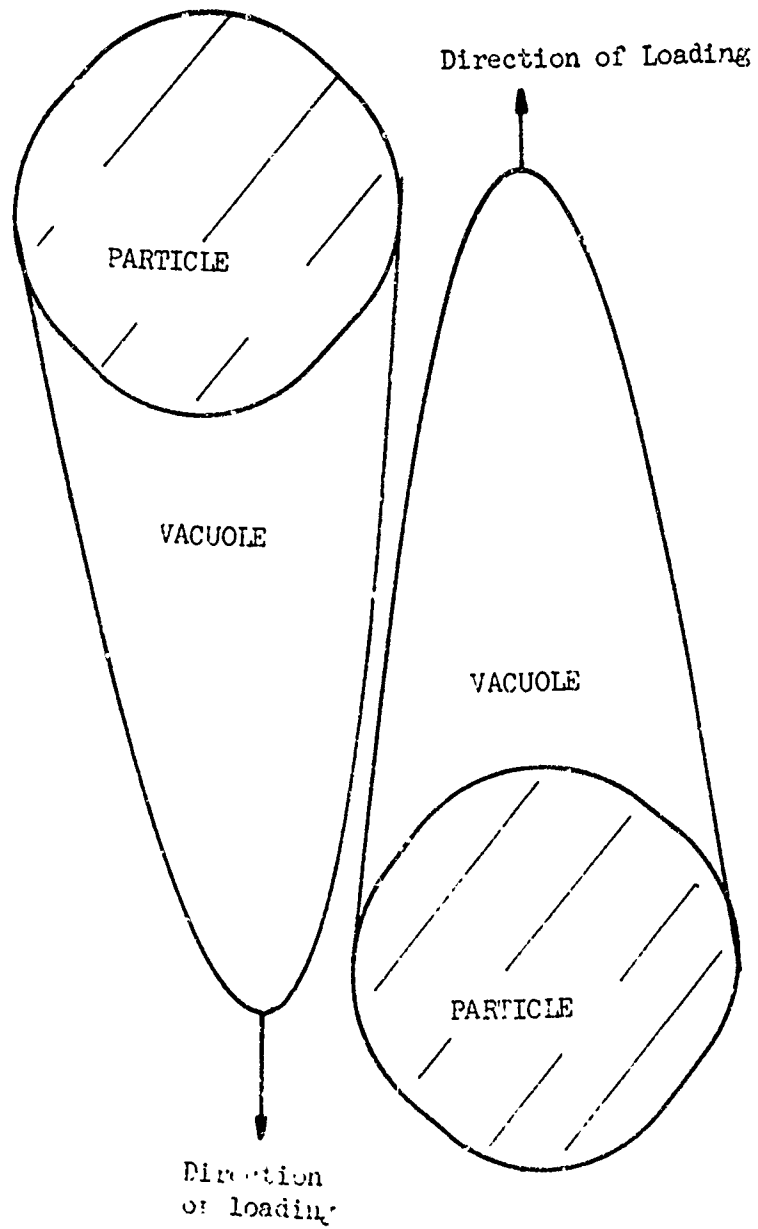


Figure 24. Schematic of Binder Ligament Between Two Vacuoles (Highly Elongated)

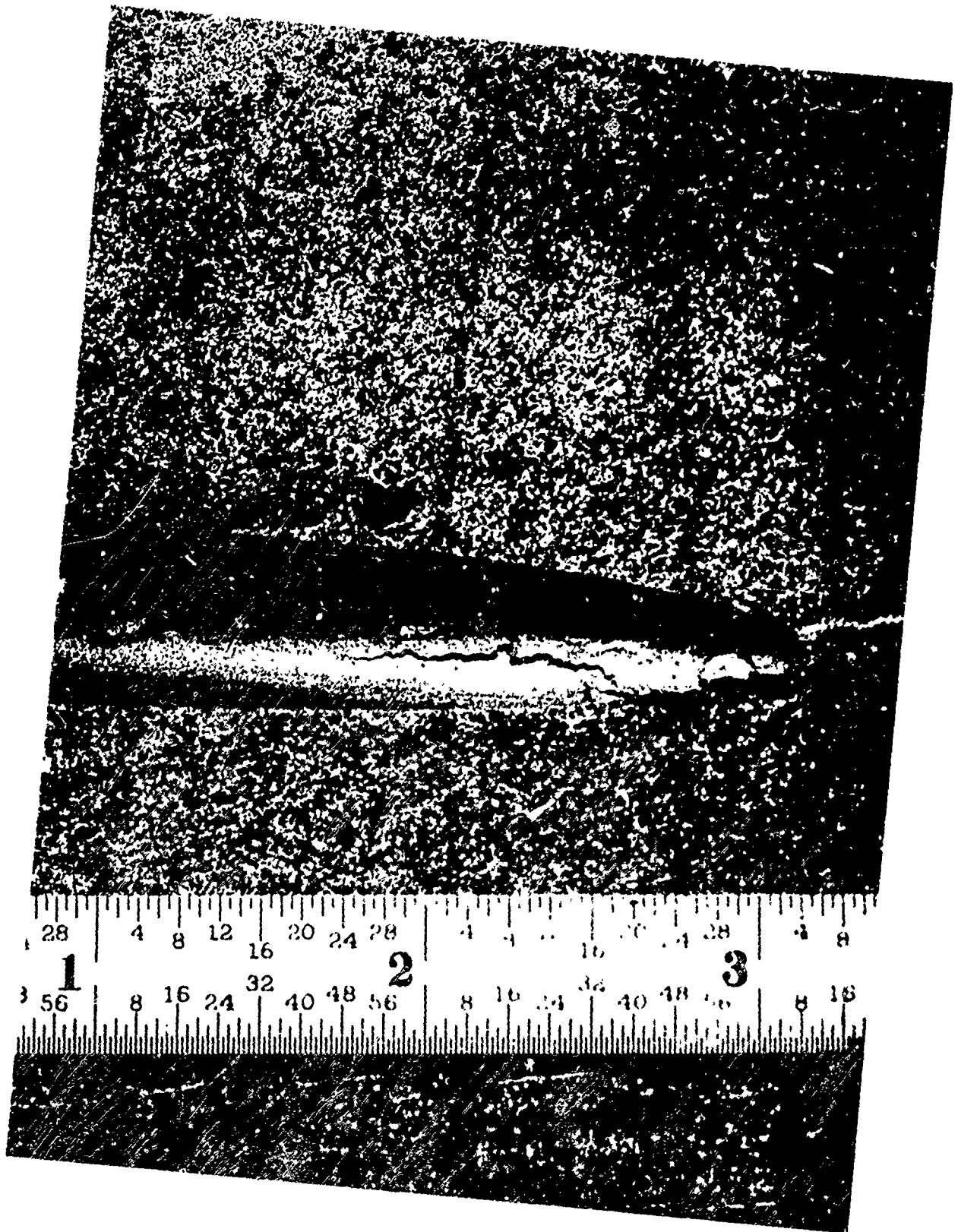


Figure 25. Jagged Cracks in a Grain Fin Slot

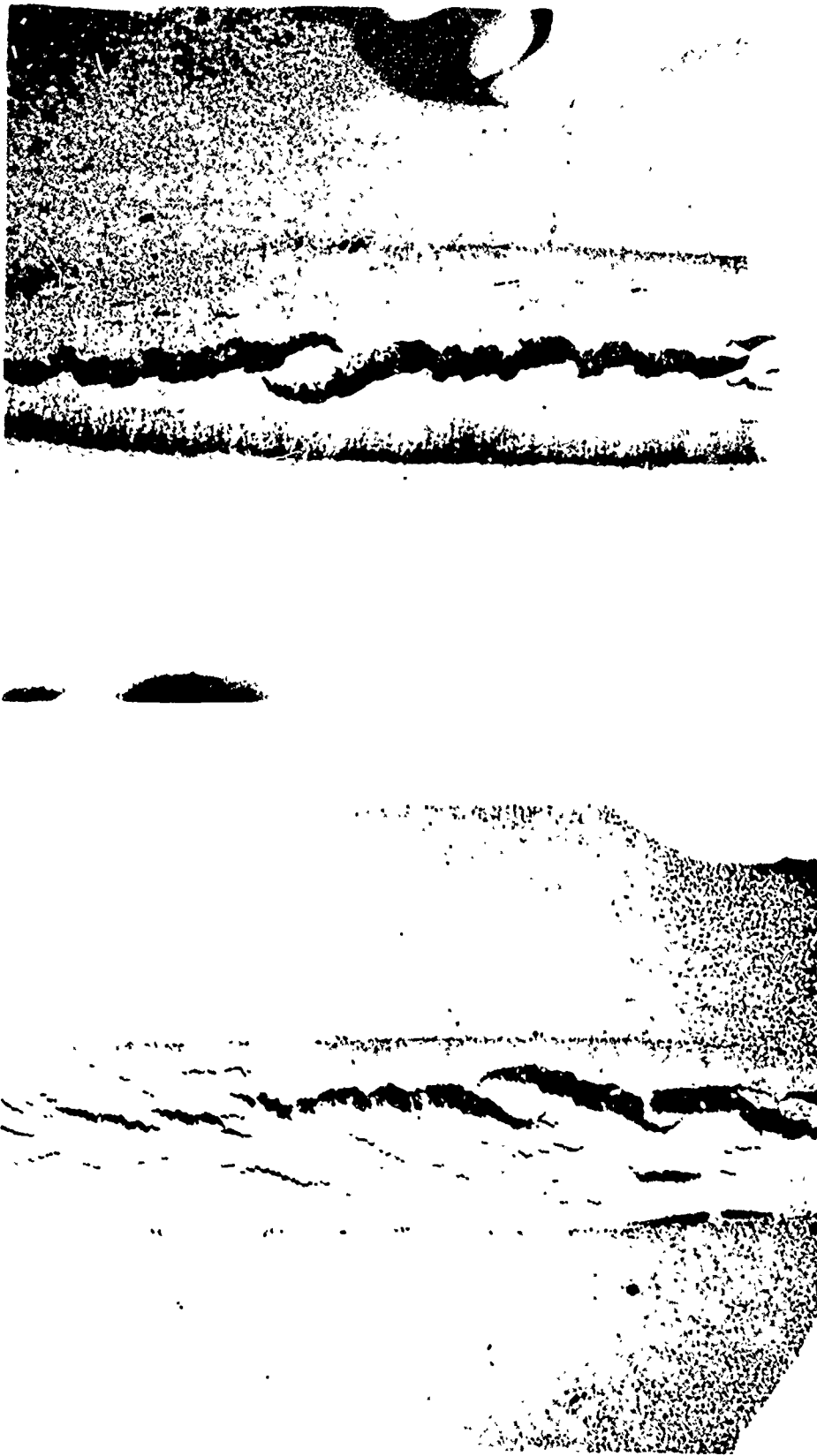


Figure 26. Multiple Jagged Cracks in a 5" Subscale Grain

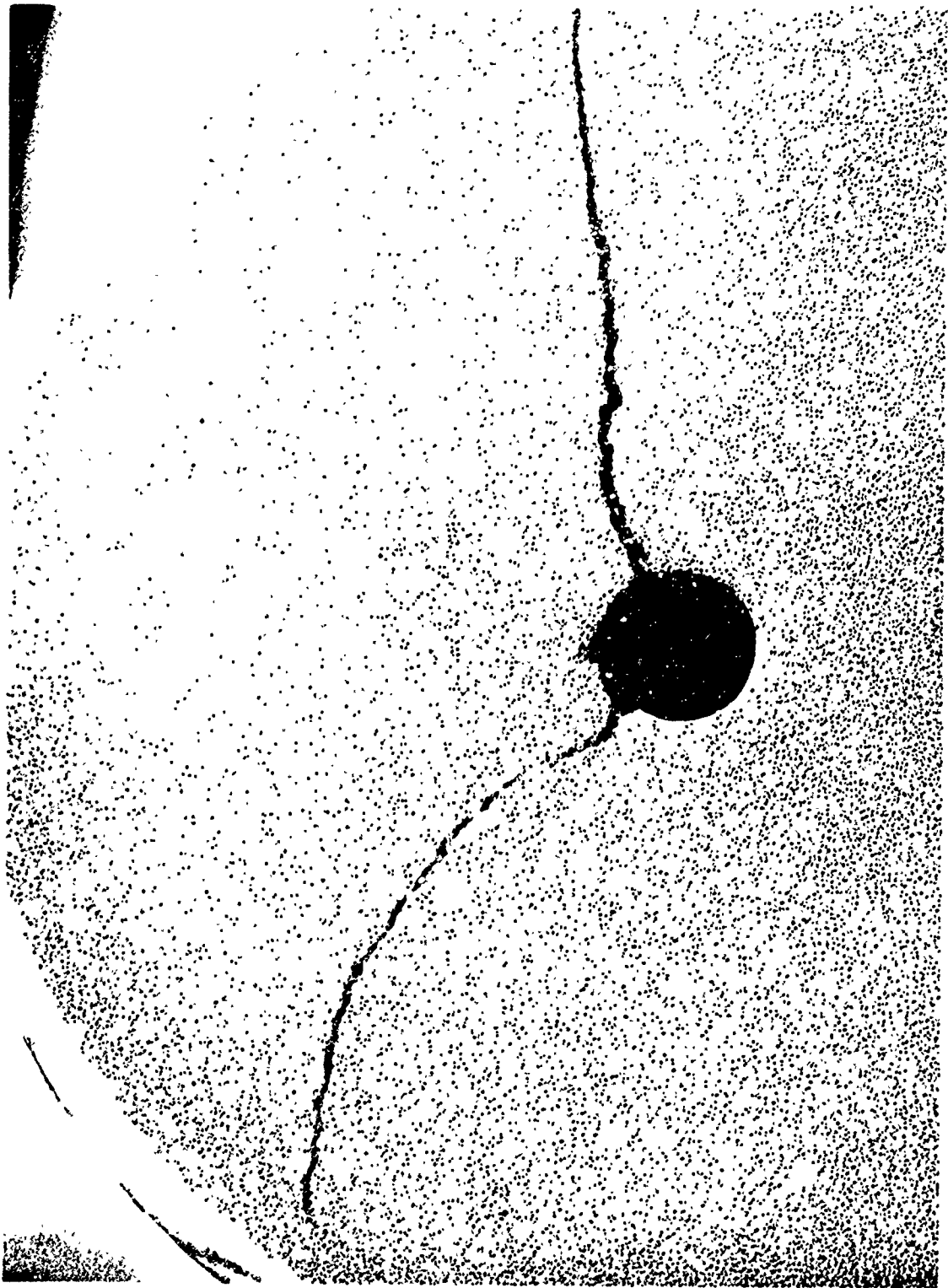


Figure 27. Non-Linear Propagation of Radial Cracks

Other examples of multiple fracture initiations and jagged cracks are given in References

A partial explanation for this behavior may be obtained from photoelastic analyses. Figure 28 shows the photoelastic stress patterns at the crack front in a rubber binder. Figure 28a was obtained with the stress at a sufficiently low level that the crack remained stationary, while Figure 28b was made at a level where the crack was slowly progressing. The artificial crack was first introduced by a sharp razor cut at the edge of the thin specimen. It is seen that the sharp front acquires a significant radius of curvature before the front progresses.

On close examination the photoelastic stress patterns show three stress concentration points, one directly in front of the crack tip, and two near the tip, but at an angle to the direction of crack propagation.

Using these findings, and a modification of a concept by Andrews (31 and 32), we have concluded that the stress at the axis of the crack tip is attenuated by the dewetting (or vacuole) process, leaving the two lateral stress concentrations to fight for control of the growing crack. Thus, crack propagation will not follow the crack axis but will follow one of the maximum stress trajectories, see Figure 29. This is what appears to happen in the small-scale propagation of a crack in propellants.

In the grain the rotation of the crack turns it into the hoop direction where the normal stress conditions are insufficient to continue the propagation process. Thus, the crack terminates and a new crack must be initiated to continue the failure process.

On the basis of the above, the cracking of a propellant grain is seen to go through four stages: initiation, propagation, and termination of small crack segments followed by a final tearing process across the various small cracks to form one large crack. Admittedly, stress levels, test temperatures and material properties will modify the various steps leading to a wide variety of behaviors from smooth to very jagged crack surfaces.

(2) High Propagation Rates

Under special conditions of temperature, deformation rate, or, sometimes, depth of crack, the propellant will exhibit a high rate of crack propagation. Figure 30 is a photograph of an inner-bore crack that was generated at a moderate rate. The crack is seen to be slightly rough, but it is not jagged like those obtained at lower rates.

Under brittle failure conditions where the crack rates are very high, the failures are smooth and they propagate through the AP crystals, as well. We have no available photographs of this phenomenon. But, a bar of propellant soaked in liquid nitrogen will exhibit brittle fracture,



Stationary Crack



Progressing Crack

Figure 28. Photoelastic Stress Patterns in Stretched Binder Specimens with Crack

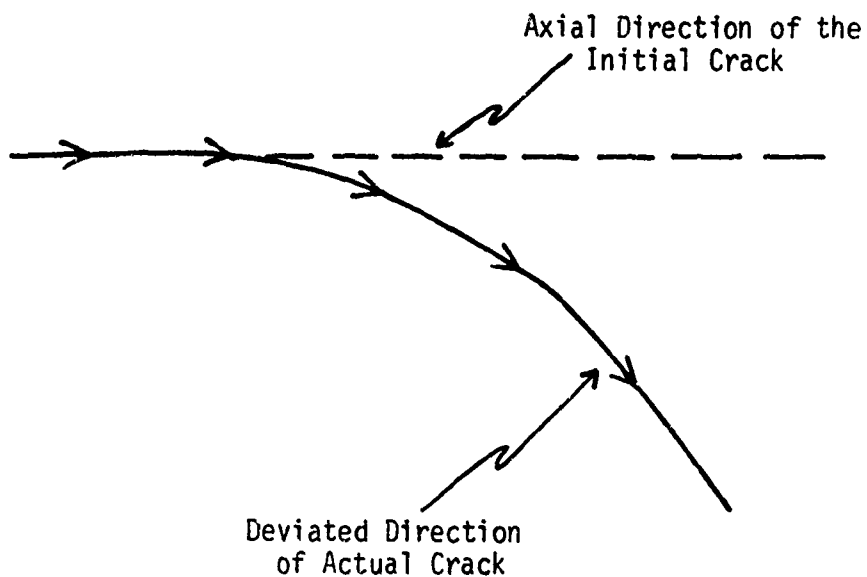


Figure 29. Deviation of Growing Crack
from Axis of Symmetry

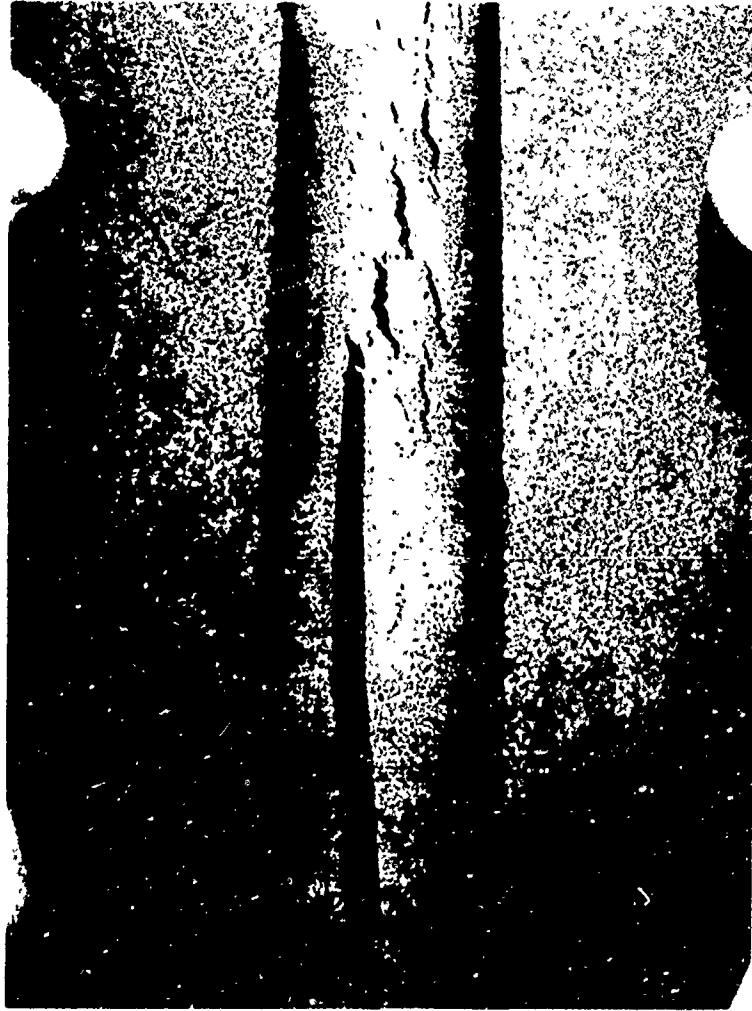


Figure 30. Long Crack Formed at an Intermediate
Propagation Rate

and the test is readily conducted by hand (gloved, of course). Actually, most propellants propagate fractures so readily at this temperature that a JANNAF tensile bar can be reduced to powder upon crushing in the fingers of one hand.

(3) Conclusions

The various failure processes observed above lead to the following conclusions:

(a) Under low propagation rates there will be a considerable energy dissipation along the jagged crack front, and in the extraneous failure initiations away from the main crack.

(b) The non-linear propagation of cracks at low rates should lead to errors in predicting crack trajectories.

(c) At very high propagation rates the crack trajectories are linear and the failed surfaces are smooth.

(d) In developing a practical theory, the transition from low to high propagation rates must be accomplished by analytical descriptors of the associated mechanical phenomena.

Effect of Dewetting Upon the Criterion of Failure

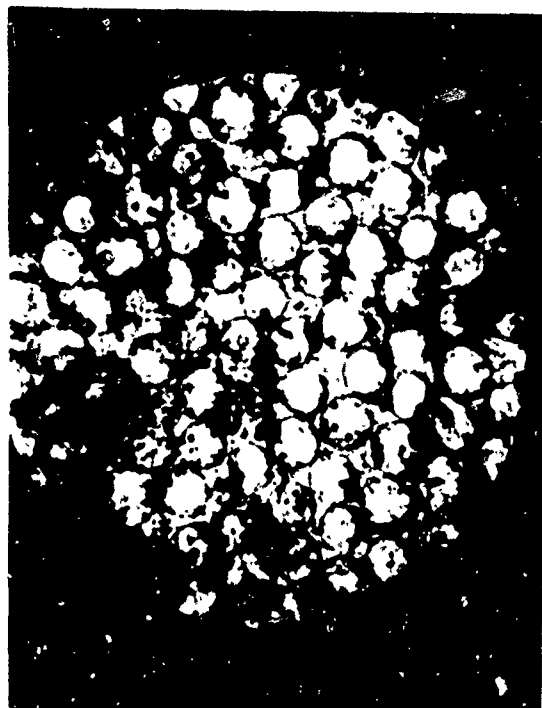
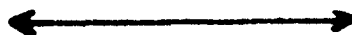
For specimens not experiencing compressive strains the dewetting phenomenon (or vacuole formation) provides a simple control over the mode of failure. In effect, dewetting reduces the local ligament geometry to that for an equivalent uniaxial test, regardless of the loading history. There is support for the same behavior under lateral compression, but it will not be made at this time.

Uniaxial, Biaxial and Triaxial Tension

Figure 31 is a photomicrograph of dewetting cavities (dark bands) forming around some glass bead as the specimen is uniaxially strained. Figure 32 is another photomicrograph of a specimen that has been pulled equally in biaxial tension. (This was an "Iron Cross" specimen that shows extensive ligation in a portion of a leg that was uniaxially strained.) As shown in Figure 33, the dewetting forms a honey-comb pattern. Thus, at the local level, the dewetting is the same as that for uniaxial tension.

This, reduction of problems to simple uniaxial dewetting conditions helps to explain why the uniaxial, biaxial and poker chip data can be represented by the same Maximum Principal Stress failure criterion (see above).

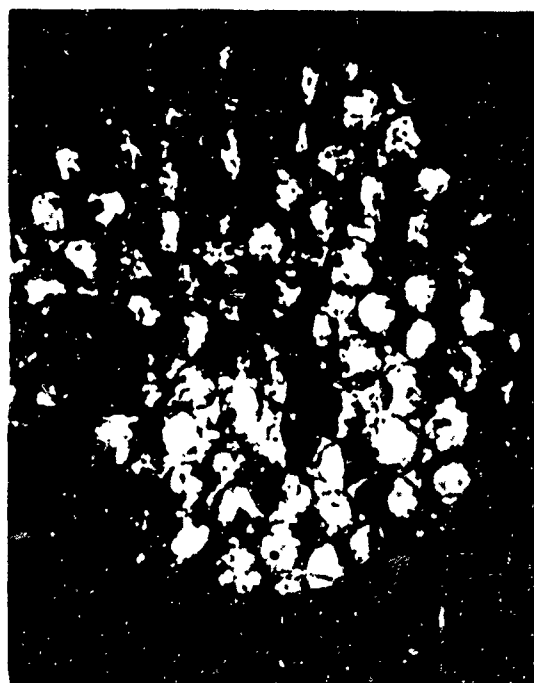
DIRECTION OF STRAIN



5% ELONGATION



10% ELONGATION



15% ELONGATION



25% ELONGATION

Figure 31. Dewetting in Uniaxial Tension



Figure 32. Dewetting Behavior Under Equal Biaxial Tension

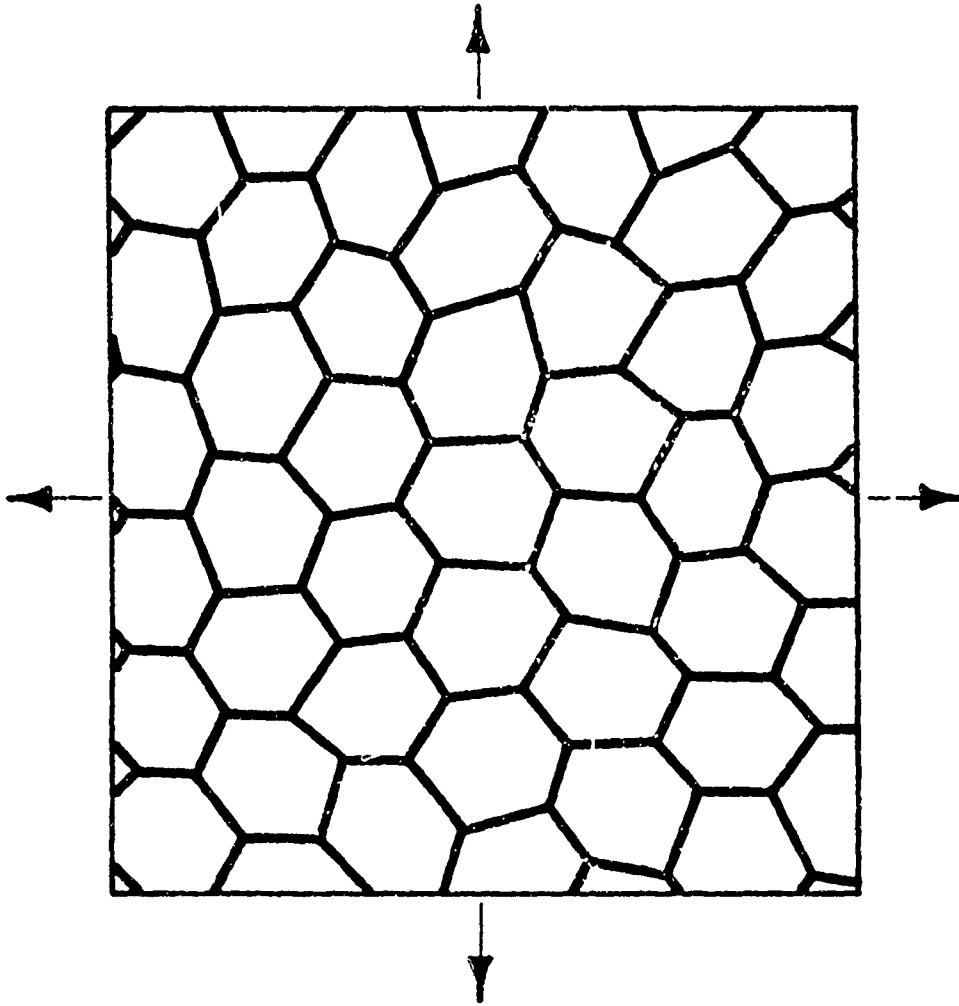


Figure 33. Schematic Representation of Dewetting Bands in a Biaxially Strained Specimen

Shear

We ran a special test on a shear specimen using notches cut deeply into both ends, Figure 34. Extensive dewetting occurred, especially at the right hand notch. The dewetting bands fell at an angle to an imaginary line connecting the notches. Thus, even the shear specimen yields extensive dewetting; the behavior being like a rotation of the uniaxial tensile test.

Conclusion

For the usual conditions of solid propellant applications, there is extensive dewetting with the result that all testing modes act as if they were uniaxials. However, at low temperatures dewetting may be suppressed and the simplifying assumptions due to the dewetting bands will no longer hold.

Loading Path Dependence

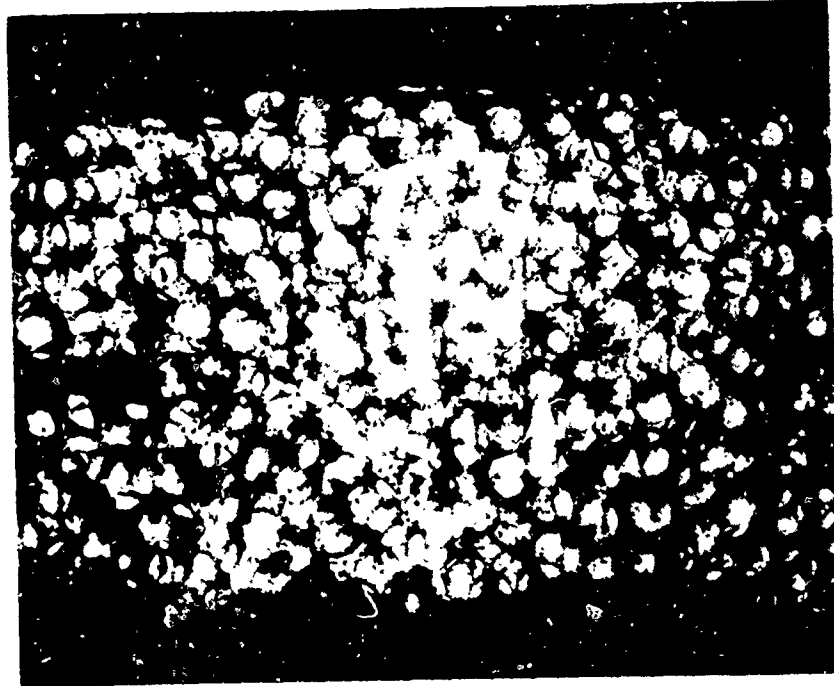
Failures in solid propellants depend greatly upon the order of application of the loads. Examples of this behavior are plentiful. Those presented here were selected to represent path-dependence under several different types of loading.

Temperature-Strain Paths

In this example we have considered three paths: Path I is for a propellant specimen that is strained, then cooled; Path II is for the specimen that is cooled and then strained; and Path III involves simultaneous cooling and straining. Figure 35 summarizes these paths schematically.

The path dependence of a polyurethane propellant was observed in a series of tests where the specimen was strained or cooled along the different paths of Figure 35. The results are:

<u>Path</u>	<u>Description</u>	<u>Observed Failure Strains</u>
I	Cool specimen from +40° to -75°F, then strain to break at 0.74 min ⁻¹	Average $\epsilon_b = 2.0\%$ at -75°F
II	Stretch specimens to various strain levels at 40°F hold and cool to -75°F	Strains up to 25% held 9 days when test terminated
III	Simultaneous cooling and straining from +40°F to -75°F at 10°F/hr and 1.08% strain/hr.	Average $\epsilon_b = 7.7\%$ at -30°F
III (Modified)	Specimens were given a 10% pre-strain before following Path III above.	Average $\epsilon_b = 21.9\%$ at -75°F



a. Unstrained



b. 20% Shear Strain

Figure 34. Dewetting in a Notched Specimen Undergoing Shear Deformation

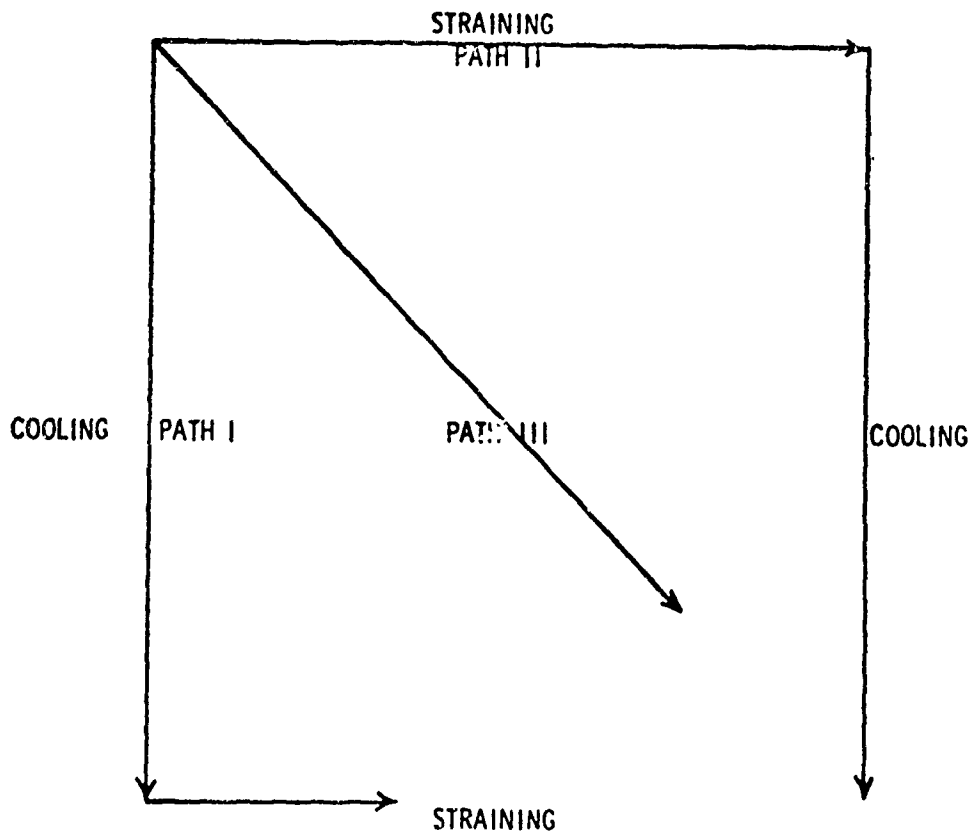


Figure 35. Schematic Representation of Path Dependency

From these data it can be seen that Path I gives the lowest value for ϵ_b , while Path II gives the largest values. However, Path III is more typical of the experience of a motor, and is intermediate between Paths I and II.

Bauschinger Effect

This effect modifies the response behaviors of all materials that exhibit creep or hysteresis, including hard steels. The effect described here arises from a pre-loading in compression during which the material experiences "temporary set." This "set" causes an effective shift of the coordinate stress-strain axes, which, of course, will modify the apparent failure properties when the sample is tested in tension.

Tests were conducted on the standard specimen used to characterize the strain energy release rate in solid propellants. This is a strip-biaxial specimen with a 1 in. razor cut made in the specimen center.

In this test, the specimen was put into 5% compression, held 10 min. to induce a temporary set, then, without removing it from the fixture, the specimen was pulled at a constant rate until crack initiation was detected.

Figure 36 contains a plot of the stress-displacement curve for a CTPB propellant tested in this manner. The results of a standard test are included for comparison in Figure 36. As summarized in Table I there is a reduction of 15% in the failure stress (tear initiation) while the axial deformation is reduced by 24%.

Pre-Strain Before Pressurization-to-Failure

This, also, is a Bauschinger effect, except that the shift of the coordinate axes is into the tensile stress-strain region. Thus, it may show a benefit to grain performance.

Motor firings at low temperatures involve rapid straining beginning from the existing thermal strain. The laboratory test for this is to pre-strain the propellant then test it to failure under superimposed hydrostatic pressures.

Figure 37 contains the failure envelopes for a CTPB propellant tested at -75°F under an 800 psi superimposed hydrostatic pressure. The envelope generated from specimens with a 10% pre-strain has a distinctly improved failure strain capability over that of the specimens without pre-strain.

Figure 37 was used to plan a set of experiments where four motors were cooled to -75°F and pressure tested (33). Failures were not obtained until the envelope on the right was exceeded.

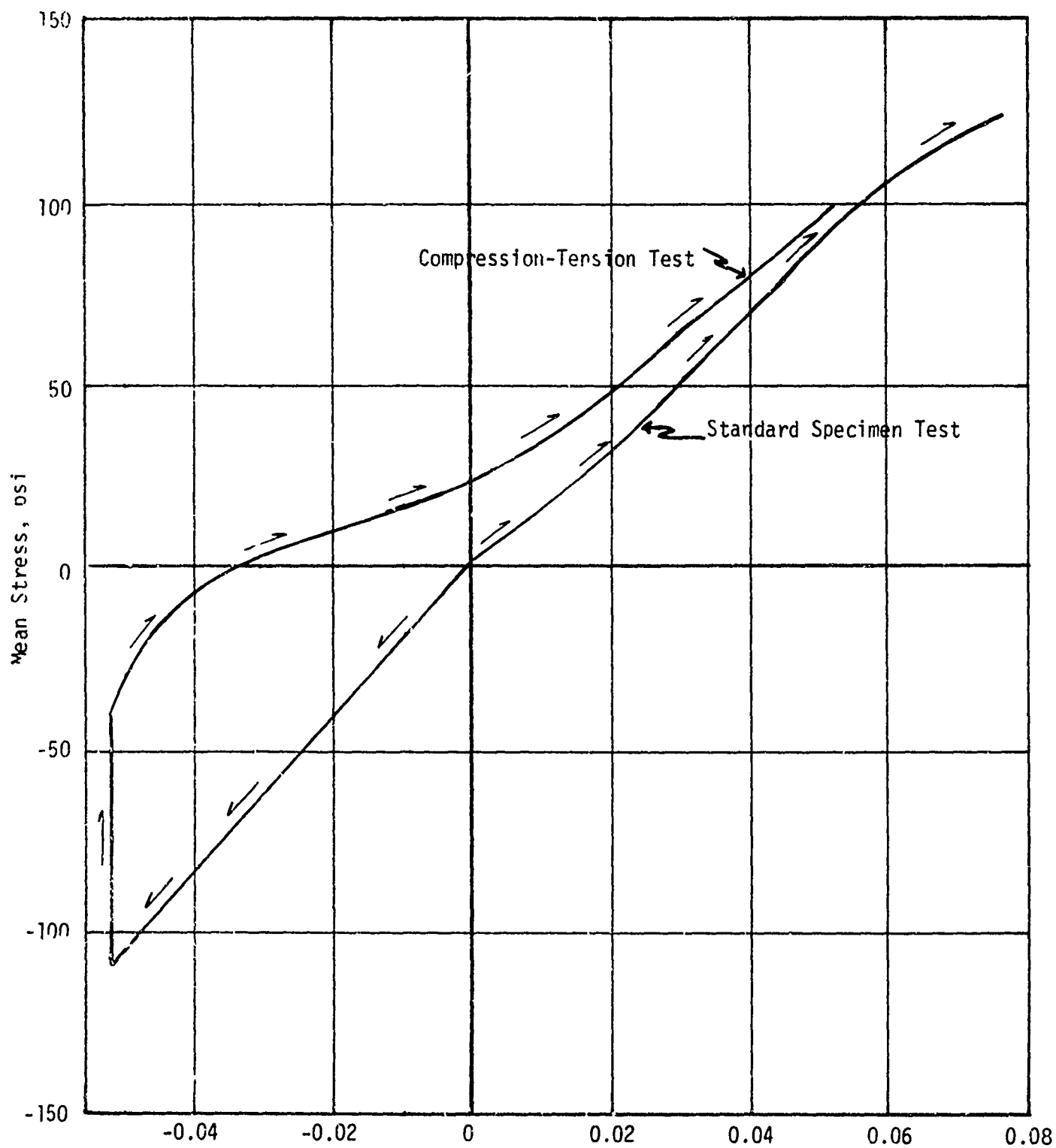


Figure 36. Bauschinger Effect in Strip-Biaxial Tear Specimen

TABLE I

BAUSCHINGER EFFECT IN TEAR SPECIMENS OF A CTPB PROPELLANT AT 77°F

<u>Test</u>	<u>Failure Stress, σ_f, psi</u>	<u>Displacement at Failure, Δl, in.</u>
Tension only	116	0.079
	<u>121</u>	<u>0.077</u>
Mean	119	0.078
Compression- Tension		
(5% Compression for 10 min.)	96	0.052
	<u>106</u>	<u>0.066</u>
Mean	101	0.059
Difference, %	15%	24

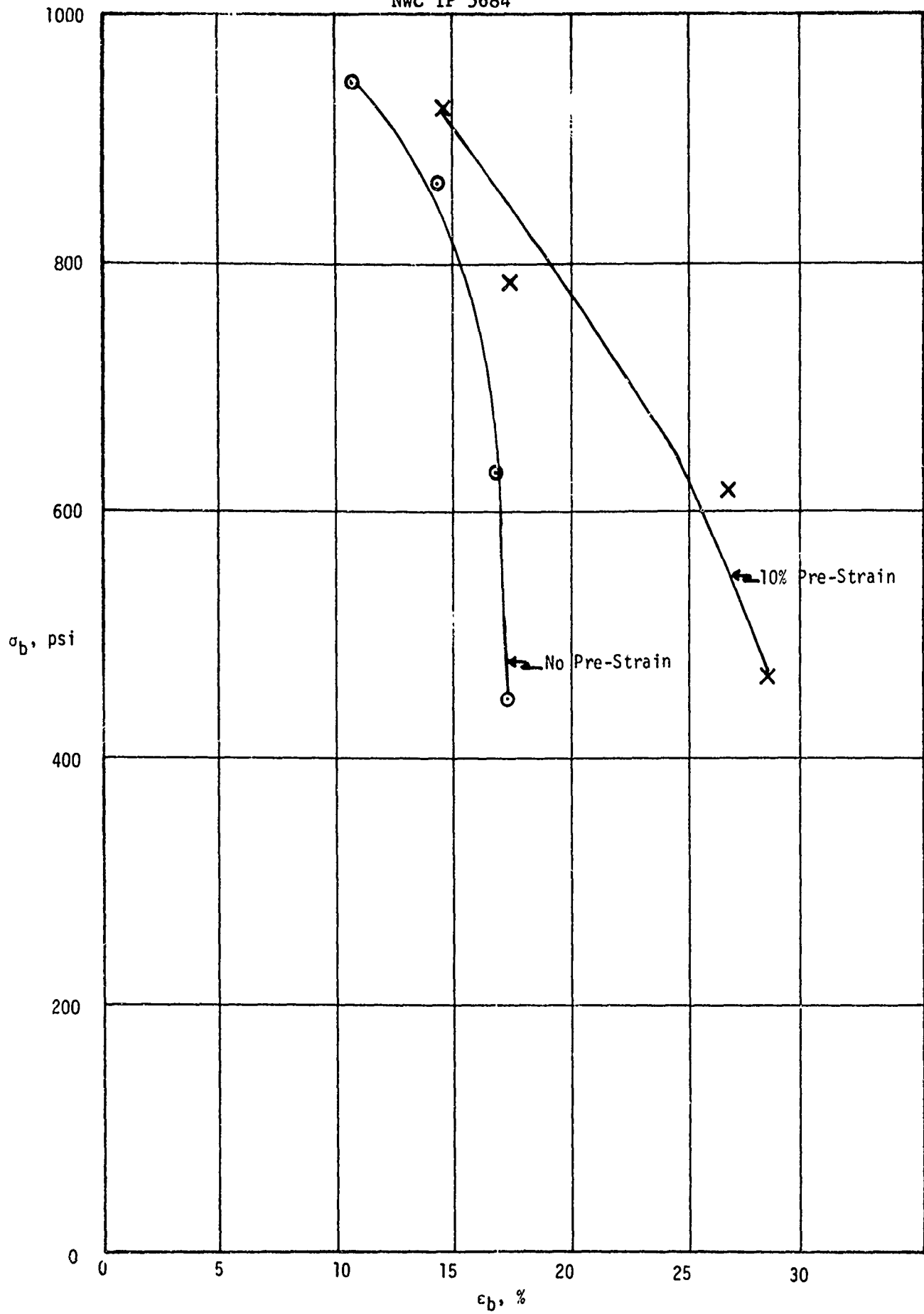


Figure 37. Effect of Pre-Strain on the Failure Envelope for a CTPU Propellant Tested Under 800 psi Pressure at -75°F

Conclusions

The strong path dependency of solid propellant failures is primarily a material response problem. These changes in material response affect both the shape and the stresses at the tip of a crack, thus modifying propellant failure properties.

If we are to have a viable failure theory it must contain a realistic constitutive theory that accounts for path-dependencies like those described above. Because of that need we instituted a theoretical effort to develop the required relations. The preliminary efforts in this area are summarized in a later section of this report.

Independence of Filler Content

The important aspects of dewetting and vacuole formation need further clarification. This is essential since a number of failure theories (15 to 17) have centered around the phenomenon. We find the following data to be somewhat challenging to those theories.

A number of HTPB propellant compositions were made using different filler fractions (0, 50, 64 and 76.3 vol. %) and various binder equivalents ratios (crosslinking levels). One of the material characterization methods included standard tensile tests conducted over a range of temperatures and crosshead speeds.

The tensile strength data given in Figures 38 to 40 show this property to be entirely independent of filler content. This contradicts our pre-conceptions of dewetting, where material strength would seemingly be reduced as the filler content increases.

That is, one would expect that as more filler is used there should be more dewetting; or, that the particles should be brought closer together inducing local stress concentrations and earlier failures. Clearly, the data in Figures 38 to 40 contradict that expectation.

Strong Time Dependence

There are a number of meaningful molecular parameters that affect the way propellants respond and fail. We shall consider only one, an old "friend", binder crosslinking, which we have found to be much less important than previously supposed.

An exception is taken to the position of Landel and Fedors (34 and 35) with respect to the failure properties of lightly crosslinked elastomers, which is the case for solid propellant binders. They indicate that the tensile strength of an elastomer is proportional to its crosslink density. However, from the data of Bueche and Dudek (18, 19 and 20) this should be true only for the more highly crosslinked elastomers.

The analyses of Bueche and Dudek (18 to 20) show that the stress at break on the rubber consists of two parts; a normal kinetic theory stress on

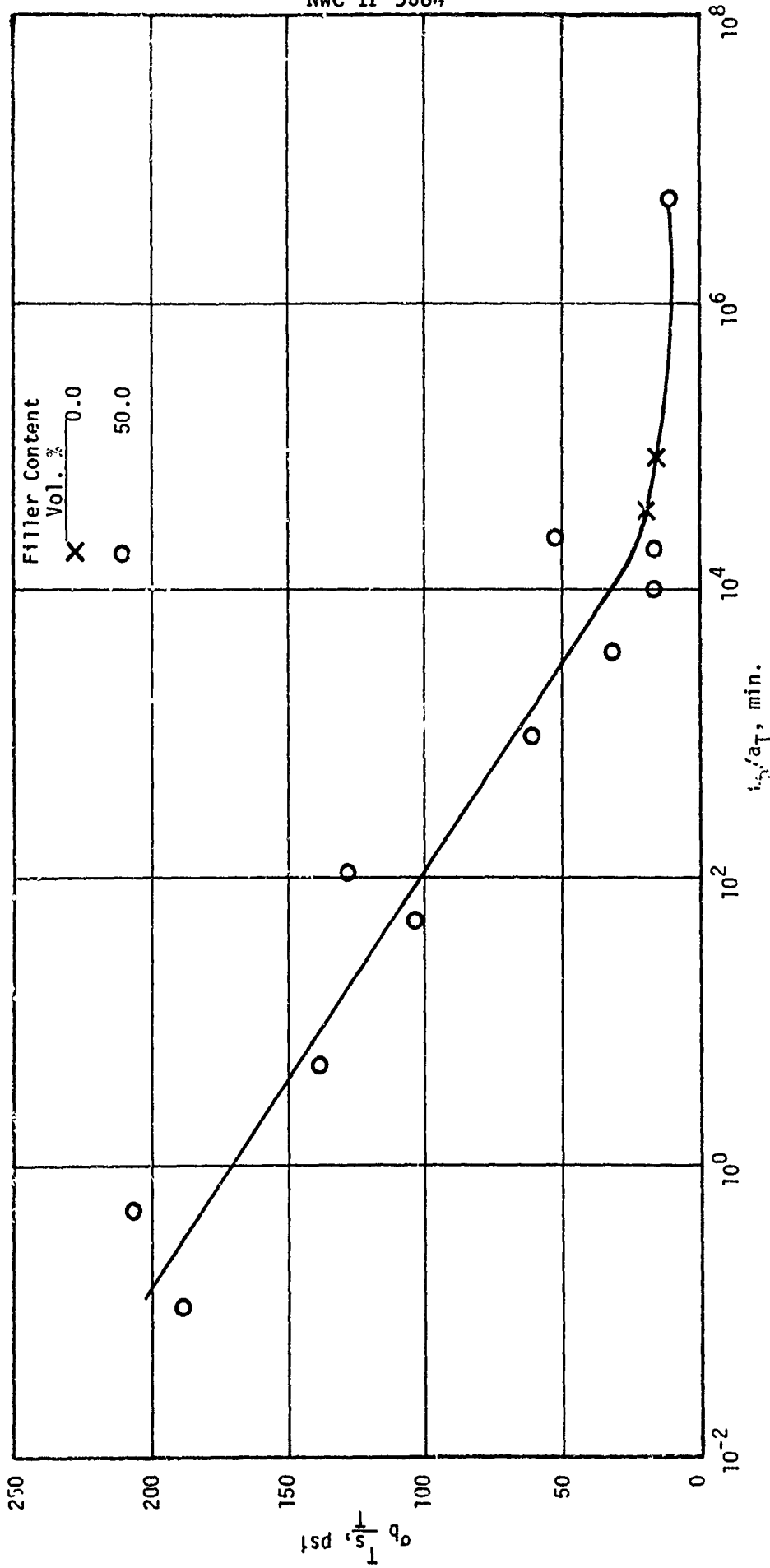


Figure 38. Master Plot of the Stress-at-Break for an HTPB Polymer
 - Equivalents Ratio 60/40 -

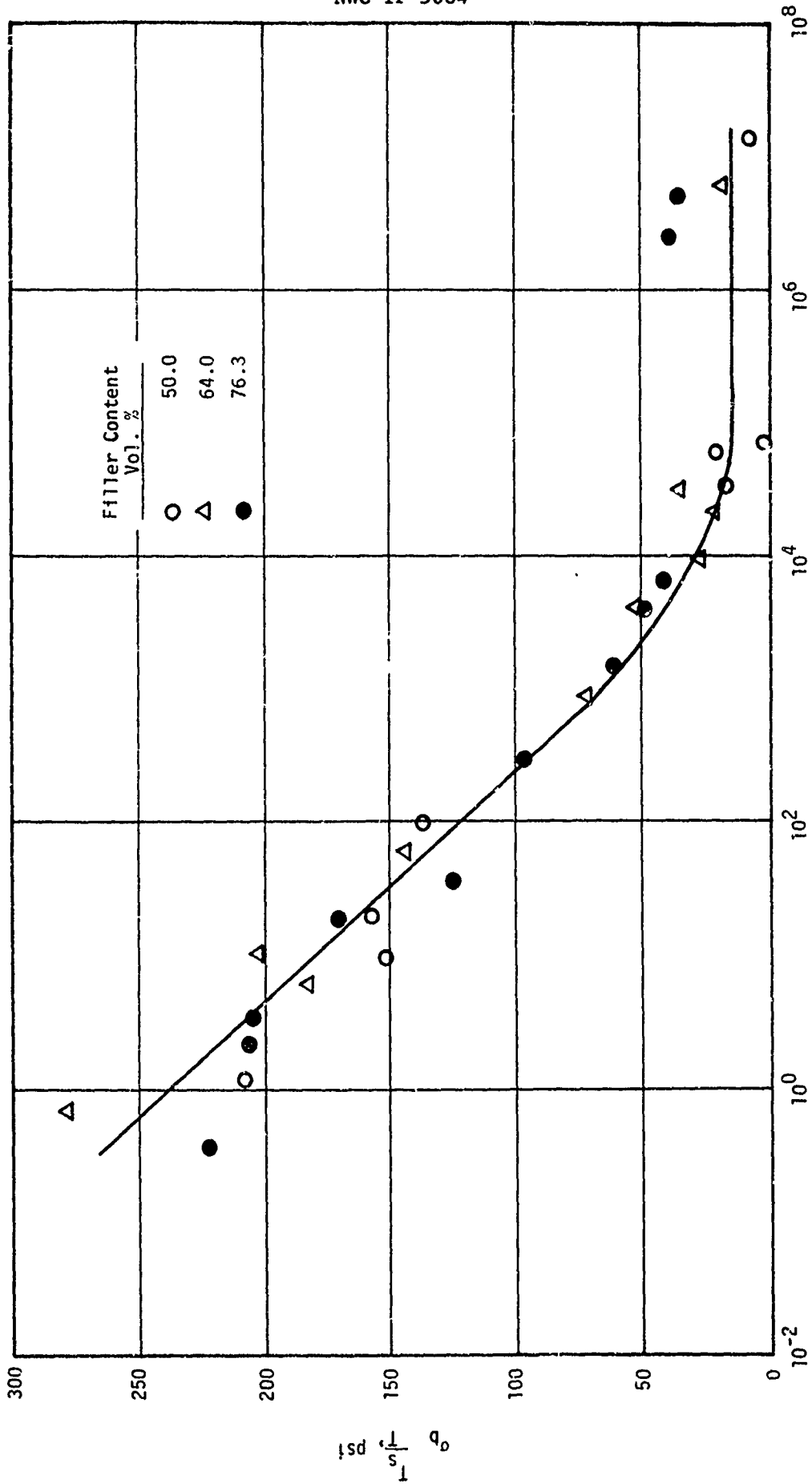


Figure 39. Master Plots of the Stress-at-Break for an IITPB-Polymer

- Equivalents Ratio 70/30 -

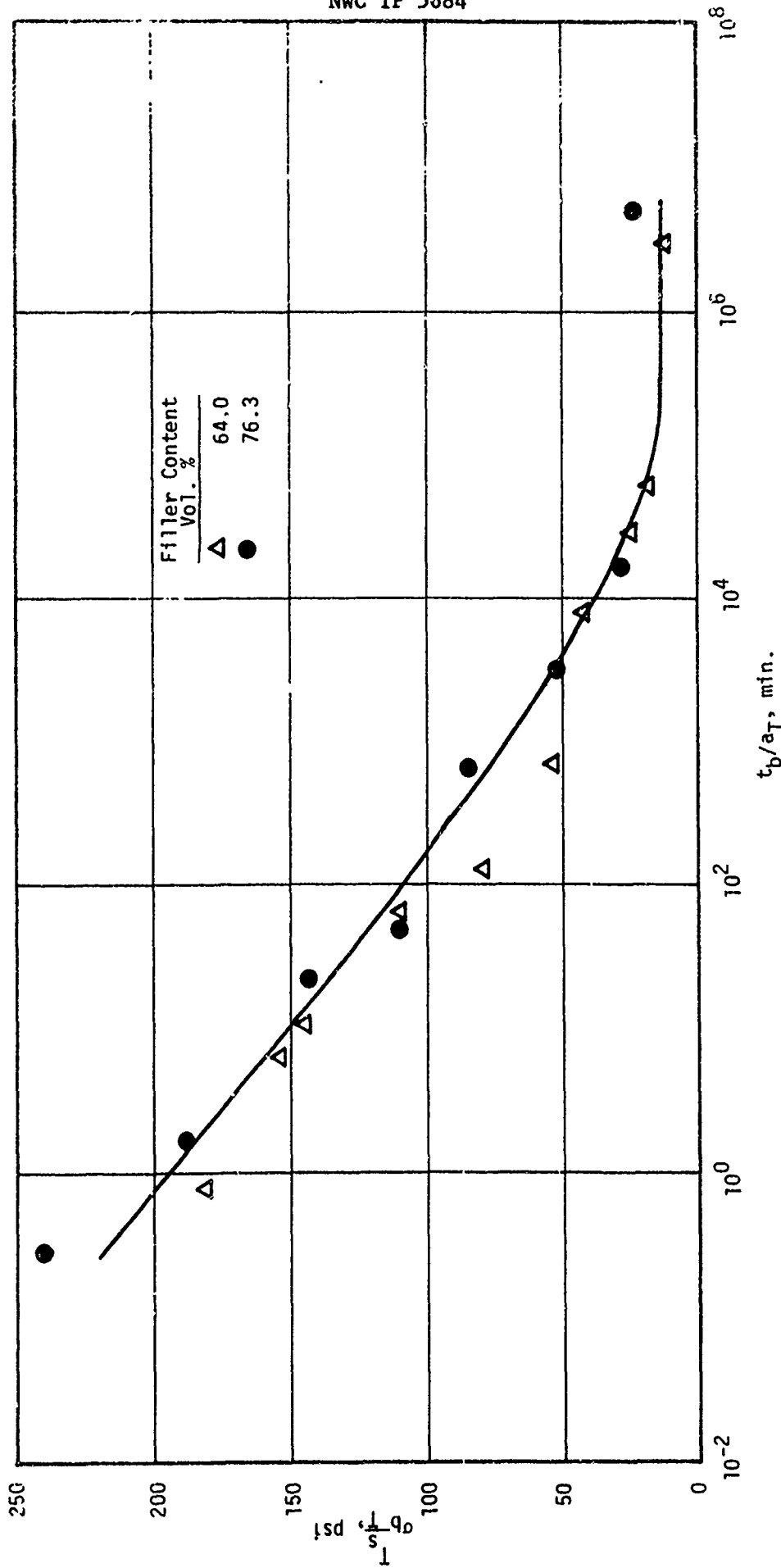


Figure 40. Master Plots of the Stress-at-Break for an HTPB Polymer - Equivalents Ratio 80/20 -

the network and a highly rate-dependent stress held by fully extended chains. The fraction of the chains in the fully extended state at the instant of break is much greater for lightly crosslinked rubber than for highly crosslinked rubbers under nonequilibrium test conditions. They show that the kinetic theory stress (related to polymeric crosslinking) contributes the major portion of the stress-at-break in highly crosslinked amorphous rubbers. However, the stress-at-break of very lightly crosslinked rubbers is largely the result of stresses in the most highly elongated chains.

This theory is illustrated in Figure 41, which is a plot of the stress-at-break vs the log of the crosslink density for an SBR amorphous rubber. The experimental data show the strength to increase to a maximum then decrease as the crosslink density is increased. The theoretical prediction of Bueche and Dudek is given as the solid line in Figure 41 while the load supported by the crosslinked network (elastic contribution) is shown by the dashed line.

The maximum in the curve of Figure 41 was also studied by Bueche and Dudek (20) and an explanation given. It is due to the fact that a greater fraction of chains, which have been extended to their limit of extensibility, is present at the moment of fracture in lightly crosslinked vulcanizates. A rate dependent nonaffine deformation of the network junction points comes into play at these chain elongations approaching full extension and provides a molecular mechanism to explain the results.

From these data we concluded that the parameter plays a lesser role in propellant properties and aging effects than previously supposed.

Characterization of Material Fracture

Laboratory characterizations of propellant fracture are considered to be inaccurate. This stems, mostly, from differences between the shapes of the crack tips as seen in the motor and those obtained during laboratory characterization.

All of the cracks obtained in motor testing have sharp tips, Figures 25 to 27 and Figure 30. By contrast, the crack tip in a laboratory specimen can be markedly rounded, Figure 42. The photograph given in Figure 42 was selected as the most exaggerated case of those available to us.

Figure 43 is a photograph of fracture initiation in a specimen where the razor cut was slightly canted.

Figure 44 was chosen to illustrate that the stresses at the crack tip are not necessarily the highest ones in the test specimen. Here, specimen failure initiated at a point ahead of the artificial crack tip.

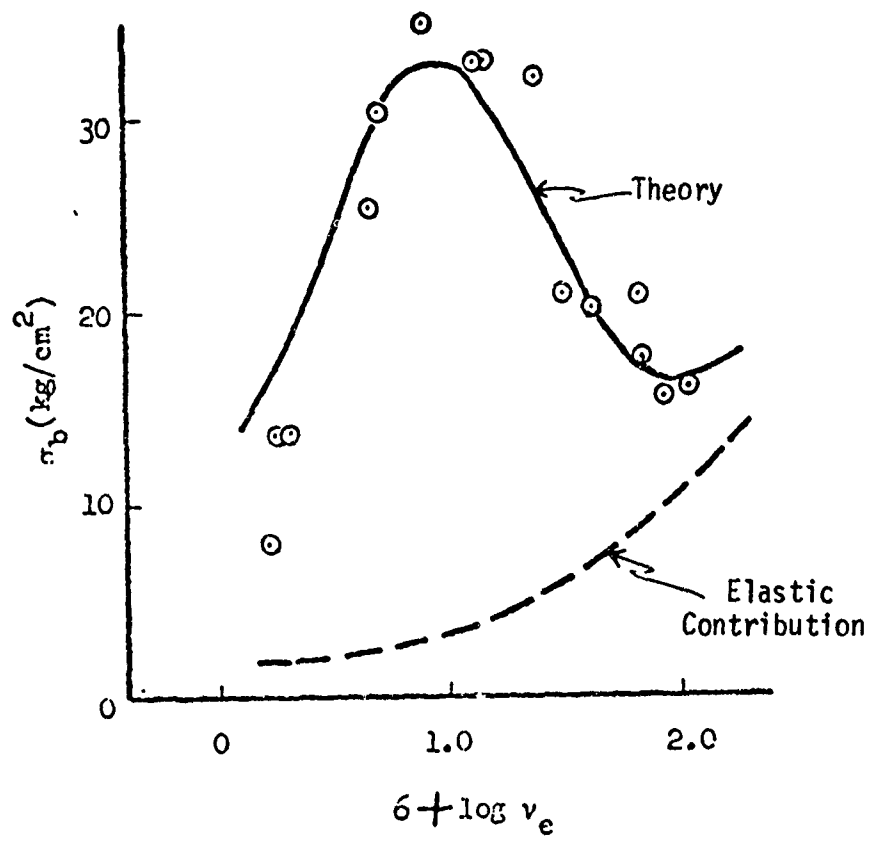


Figure 41. Strength of Unextracted SBR at an Extension Rate of 5 min.^{-1} . (Copied from Bueche and Dudek).

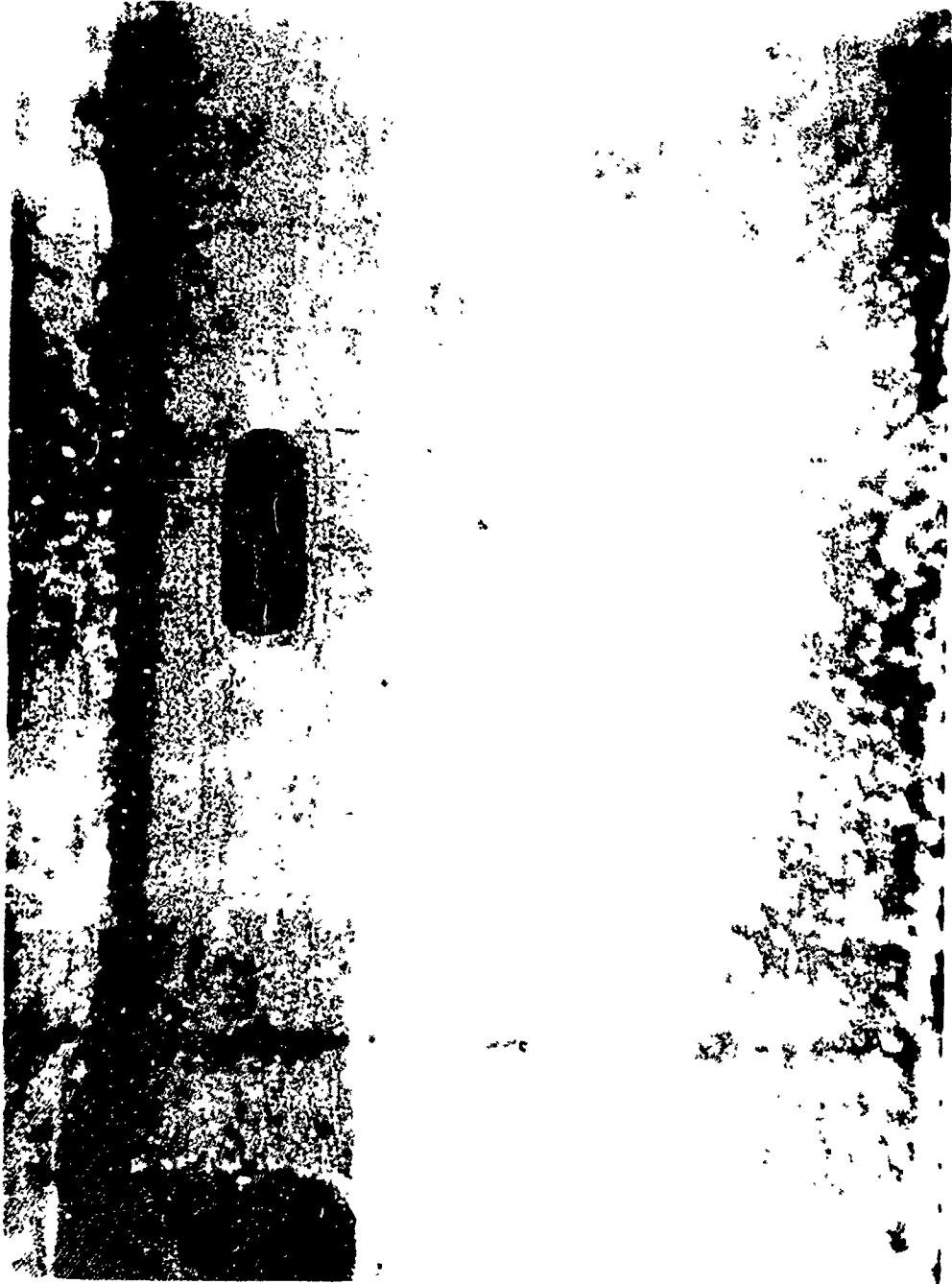


Figure 42. Shape of the Crack Tip at Failure Initiation for a Polyurethane

Propellant at -65°F

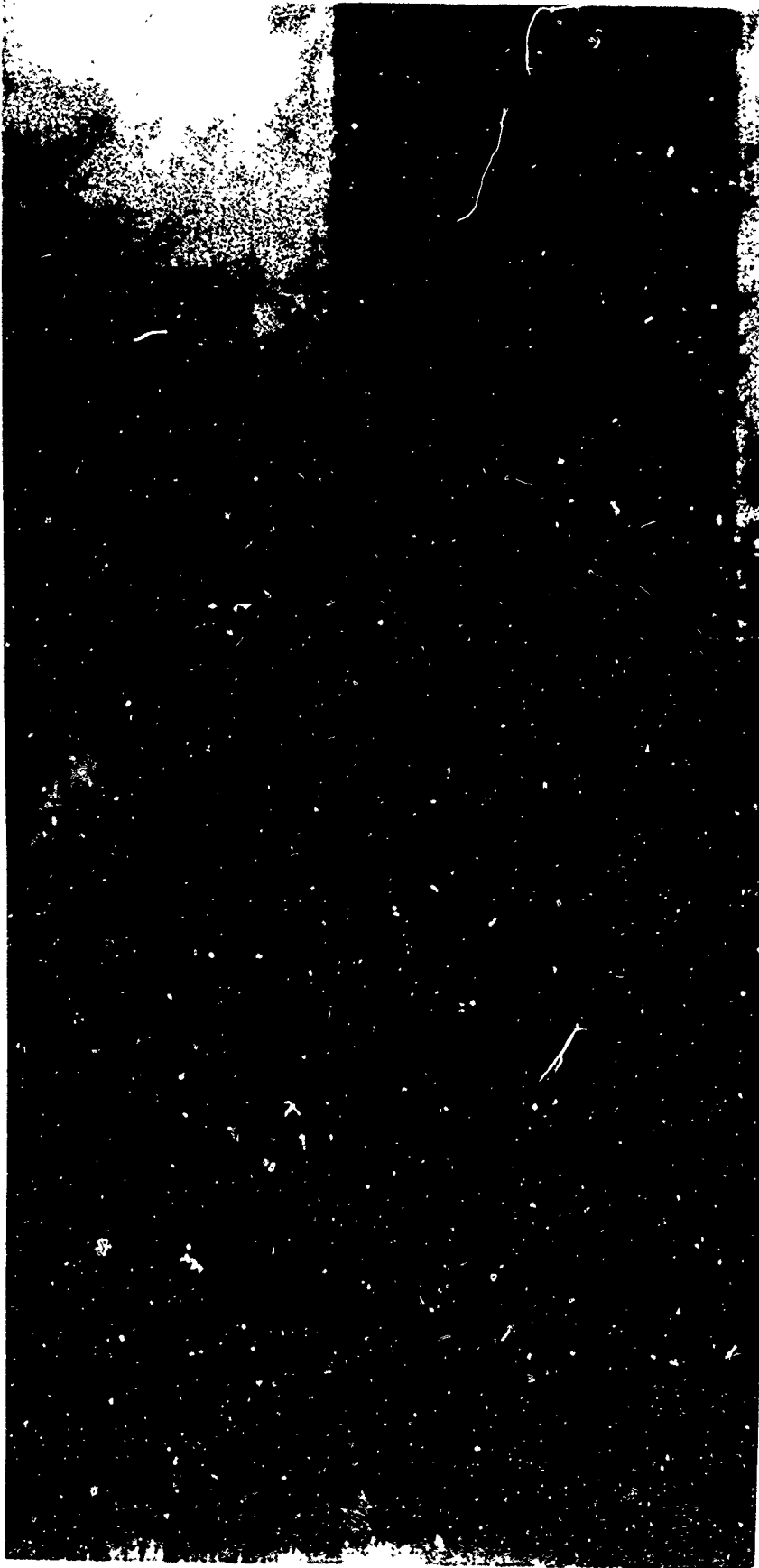


Figure 43. Shape of Crack Where the Initial Razor Cut was Slightly Canted
(Polyurethane Propellant at -65°F)

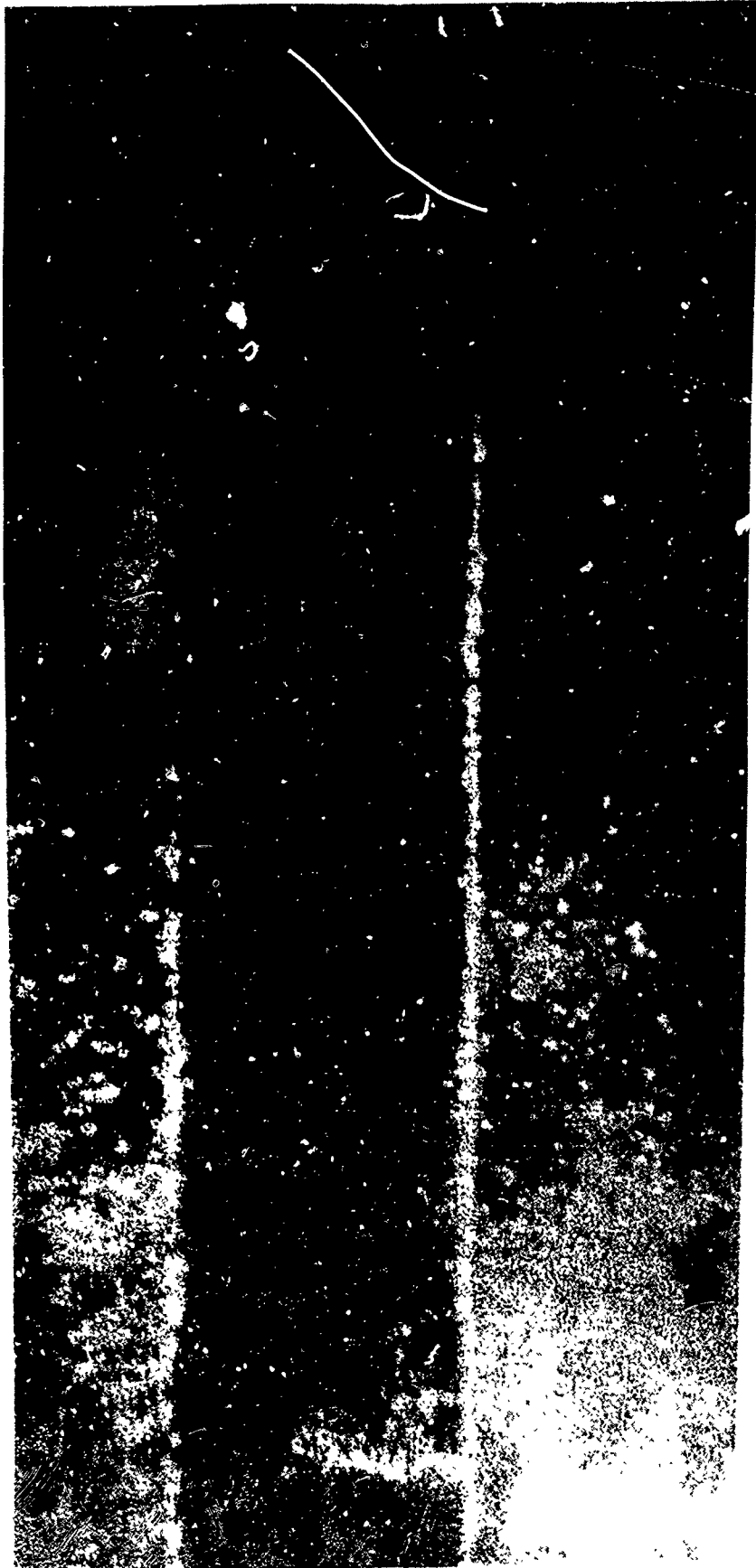


Figure 44. Failure Initiation Ahead of the Crack Tip in a Polyurethane
Propellant at -65°F

In summary, we feel that a material characterization method that gives sharp cracks must be used in the future.

Dependence of Low-Strain Moduli on Dewetting

Dewetting in propellants appears very early in the straining process. This is readily observed in careful stress-strain measurements of end-bonded test specimens. A typical stress-strain curve is illustrated in Figure 45. It is concave downward, the modulus continually decreasing with increasing strain. Schapery (36) noted this behavior of propellant and made tests showing that stress relaxation moduli taken at 0.25% strain were four to six times those taken at 3% strain.

Francis (21) separately noted the effect of strain level upon stress relaxation moduli, while Adicoff and Lepie (22) drew the conclusion that the dewetting effect causes the propellant to deviate from thermomechanical simplicity. In particular, they noted that the time-temperature shift factor, a_T , is modified by the strain level.

With respect to Equation (1) this strain level dependency is of major importance. If r is to be evaluated as a valid constant, it will be necessary to obtain accurate values of the relaxation moduli.

It is recommended that the various available techniques be evaluated for accurate moduli determinations at strain levels in the vicinity of 0.25% strain.

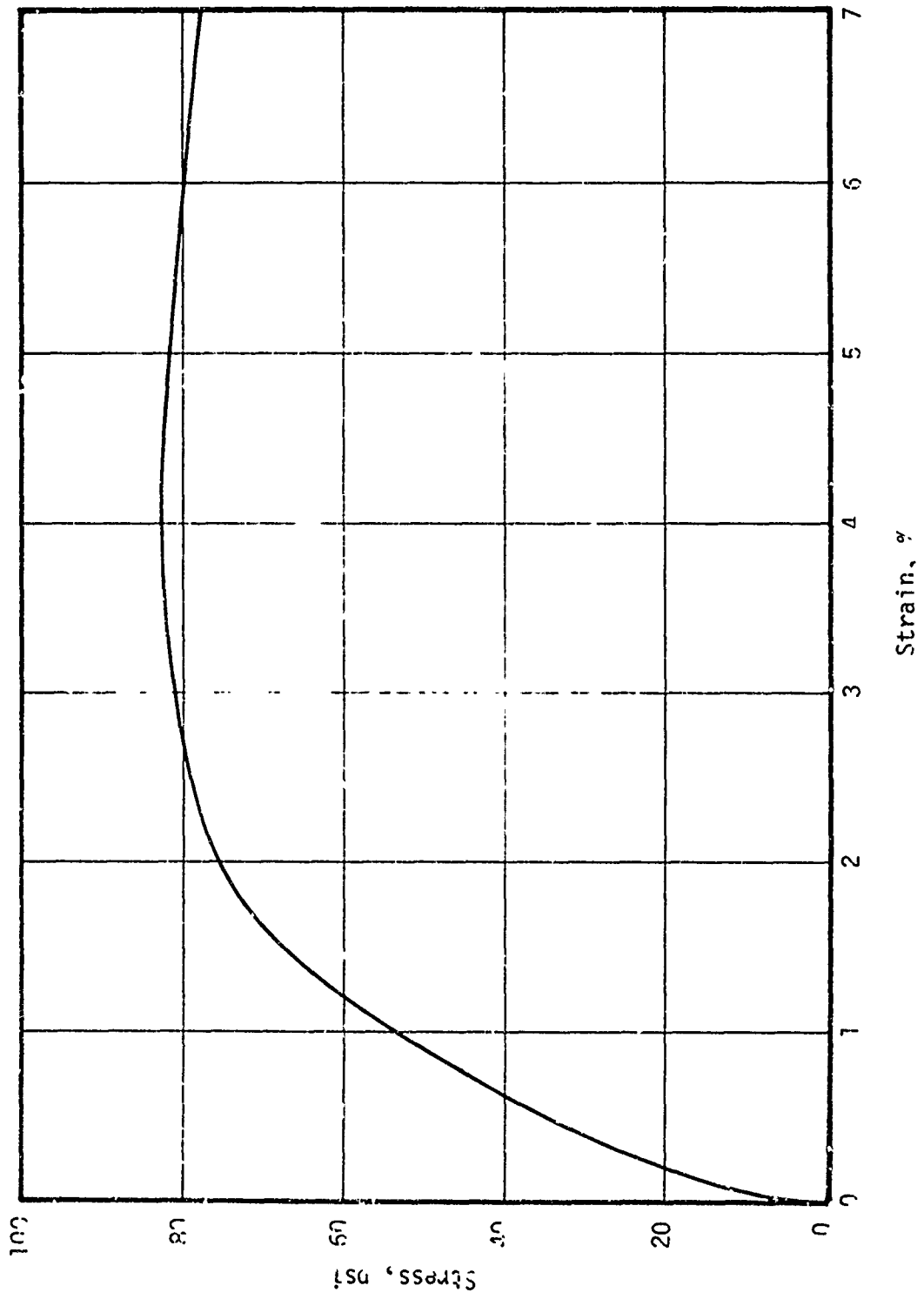


Figure 45. Stress-Strain Curve for a Polyurethane Binder Filled with 80 wt. % Glass Beads

THEORY - INTRODUCTION

(A New Approach to Solid Propellant Mechanical Behavior)

Basic Response Processes

Solid propellant material is a composite of rigid incompressible filler particles (roughly spherical) entrained in an incompressible rubber matrix. When such a composite is deformed mechanically, the rubber stores elastic strain energy and the binder pulls away from the filler, producing a modest amount of dilatation in the composite structure. In addition the rubber may dissipate the stored energy viscoelastically and the filler particles may slip relative to the binder, causing additional dissipation. In the theory that we present below, these dissipation effects are neglected; the intent is to extend the theory in a later development program to include such effects. Thus, we are talking about rigid dewettable* filler particles in an incompressible rubber matrix.

We had available simple tensile data (all at 77°F) at various strain rates from 0.0125 to 1.25 min⁻¹ and at various superimposed pressures from 0 to 1000 psig. In the following section, we shall present a constitutive theory which correlates these data and determines the five parameters of the theory in a self-consistent fashion. The theory is relatively simple and completely physically motivated. In a nutshell, it postulates that the pull-away of the binder from the filler is controlled by the Griffith surface energy criterion.

Technical Background

The science of solid propellant mechanical behavior has had a long and fruitful history. In 1959, workers at Aerojet-General SRP painted circles on simple tensile specimens and photographed the subsequent deformation of these circles onto ellipses during simple tensile stretch. It was determined that Poisson's ratio decreased from an initial value of 1/2 to a value of about 1/4 at 40-50 percent strain. It was roughly in this period of time that workers in the field began to realize that the falloff in Poisson's ratio and the concatenates softening of the modulus (slope) of the tensile curve were in some way related to the pullaway of the binder from the filler, or to dewetting, as it is commonly called.

Roughly ten years later there appeared on the scene another Aerojet worker (Farris) who proposed a simple constitutive equation to explain this behavior (37, 38) namely:

$$\sigma = E\epsilon \left(1 - \beta \frac{\Delta}{\epsilon} \right) \quad (13)$$

* Although dewetting is used for simplicity in the descriptions, it should be apparent that tearing of the binder adjacent to the filler will lead to the same descriptive processes, and the same forms for the relations generated below.

This was the first example of a nonlinear elastic constitutive equation based on ideas other than those which stem from a strain energy function (it is easy to show that Equation (13) is not analytic). The importance of introducing a non-analytic function of this sort is that it made people realize that some other type of mathematics (besides finite elasticity) was needed to represent propellant behavior. Fitzgerald later suggested (1968) that one use semi-norms to handle the representation. Farris (39) working for Fitzgerald, put the idea on a physical basis by suggesting that the applied strain in a tensile test be constructed in a distributed fashion, and that the distribution be limited by the ratio of a critical strain to a semi-norm of the history of the strain. Farris' rationalization of the use of the semi-norm of the history of the strain is that it is a chronological counter of damage.

Taking this cue from work such as Farris', Lindsey (40) suggested that an alternative approach to representing the damage mechanism existed in the form of classical plasticity. An objection exists to the use of plasticity however from the standpoint that a propellant can evidence marked hysteresis and no permanent set.

Farris' idea of a chronological counter of damage in the form of a semi-norm has proved very fruitful. This same idea however has led to the introduction of a large number of semi-norm terms of various orders which do not easily line up with physical concepts. It is the desire to provide a completely physical theory that leads the present investigator to propose a damage criterion based on completely physical ideas and physically-motivated mathematics.

Furthermore, it is recognized by many workers in the field today that it is possible to replace classical plasticity, with its yield criterion, by a completely differential theory which involves a semi-norm in the form of a chronological counter. For example, in the case of simple tension, following workers like Rivlin, Pipkin, and Farris, one can write

$$\dot{\sigma} + \beta |\dot{\epsilon}| \sigma = E \dot{\epsilon} \quad (14)$$

and generate hysteresis with no discontinuity in stress during loading. Equation (14) is just one example of many forms of the theory developed by Pipkin and Dag (41) using chronological variables of the form:

$$s = \sqrt{\dot{\epsilon}_\alpha \dot{E}_d} \quad (15)$$

Thus it appears that whether one introduces the damage mechanism via plasticity or via a Mullin's effect, one must use chronological variables which behave like semi-norms.

In the theory that we are about to propose, the role of the semi-norm is played by a physical parameter, namely the porosity that is generated by the pullaway of the binder from the filler. In this process of pullaway, new surface area is created and new surface energy is added to the deformed propellant. We use the Griffith criterion to control the rate of increase of the new surface energy.

In this approach to fitting data based on our theory, we shall assume that all the hysteresis is generated by the irreversibility of the porosity. We shall, therefore, use no hereditary integral, but will use a nonlinear measure of strain.

ANALYTICAL DEVELOPMENT

Generating the Physical Model

Roughly speaking, the maximum strain evinced by a solid propellant specimen subjected to simple tension is about 50 percent. Within this range of strain, only a mildly nonlinear constitutive equation is needed to fit the behavior of a purely elastic material. This statement implies the presence in the constitutive equation of only two moduli, the shear modulus and the bulk modulus. Because the binder pulls away from the filler particle, these two moduli soften with increasing strain. This demands that the theory be even more nonlinear. One way of handling this, as suggested by Farris and Schapery is to make the shear modulus a decreasing function of the dilatation, and the bulk modulus a decreasing function of the octahedral shear strain. Such an approach is subject to two limitations. One is that the presently proposed forms such as Equation (13) are not consistent with linear theory in the limit of infinitesimal strain, while other forms, which are based on functions that are essentially empirical, lack physical motivation.

In an attempt to motivate the decrease of the shear modulus and the bulk modulus by a physical argument, we propose the following model.

We envisage the propellant rubber-filler matrix as a collection of unit spherical cells each with a dewetting cavity. As the propellant is strained, the cavity grows in proportion to the amount of new surface area that is produced when the binder pulls away from the filler (or tears in the rubber adjacent to the filler). In effect, our model treats the binder-filler matrix as a porous material in which porosity increases during loading, remains fixed during unloading (this makes it a physical semi-norm), and in which the porosity effects the bulk modulus and shear modulus in such a way that they decrease with increasing porosity. In turn, the rate of increase of the porosity with increasing strain is controlled by the Griffith criterion.

The physical model described above led to a straightforward mathematical relation. Testing of that model with actual propellant response data required only a minor correction for the case of superimposed hydrostatic pressures. These analytical relations are described below.

Choosing the Strain Energy Function

In dealing with nonlinear materials, there are a plethora of strain energy functions that can be used to describe elastic behavior. This is particularly true in dealing with materials (such as propellants) in which the tensile strain does not greatly exceed 50%. This nonlinearity is mild, and many functions describe elastic behavior up to 50% with equal accuracy. For the initial studies we chose the following function:

$$W = AI_e + B\Delta \quad (16)$$

Where W is the elastic strain energy function

I_e is the first strain invariant

Δ is the dilatation

A and B are constants

The first strain invariant, I_e , is defined as follows:

$$I_e = \sum \epsilon_\alpha \quad (17)$$

Geometrical nonlinearity is introduced into this relation through the strain, which we choose to be Seth's n -measure (23), namely:

$$\epsilon_\alpha = \frac{\lambda_\alpha^n - 1}{n} \quad (18)$$

Where $\{\lambda_\alpha\}$ are the principal stretch ratios n

n is an empirical constant which determines the measure of the strain

An additional geometrical nonlinearity is provided by the dilatation term.

$$\Delta = \frac{J^{-\beta} - 1}{\beta} \quad (19)$$

Where $J (= \pi \lambda_a)$ is the dilatation ratio

β is an empirical constant

Inserting Equations (17), (18) and (19) into Equation (16) gives the following strain energy relation

$$W = A \sum \left(\frac{\lambda_\alpha^n - 1}{n} \right) + B \left(\frac{J^{-\beta} - 1}{\beta} \right) \quad (20)$$

Although Equation (20) generates a linear stress-strain law, it is both materially and geometrically nonlinear. It is materially nonlinear because the constants A and B (as will be shown) depend indirectly on the stress through the porosity; it is geometrically nonlinear because of the strain and dilatation measures, Equations (18) and (19).

Parameter Determination

The parameters A, B, n and β in Equation (20) are determined by the fact that W must reduce to Hookean behavior in the limit of small strain. We proceed as follows:

$$J^n = \pi \lambda_{\alpha}^n = \pi (1 + n \epsilon_{\alpha}) = 1 + n I_{\epsilon} + n^2 II_{\epsilon} + n^3 III_{\epsilon} \quad (21)$$

$$J^{-\beta} = 1 - \beta (I_{\epsilon} + n II_{\epsilon} + \dots) + \frac{\beta}{n} \left(\frac{\beta}{n} + 1 \right) (n^2 I_{\epsilon}^2 + \dots) + \dots \quad (22)$$

When Equations (21) and (22) are introduced into Equation (20), we obtain:

$$W = A I_{\epsilon} - B I_{\epsilon} - B n II_{\epsilon} + \frac{B}{2} (\beta + n) I_{\epsilon}^2 + \dots \quad (23)$$

In the limit of small strain, we have:

$$0 = A - B \quad (24)$$

$$-2G = -nB \quad (25)$$

$$K + \frac{4}{3}G = B(\beta + n) \quad (26)$$

or

$$A = B = \frac{2G}{n} \quad (27)$$

$$\beta = n \frac{K - \frac{2}{3}G}{2G} \quad (28)$$

Where G is the elastic shear modulus of the propellant.

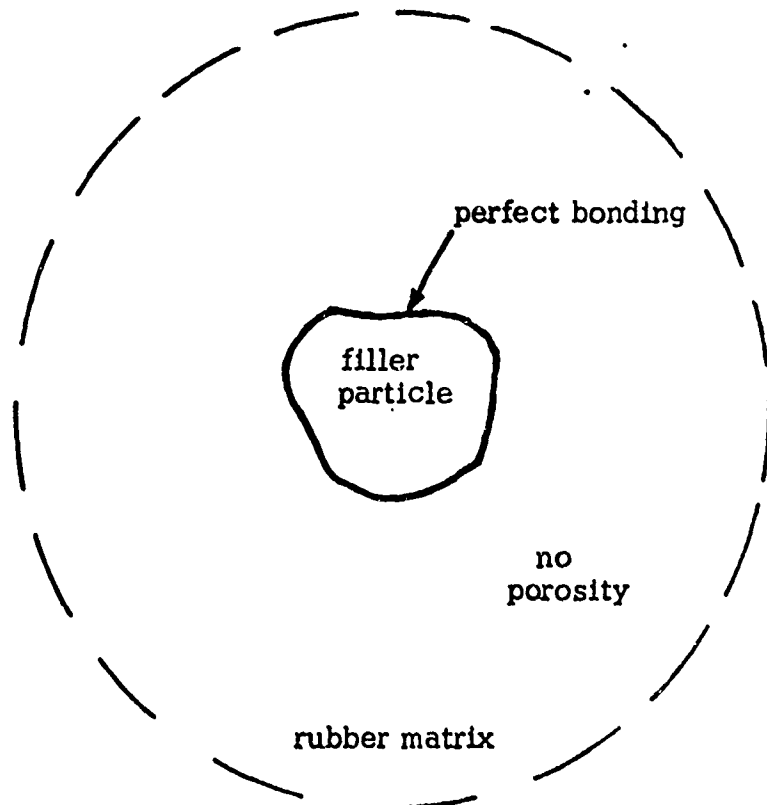
K is the elastic bulk modulus of the propellant.

Thus, our strain energy function is given by:

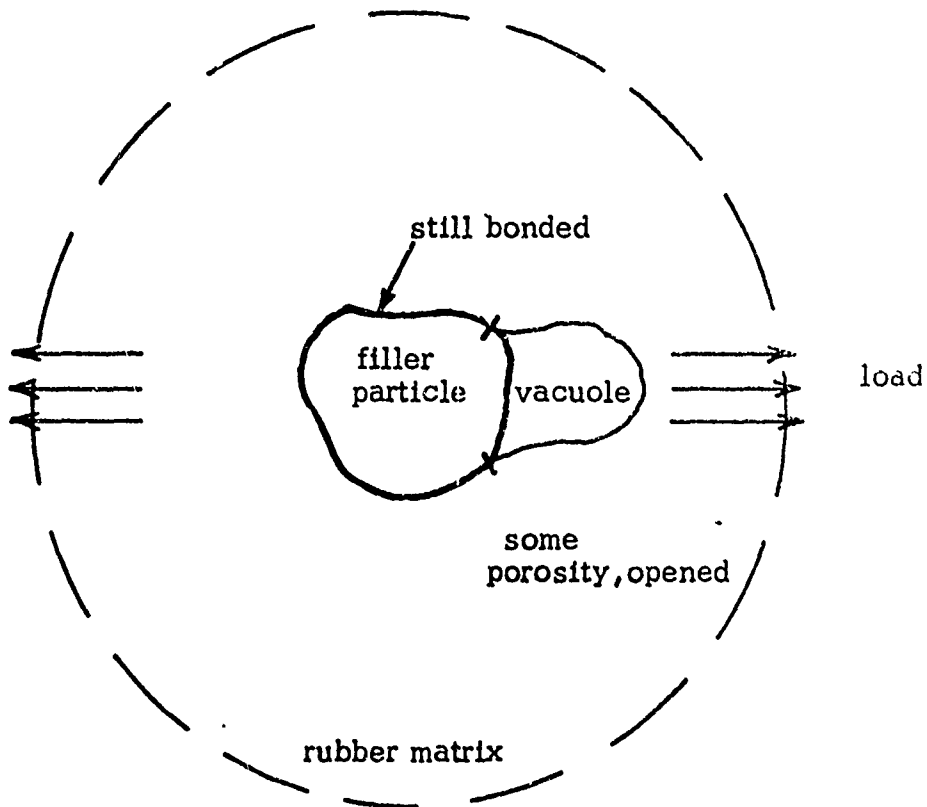
$$W = \frac{2G}{n} \left[\Sigma \left(\frac{\lambda_{\alpha}^n - 1}{n} \right) + \frac{J^{-\beta} - 1}{\beta} \right] \quad (29)$$

Thus, the elastic potential contains three parameters (n , G , and K). Such a strain energy function will describe the elastic behavior of many rubber-like materials reasonably well up to 50% strain, or thereabouts. The actual form that we have chosen is unimportant because of the flexibility provided by the parameter n that measures the strain hardening or strain softening response of the rubber. The constant n may be positive or negative and is not limited to integral values.

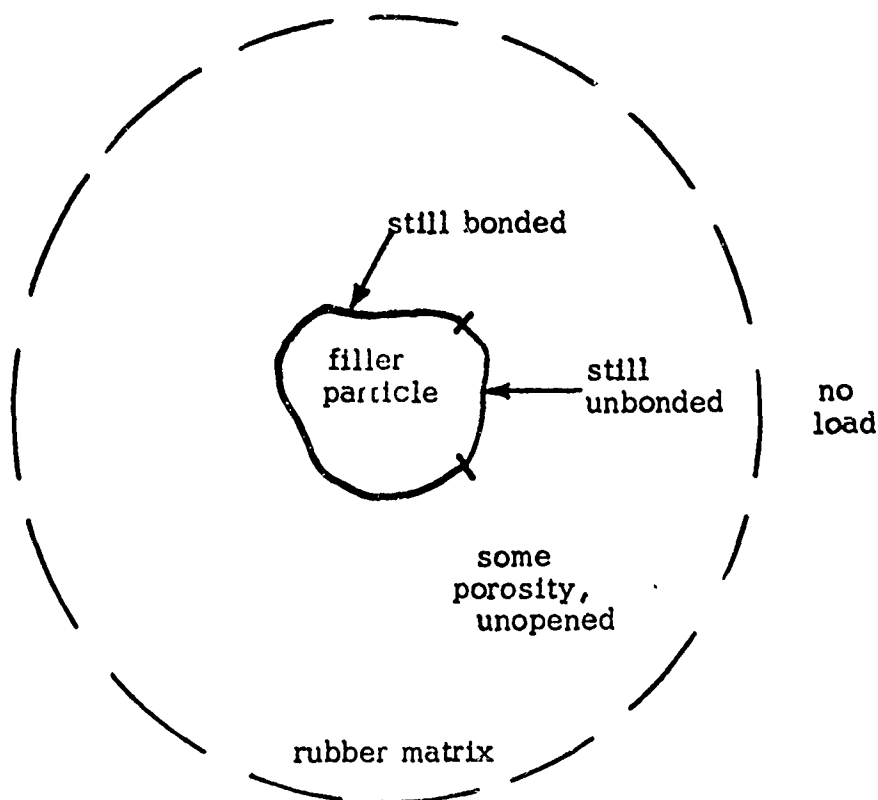
Now the fact of the matter is, solid propellant materials evince hysteresis upon unloading. One way of explaining this is that the two moduli G and K soften during loading and remain fixed during unloading. In order to represent this mathematically, we postulate that G and K depend upon a parameter γ which is physically related to the area fraction of dewetted particles, and which is controlled by the Griffith criterion. Our picture is as follows. In a virgin propellant, we have zero unbonding or zero dewetting as shown below:



After loading, some of the bonds tear and dewet and we have:



After unloading we have:



We construct a simple model as follows. Assume the unit cell to be a sphere of radius b containing rubber matrix inside of which is a rigid filler particle of radius a . The contact area, ϕ between the spherical particle and the rubber matrix (whether bonded or unbonded) is given by:

$$\phi = \frac{4\pi a^2}{\frac{4\pi}{3} b^3} = \frac{3(a^2)}{b} \quad (30)$$

where ϕ is the area per unit cell volume.

The volume fraction of filler particles, v_f , is given by:

$$v_f = \frac{a^3}{b^3} \quad (31)$$

so that:

$$\phi = \frac{3}{b} v_f^{2/3} \quad (32)$$

Let us now denote the fraction of the area that is unbonded by δ . Then the unbonded area per unit cell volume is given by:

$$\delta\phi = \frac{3}{b} v_f^{2/3} \delta \quad (33)$$

If we denote the specific surface energy associated with the unbonded area by Γ , then the total surface energy of the unbonded region per unit cell volume is given by:

$$\frac{U_3}{V^+} = \frac{3}{b} v_f^{2/3} \Gamma \delta \quad (34)$$

Where U_3 is the total surface energy of the sample

V^+ is the volume of the undeformed sample

The parameter γ (which determines the softening in G and K) is a measure of the porosity that develops when an unbonded area under load opens up into a vacuole as shown in the second sketch above. Workers in the field of geophysics (42) have shown that effective moduli can be defined in terms of γ in the form:

$$G_e = G \frac{1 - \gamma}{1 + \frac{\gamma}{4}} \quad (35)$$

and

$$K_e = \frac{4}{3} G \frac{1 - \gamma}{\gamma} \quad (36)$$

Equations (35) and (36) are easily derived by solving the elastic problem of a porous sphere under load, averaging the stress field, and then defining effective moduli.

Having introduced effective moduli, we rewrite Equations (28) and (29) as:

$$W = \frac{2G_e}{n} \left[\lambda_\alpha \left(\frac{\lambda_\alpha^n - 1}{n} \right) + \frac{J^{-\beta} - 1}{\beta} \right] \quad (37)$$

and

$$\beta = n \frac{K_e - \frac{2}{3} G_e}{2G_e} \quad (38)$$

We now postulate that γ and δ are related by:

$$\gamma = k\delta^m \quad (39)$$

Where k and m are constants

Equation (39) states that the porosity γ which occurs under load is a nonlinear function of the area fraction of unbonded matrix δ . Because the actual determination of the porosity via a stress analysis is an extremely difficult problem and because of interactions between adjacent cells, we prefer to eschew this difficult analysis, and introduce one extra parameter m , an interaction parameter, into the theory. The proportionality constant k will turn out to be absorbed into the fourth parameter, which is the surface energy.

Stress-Strain Relations

The stress-strain law is given by:

$$\lambda_\alpha \sigma_\alpha = \bar{\sigma}_\alpha J = \lambda_\alpha \frac{\sigma W}{\sigma \lambda_\alpha} = \frac{2G_e}{n} (\lambda_\alpha^n - J^{-\beta}) \quad (40)$$

where

σ_α is the principal Piola stress

and

$\bar{\sigma}_\alpha$ is the principal Cauchy stress

The power input to a sample is given by:

$$\dot{\mathcal{P}} = V^+ \sigma_\alpha \dot{\lambda}_\alpha \quad (41)$$

The total strain energy, U_1 , is given by:

$$U_1 = V^+ W \quad (42)$$

The total surface energy is given by:

$$U_3 = V^+ \frac{3}{b} v_f^{2/3} \Gamma \left(\frac{\gamma}{k} \right)^{1/m} \quad (43)$$

and the Griffith criterion postulates that:

$$\dot{\mathcal{P}} = \dot{U}_1 + \dot{U}_3 \quad (44)$$

where the dots denote time derivatives.

We now turn to the case of simple tension with superimposed hydrostatic pressure. For this case, we have:

$$\lambda_1 = \lambda \quad (45)$$

$$\lambda_2 = \lambda_3 = \sqrt{\frac{J}{\lambda}} \quad (46)$$

$$\bar{\sigma}_1 = S - P \quad (47)$$

$$\bar{\sigma}_2 = \bar{\sigma}_3 = -P \quad (48)$$

Upon substituting into Equation (40), we obtain:

$$SJ = \frac{2G_e}{n} \left[\lambda^n - \left(\frac{J}{\lambda} \right)^{n/2} \right] \quad (49)$$

$$PJ = \frac{2G_e}{n} \left[J^{-\beta} - \left(\frac{J}{\lambda} \right)^{n/2} \right] \quad (50)$$

After some simplification, Equation (44) reduces to:

$$\begin{aligned} \frac{40}{n(4+\gamma)^2} \left[\frac{\lambda^n + 2 \left(\frac{J}{\lambda} \right)^{n/2} - 3}{n} + \frac{J^{-\beta} - 1}{\beta} \right] - \frac{16}{3\beta\gamma^2} \left[\frac{1-\gamma}{4+\gamma} \frac{J^{-\beta} - 1}{\beta} + J^{-\beta} \ln J \right] \\ = \frac{3\Gamma v_f^{2/3} \gamma^{\frac{1-m}{m}}}{bG mk^{1/m}} \quad (51) \end{aligned}$$

Equations (49), (50), and (51) complete define S and P in terms of λ , J, and γ .

EXPERIMENTAL EVALUATION OF CHARACTERIZATION PARAMETERS

For this effort we will define a new constant M as follows.

$$M = \frac{\Gamma v_f^{2/3}}{bG mk^{1/m}} \quad (52)$$

Thus, the basic material characterization requires the evaluation of four parameters n, G, m and M. The problem is to work backwards from available data and determine these four parameters in a self-consistent fashion. First we set:

$$\lambda = e^\epsilon \quad \text{or} \quad \epsilon = \ln \lambda \quad (53)$$

$$J = e^\Delta \quad \text{or} \quad \Delta = \ln J \quad (54)$$

whereupon Equation (49) may be rewritten:

$$\frac{1 - \gamma}{1 + \frac{\gamma}{4}} = \frac{G e}{G} = \frac{\frac{n}{2} \frac{S}{G} e^\Delta}{e^{n\epsilon} - e^{-n \frac{\epsilon - \Delta}{2}}} \quad (55)$$

Likewise Equation (50) may be rewritten:

$$n \frac{4 - \gamma}{6 \gamma} = \beta = - \frac{\ln \left[e^{-n \frac{\epsilon - \Delta}{2}} + \frac{P}{S} (e^{n\epsilon} - e^{-n \frac{\epsilon - \Delta}{2}}) \right]}{\Delta} \quad (56)$$

We now consider two cases. First, take the case P = 0. Since the strains we are dealing with do not exceed 50%, we can expand Equations (55) and (56) to second order and obtain:

$$\frac{1 - \gamma}{1 + \frac{\gamma}{4}} = \frac{G e}{G} = \frac{\frac{S}{E} \epsilon}{1 + \frac{n\epsilon}{4} - \frac{\Delta}{3\epsilon}} \quad (57)$$

and

$$\gamma = \frac{4\Delta}{3\epsilon - \Delta} \quad (58)$$

When we eliminate γ between Equations (57) and (58), we obtain:

$$\frac{S}{\epsilon^2} = \frac{En}{4} + E \left(\frac{\epsilon - 2\Delta}{\epsilon^2} \right) \quad (59)$$

Equation (59) suggests that a plot of (S/ϵ^2) vs $\frac{\epsilon - 2\Delta}{\epsilon^2}$ should yield a straight line with slope E and intercept $En/4$. In addition, when we expand Equation (51), we obtain:

$$\Delta = \left(\frac{3}{4}\right) M \epsilon^{-\frac{m}{1+m}} \quad (60)$$

which suggests that a log-log plot of Δ vs ϵ should determine M and m via slope and intercept.

Atmospheric Pressure Tests

Figures 46 to 50 display the log-log correlations of Δ vs ϵ for Farris' test data #1, 5, 6, 7, 8, and 10 at $\dot{\epsilon} = 0.5 \text{ min}^{-1}$, #2 at 0.25 min^{-1} ; #3 at 0.05 min^{-1} ; #4 at 0.0125 min^{-1} ; and #9 at 1.25 min^{-1} . In all cases, good straight lines are obtained. The slight departure from linearity at the higher strain levels arises from the fact that we approximated the fracture criterion by way of second-order expansions. If we had kept the complete function and put it on the computer, we could have developed complete linearity. For the test cases enumerated above, we find:

TABLE II

Parameter Evaluations from Tests at 77°F and 0 psig						
$\dot{\epsilon}, \text{ min}^{-1}$	0.0125	0.05	0.25	0.59	1.25	
m	0.55	0.54	0.51	0.56	0.57	$\langle m \rangle = 0.55$
M	0.070	0.079	0.089	0.091	0.076	$\langle M \rangle = 0.081$

Thus the fracture parameters m and M are remarkably constant and independent of strain rate.

Figures 51 to 55 display the linear correlation between (S/ϵ^2) and $\frac{\epsilon - 2\Delta}{\epsilon^2}$ for the same five data sets. For these cases, we find:

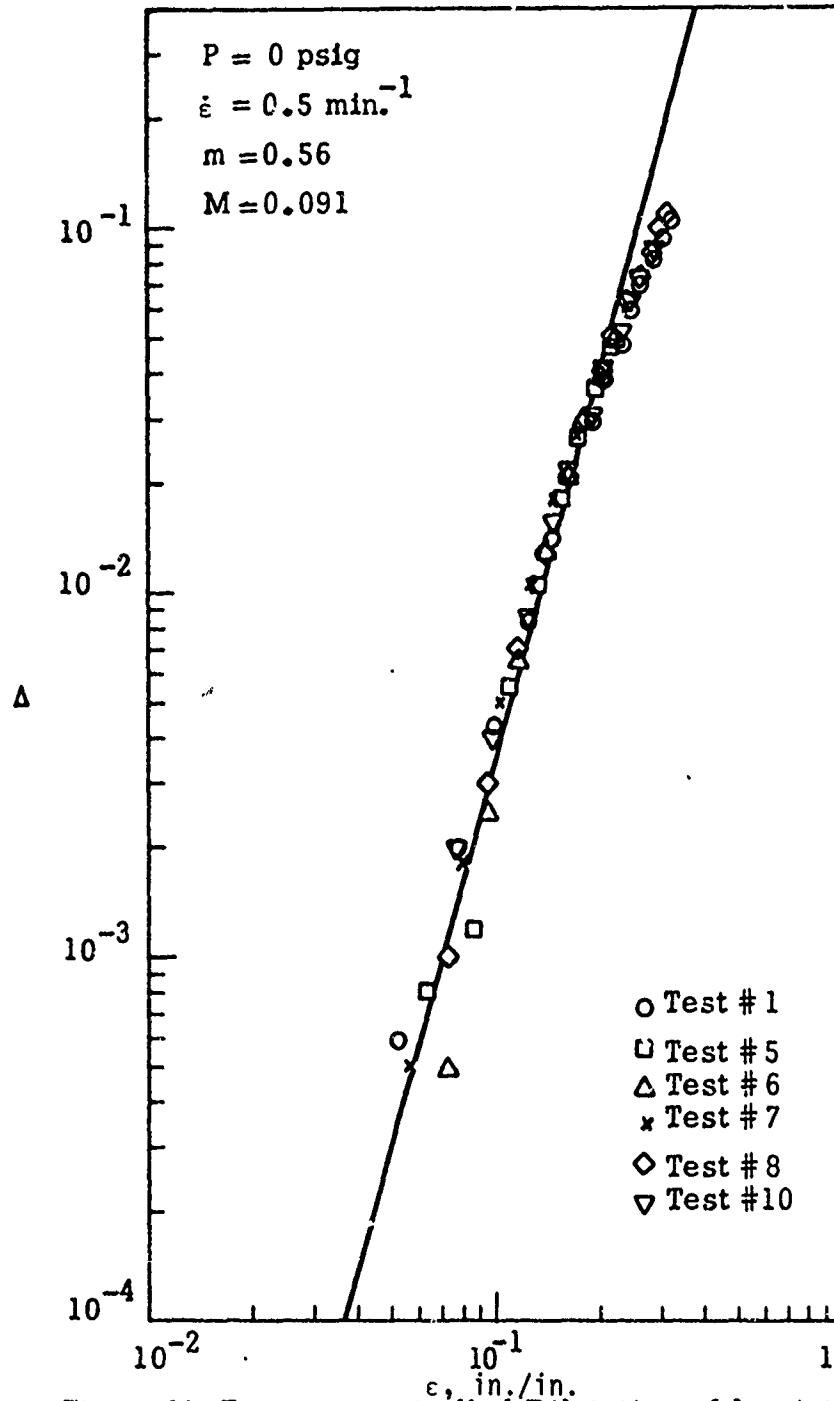


Figure 46. Fracture-controlled Dilatation of Aerojet CTPB Propellant

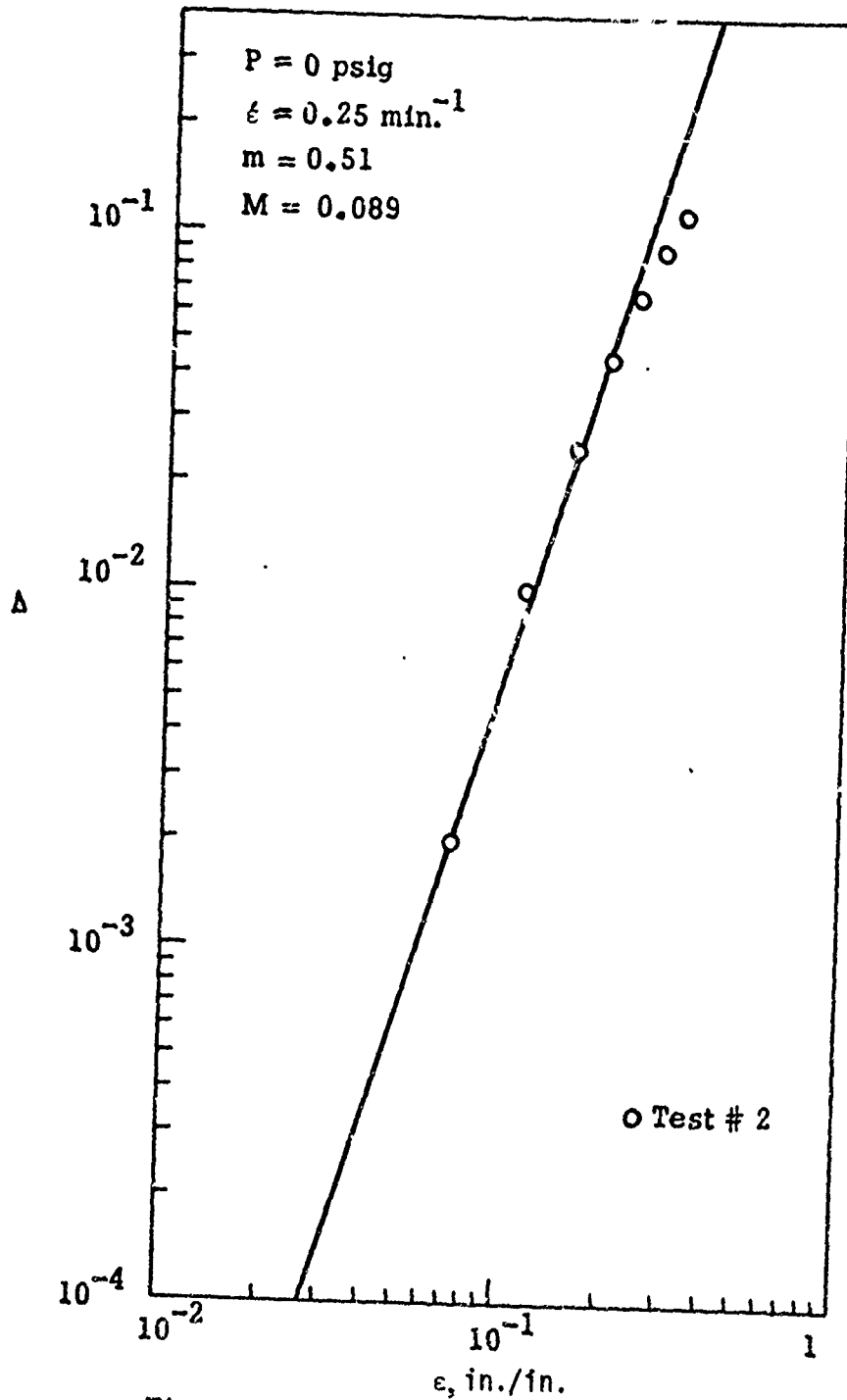


Figure 47. Fracture-controlled Dilatation of Aerojet CTPB Propellant

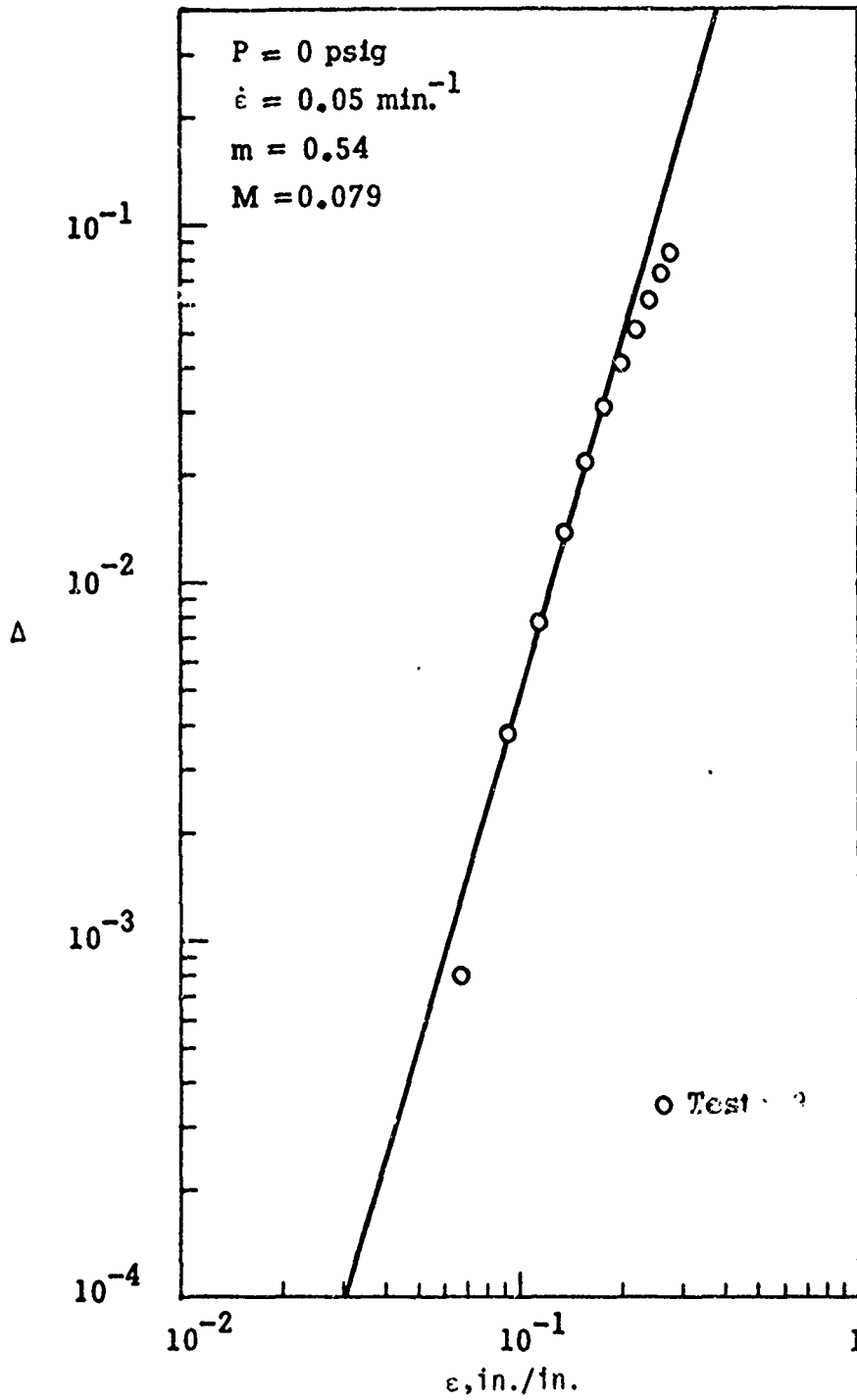


Figure 48. Fracture-controlled Dilatation of Aerojet CTPB Propellant

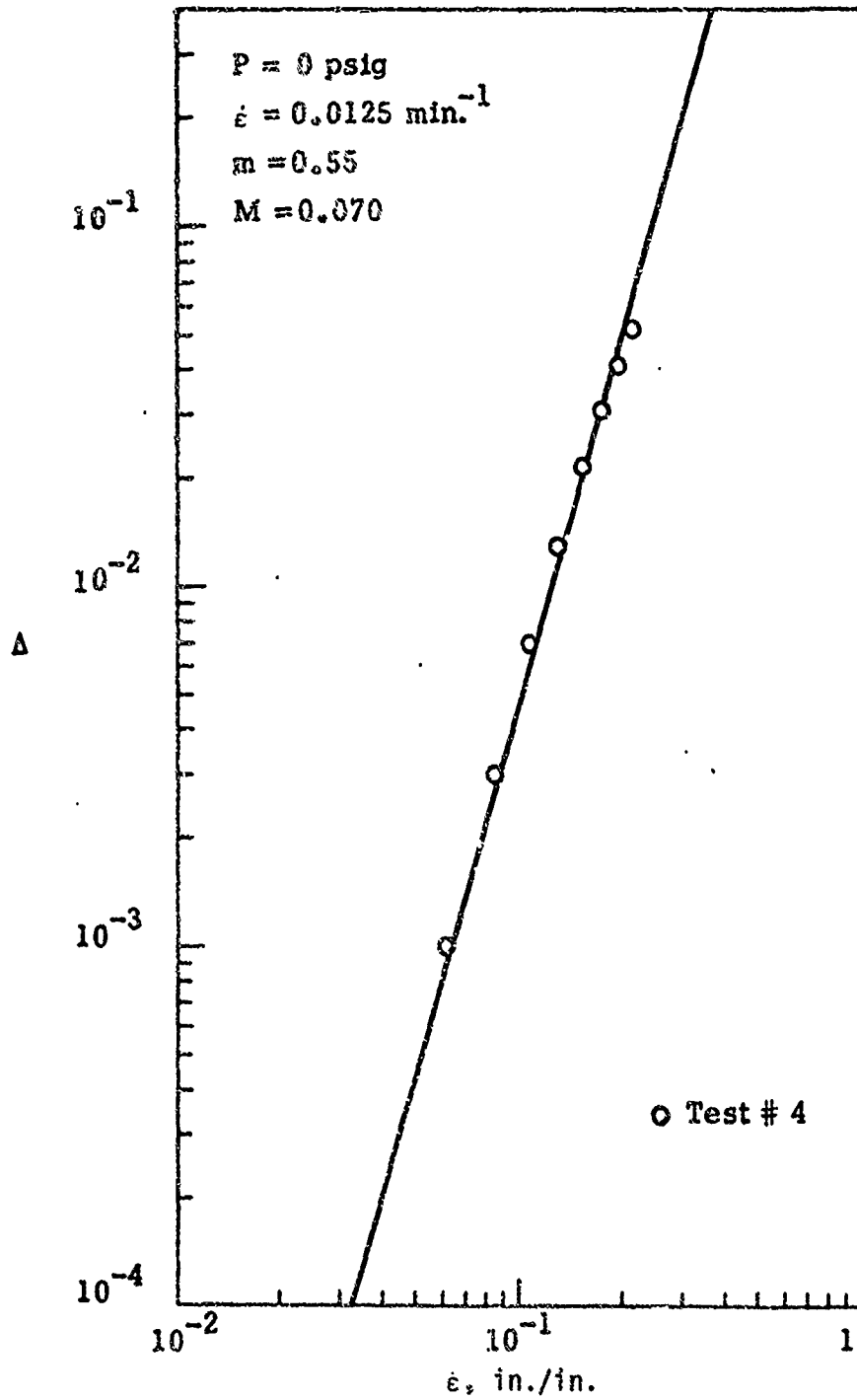


Figure 49. Fracture-controlled Dilatation of Aerojet CTPB Propellant

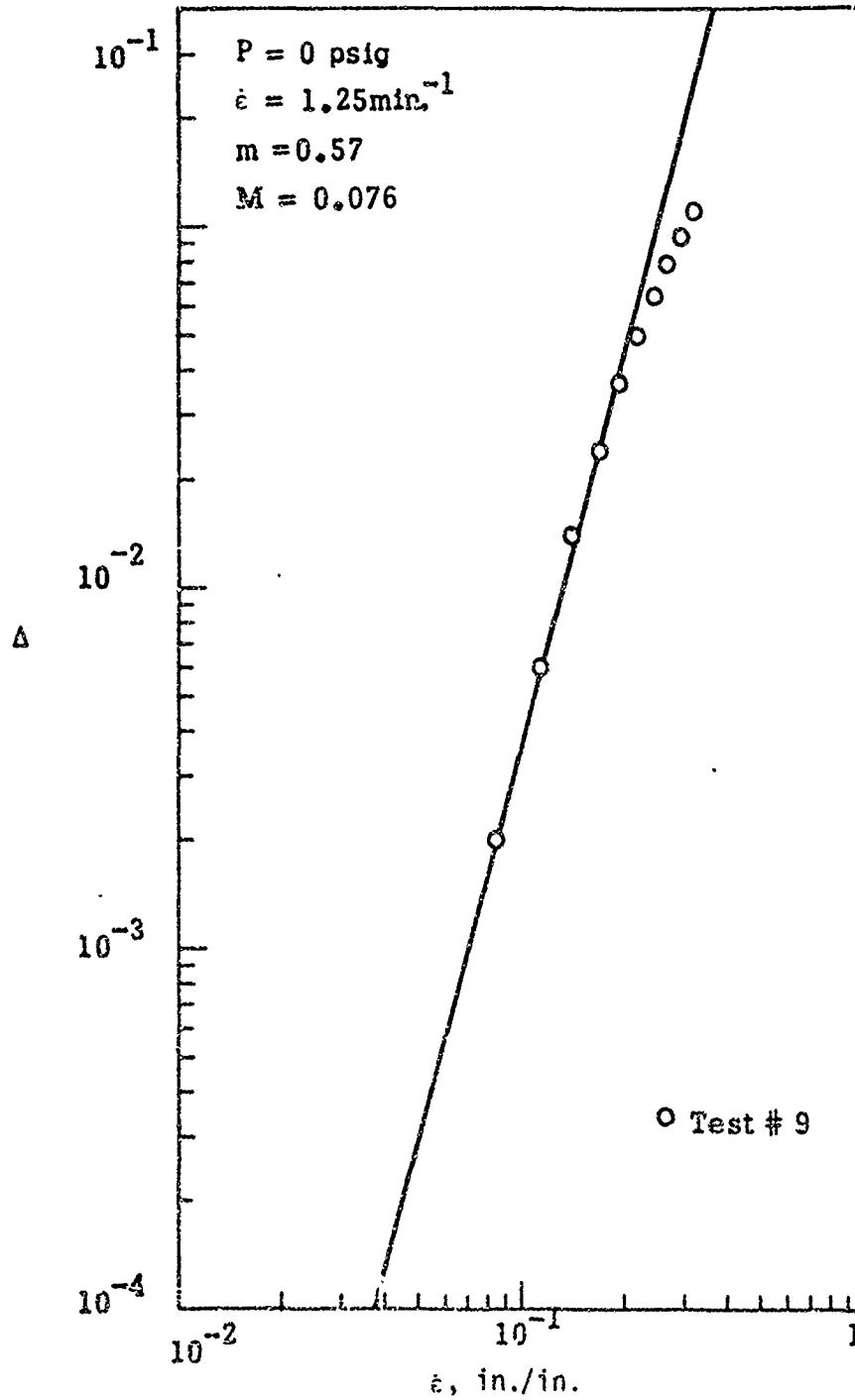
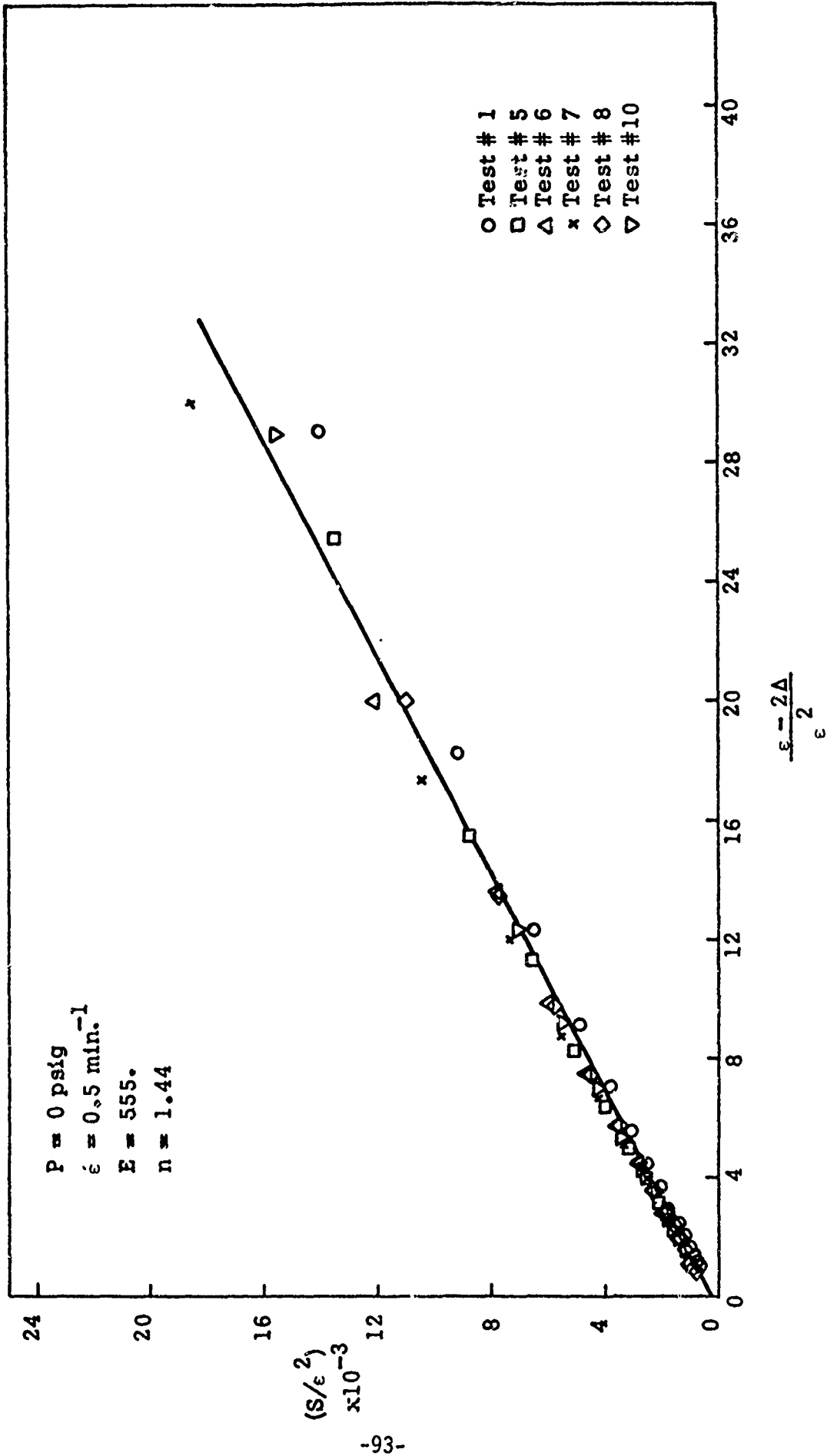


Figure 50. Fracture-controlled Dilatation of Aerojet CTPB Propellant



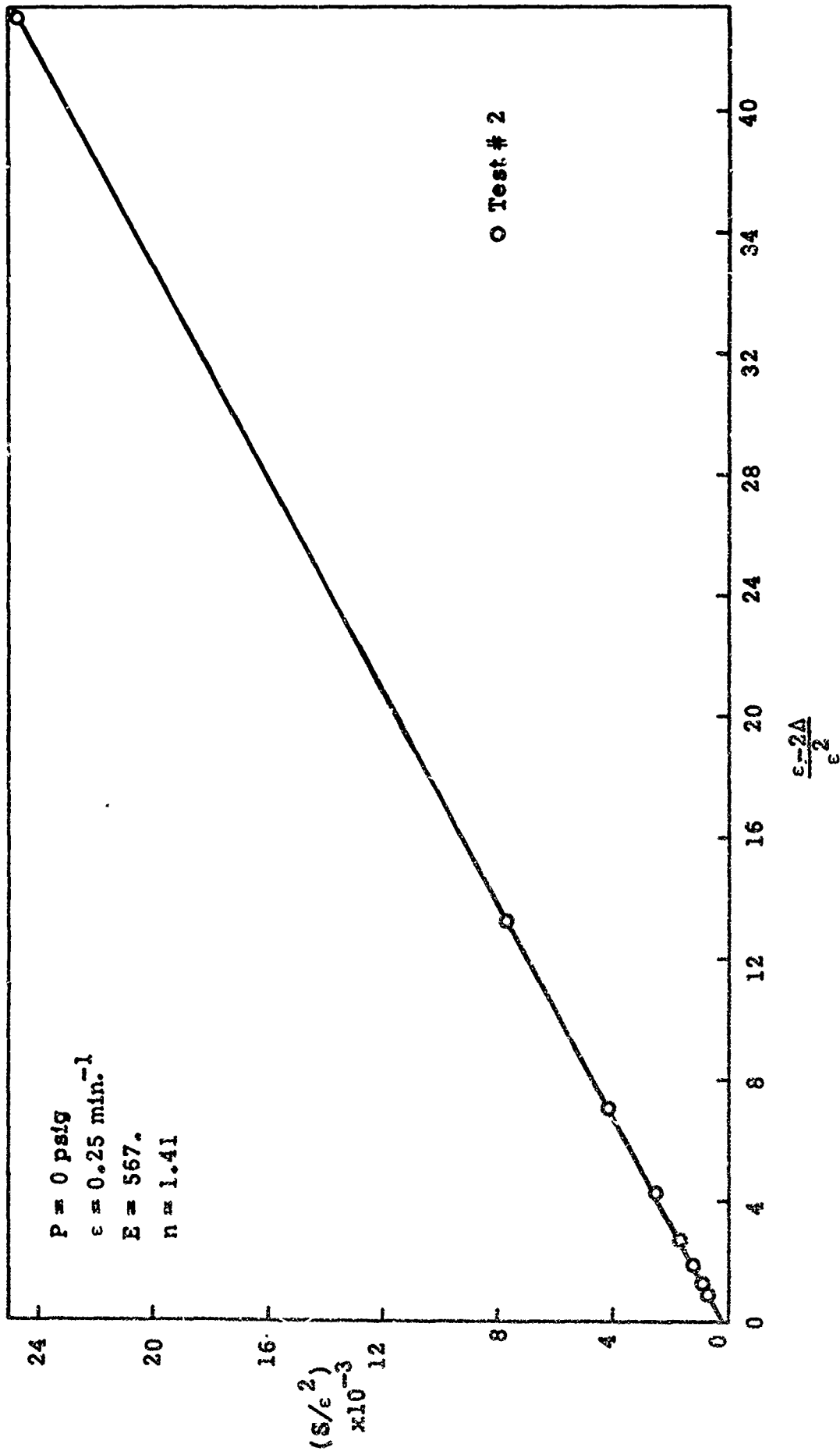


Figure 52. Fracture-controlled Simple Tensile Behavior of Aercjet CTPB Propellant

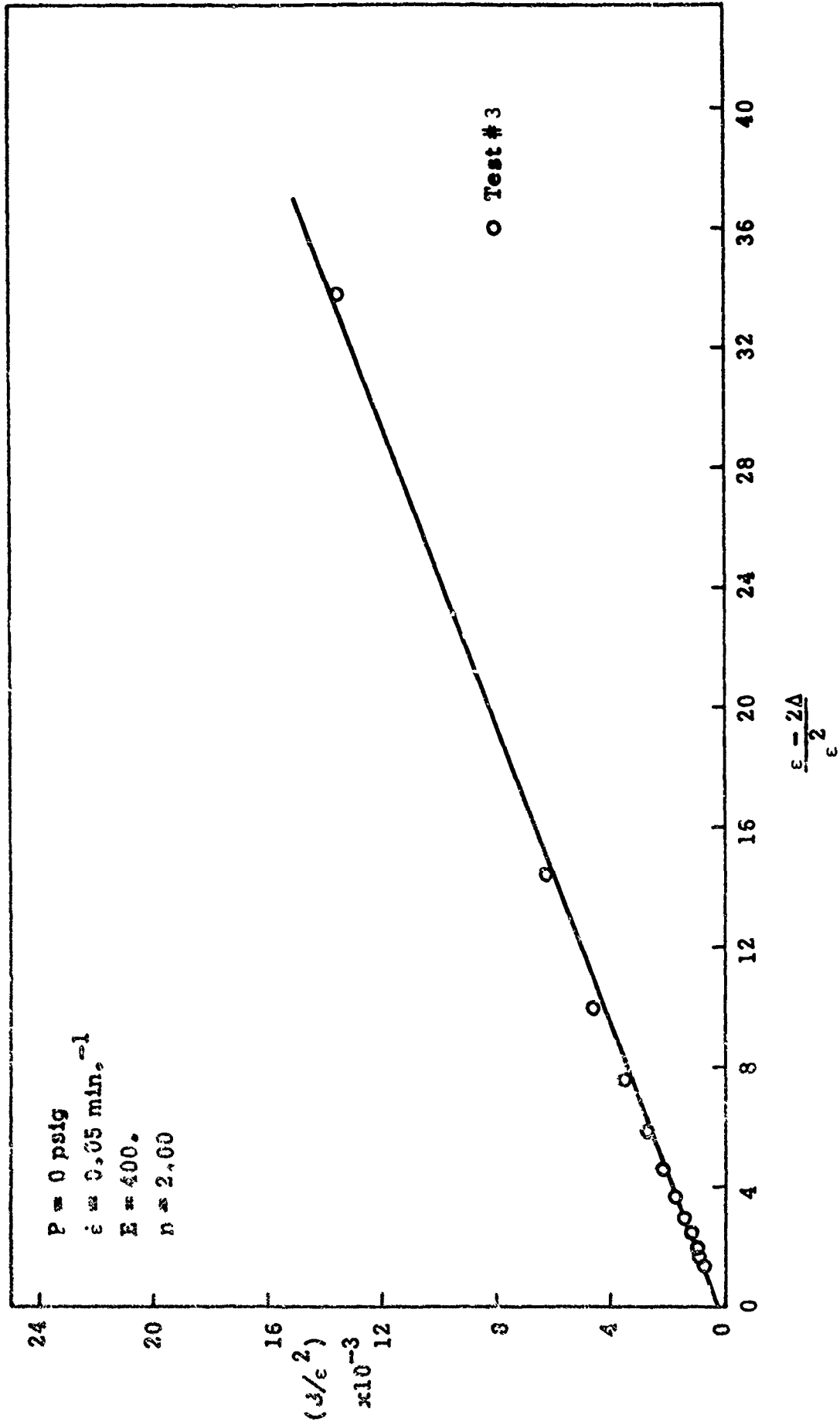


Figure 53. Fracture-controlled Simple Tensile Behavior of Aerojet CTPB Propellant

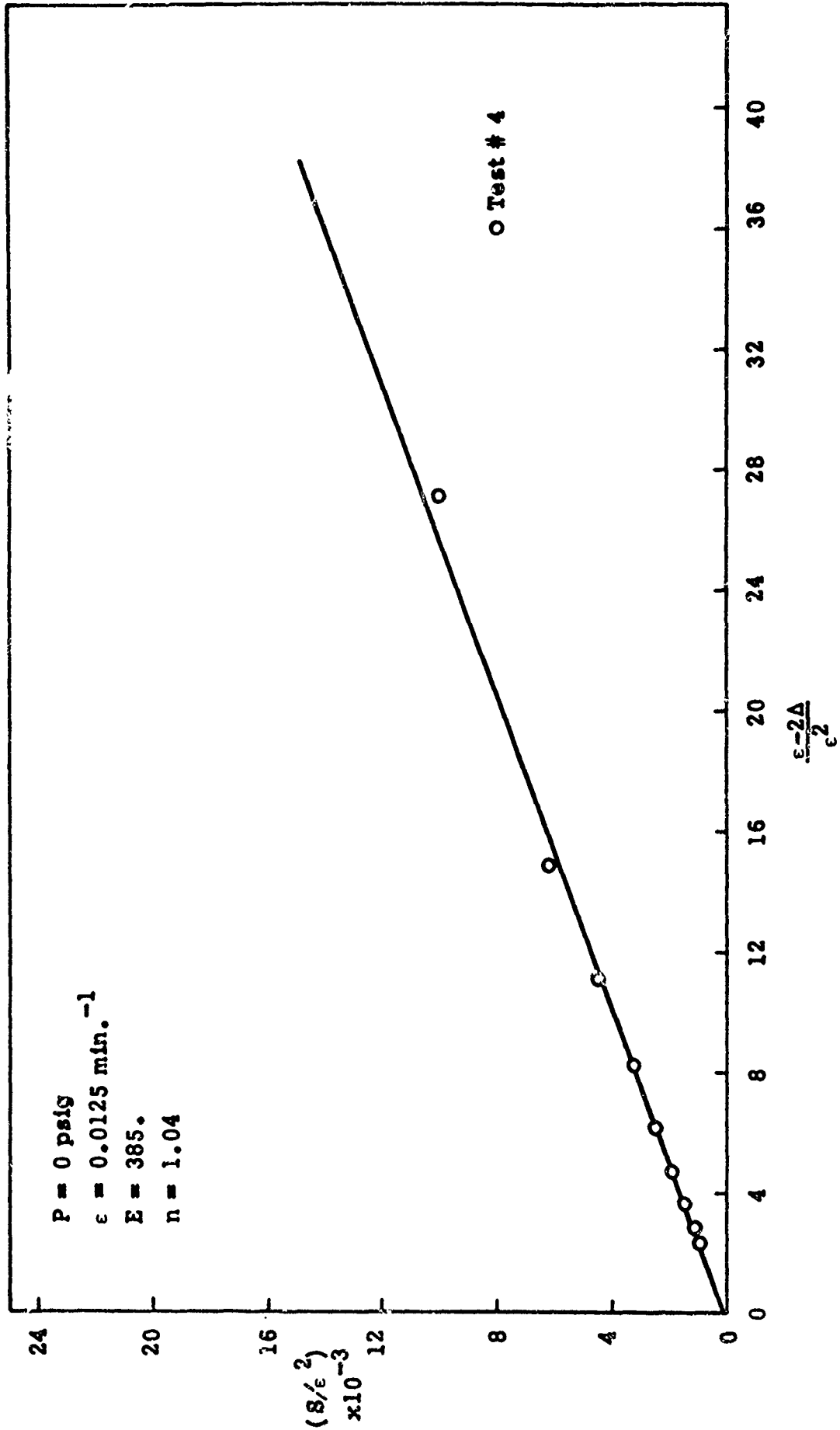


Figure 54. Fracture-controlled Simple Tensile Behavior of Aerojet CTPB Propellant

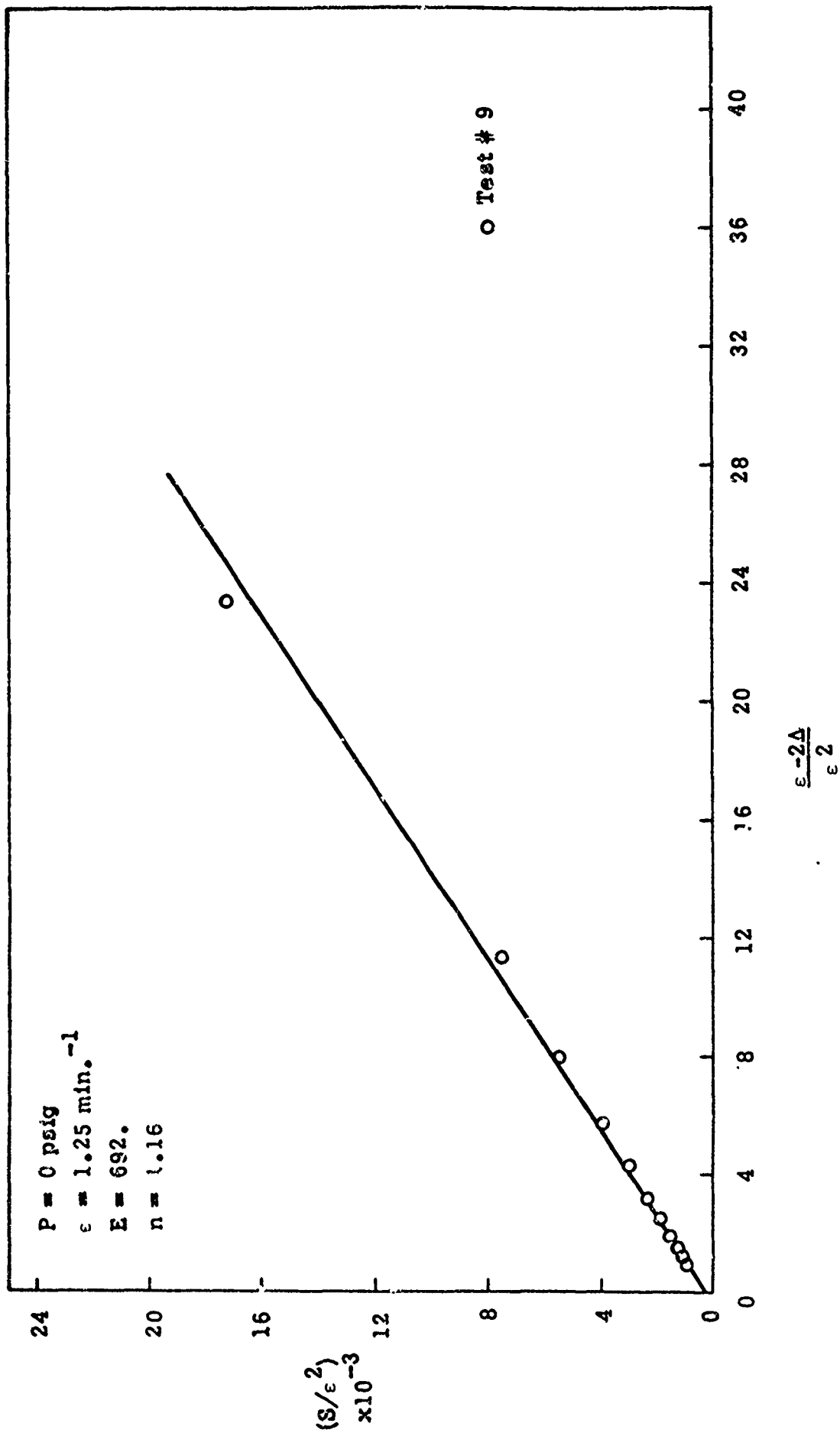


Figure 55. Fracture--controlled Simple Tensile Behavior of Aerojet CTPB Propellant

TABLE III

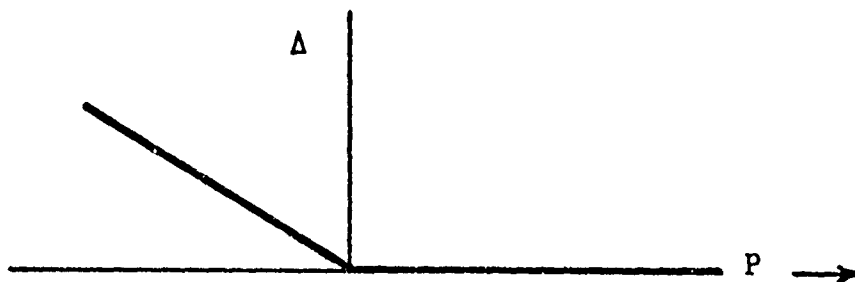
Parameter Evaluations from Tests at 77°F and 0 psig

$\dot{\epsilon}$, min^{-1}	0.0125	0.05	0.25	0.50	1.25
E, psi	385	400	567	555	692
n	1.04	2.00	1.41	1.44	1.16

Note that E increases monotonically with increasing strain rate. This trend represents the effect of viscoelasticity which we have left out of the theory. One should not read too much significance into the scatter of n because n is determined from the intercept of a line in such a way that a slight change of slope produces a large change in n. This sensitivity arises because the plot involves the large numbers (S/ϵ^2) . This scatter will be markedly reduced when the whole program is put on the computer. In this initial cut at the theory, we reduced all the calculations to an approximate form which enabled us to make log-log or linear plots.

Superimposed Hydrostatic Pressure Tests

Now we consider the case where $P > 0$. Looking at Equation (56) we note that, when $P > 3S$ the numerator of Equation (56) becomes negative, while Δ remains zero or positive. This reflects the bi-nonlinear aspects of propellant behavior, first clearly set forth by Dong, Herrmann, Pister, and Taylor (43). Putting it another way, if the filler particles were not present, the rubber would contract under pressure and Δ would be negative. But, because both the rubber and filler particles are incompressible the hydrostatic behavior of propellant is discontinuous, and a plot of Δ vs P looks like the following sketch.



Thus Equation (56) must be replaced by the statement $\Delta = 0$, when $P > S/3$. When we do this, we find the following relation:

$$\frac{\frac{S}{\epsilon^2}}{1 - \left(\frac{5}{4}\right)^{\frac{1}{1-m}} \left(\frac{\epsilon^2}{2M}\right)^{\frac{m}{1-m}}} = E \frac{n}{4} + E \left(\frac{\epsilon - \Delta/3}{\epsilon^2} \right) \quad (61)$$

NWC TP 5684

We took all the data at 50 psig and 0.5 min^{-1} strain rate (Test #'s 13, 14, 15, 16) and used the M and m determined from the data at 0 psig and made the straight line correlation suggested by (61). The result is shown in Figure 56. The agreement is fantastic. We get the same straight line as determined at zero pressure. We get the same $E = 555 \text{ psi}$, and the same $n = 1.44$.

Life is not so beautiful, however, when we go to higher pressure. At 100 psig, the linear correlation is shown in Figure 57. Again the straight line is excellent, and the modulus ($E = 550 \text{ psi}$) is in excellent agreement, but n shoots up to 5.08. At 200 psig (Figure 58), we again get a good straight line with $E = 600 \text{ psi}$ and $n = 5.33$. Part of the scatter in n is due to the fact, already alluded to, that n is determined as an intercept which is extremely sensitive to the slope of the line. But we believe that there is more significance to what happens at higher pressures; namely, there must be some extra pressure dependence of the shear modulus which we have not included in the theory. Nevertheless, we have an excellent theory for tests up to 50 psig.

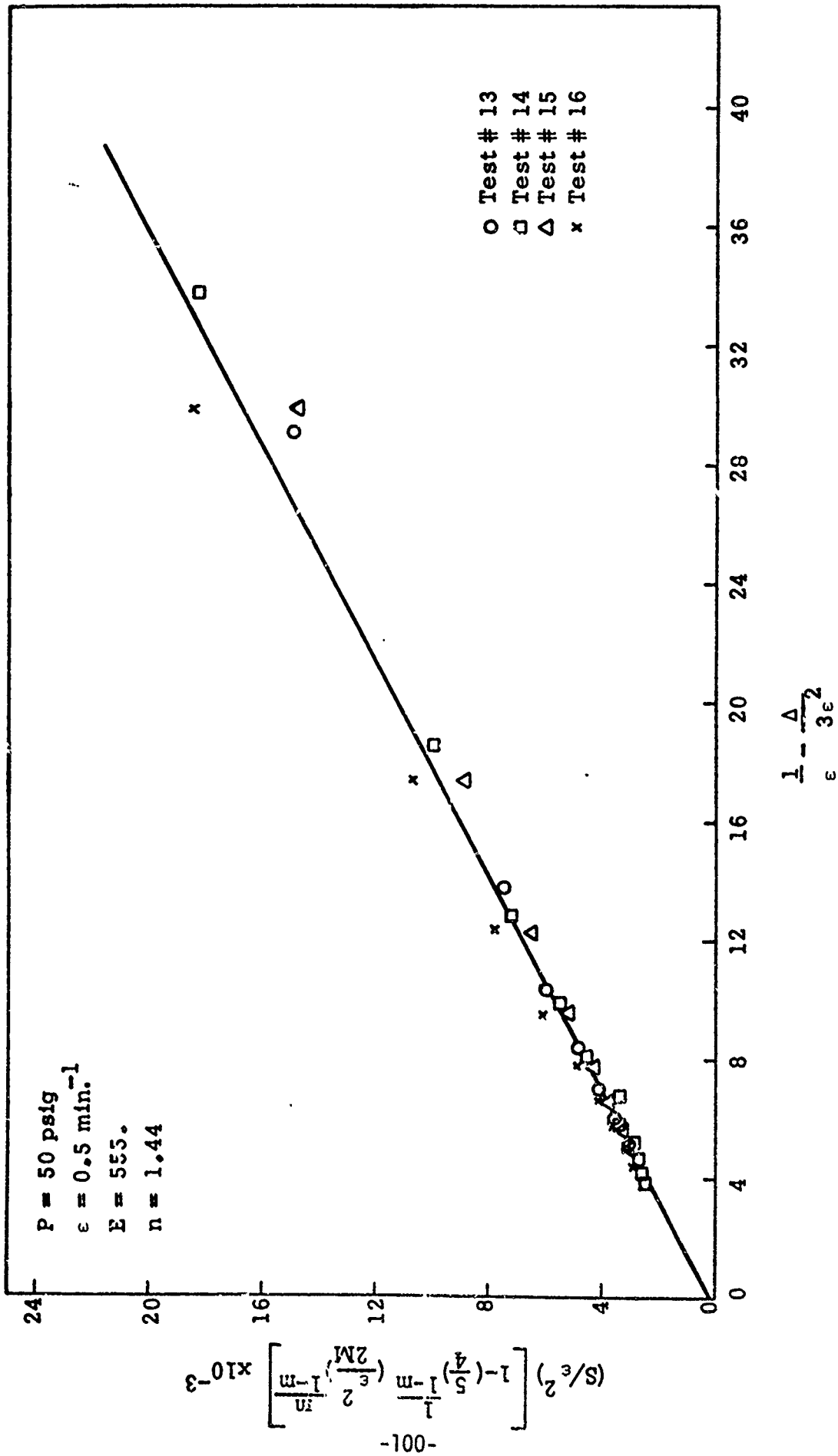


Figure 56. Fracture-controlled Dilatation of Aerojet CTPB Propellant Under Superimposed Hydrostatic Pressure

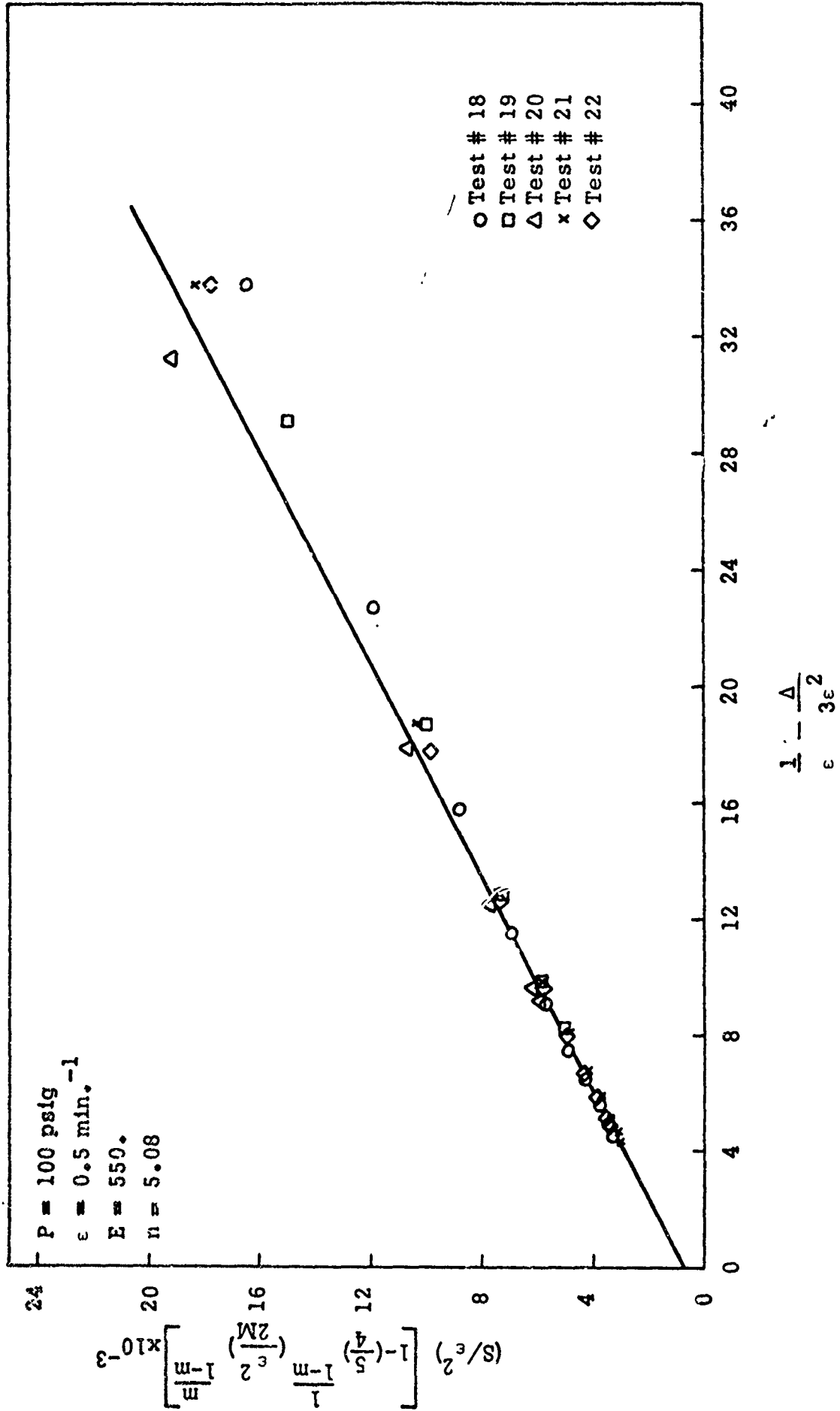


Figure 57. Fracture-controlled Dilatation of Aerojet CTPB Propellant Under Superimposed Hydrostatic Pressure.

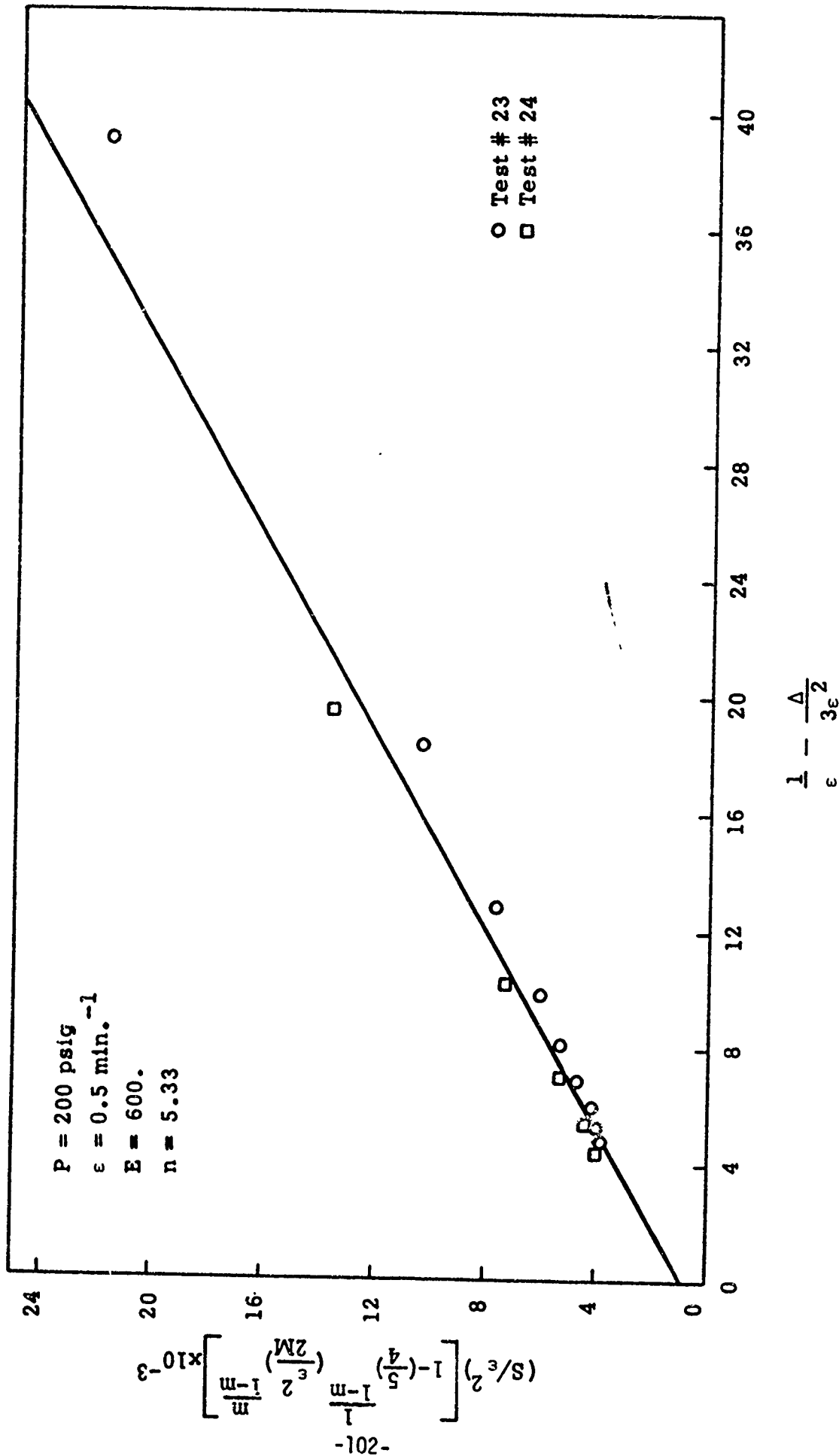


Figure 58. Fracture-controlled Dilatation of Aerojet CTPB Propellant Under Superimposed Hydrostatic Pressure.

MODIFICATION OF THE THEORY

As shown above the previous theory provided excellent correlations with uniaxial test data for pressures up to 50 psig. The purpose of this effort was to extend the correlation up to 500 psig.

In 1966, Tobolsky and Shen (44) suggested that the strain energy function for NR be modified by the factor J^α to explain the dependence of the force-pressure coefficient upon strain. Following this idea, which has been used successfully by Sharda, we write the strain energy factor in the form:

$$W = \frac{2G}{n} e J^\alpha \left[\Sigma \frac{\lambda_\alpha^n - 1}{n} + \frac{J^{-\beta} - 1}{\beta} \right] \quad (62)$$

where α is a constant

For pressures above 600 psig the dilatation is essentially suppressed; which gives:

$$J^\alpha = 1, P > 600 \text{ psig} \quad (63)$$

Under these conditions Equation (62) reduces to Equation (37). Hence the parameter characterization results given in Tables II and III remain unchanged.

Following the procedure outlined in the preceding section, and omitting unnecessary algebraic details, we arrive at the following expression for simple tension under superimposed hydrostatic pressure, after expanding to second order:

$$\gamma = \frac{2}{-1 + \frac{3}{2} \frac{\epsilon}{\Delta} - \frac{3\epsilon^2}{4\Delta} \left(\frac{n}{2} + 3\alpha \right)} \quad (64)$$

$$\left[\frac{3\epsilon}{2\Delta} - 1 - \frac{3\epsilon^2}{4\Delta} \left(\frac{n}{2} + 3\alpha \right) \right] \frac{1+m}{2m} = \frac{M}{10} 2 \frac{1+m}{2m} \left[\frac{3}{\Delta} - \frac{1}{\epsilon} - \frac{3\epsilon}{2\Delta} \left(\frac{n}{2} + 3\alpha \right) \right] \quad (65)$$

Figure 59 shows a plot of the zero pressure data, from which we find:

$$m = 0.60 \quad (66)$$

$$M = .074 \quad (67)$$

$$\frac{n}{2} + 3\alpha = 2.0 \quad (68)$$

The value of n previously determined from the 200 psi data was 5.33. Therefore we calculate that:

$$\alpha = -0.22 \quad (69)$$

which is in remarkably good agreement with the value determined by Sharda (45, 46) and by Tobolsky and Shen (44), namely $p = -0.20$.

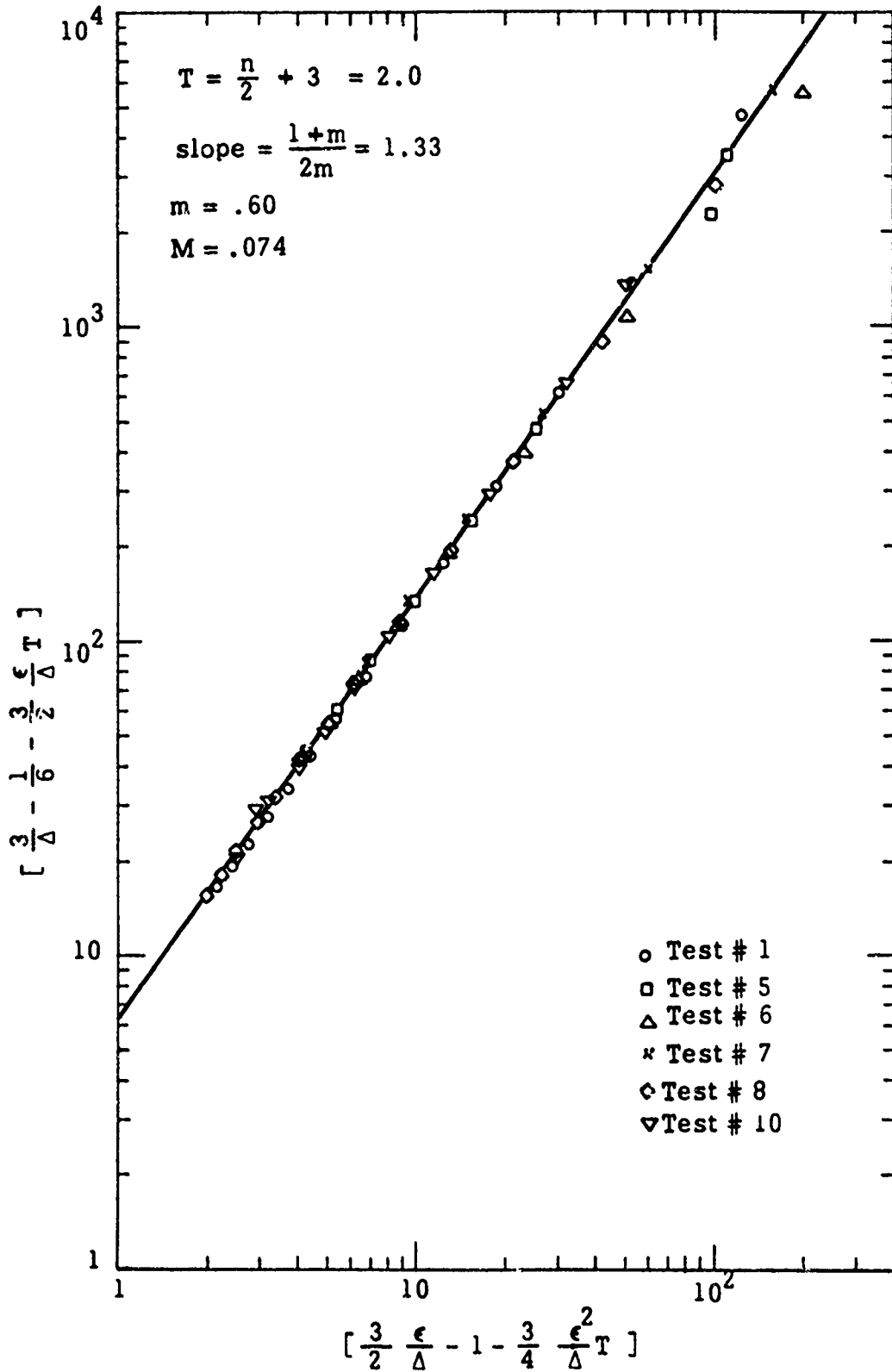


Figure 59. Fracture-Controlled Dilatation of Aerojet GTPB Propellant.

REFERENCES

1. Irwin, G. R., "Linear Fracture Mechanics in Relation to Viscoelastic Materials," Bulletin of the 6th Meeting of the ICRPG Mechanical Behavior Working Group, p. 353 (October 1967).
2. Griffith, A. A., Phil. Trans. Roy. Soc. (London), Ser. A, 221, 163 (1920-21).
3. Williams, M. L., "Initiation and Growth of Viscoelastic Fracture," International Journal of Fracture Mechanics, Vol. 1, No. 4, Dec. 1965.
4. Layton, L. H., and Bennett, S. J., "A Fracture Mechanics Approach to Surveillance," Bulletin of the 1st Meeting of JANNAF Mechanical Working Group, (November 1969).
5. Bennett, S. J., "The Use of Energy Balance in Rocket Motor Grain Integrity Studies," Bulletin of the 1st Meeting of JANNAF Mechanical Working Group, (November 1969).
6. Fulbright, J. L., and Miller, W. H., "Failure Analysis of Solid Propellant Grains Based on Dissected Motor Properties," Bulletin of the 6th Meeting of the ICRPG Mechanical Behavior Working Group, (October 1967).
7. Bills, K. W., Jr., Peterson, F. E., and Steele, R. D., "Study of Cumulative Damage Techniques for the Prediction of Motor Failure," Aerojet-General Corporation Report No. 4158-81F (Contract No. NOW 66-0545-c), (July 1967).
8. Bills, K. W., Jr., Peterson, F. E., Steele, R. D., and Sampson, R. C., "Development of Criteria for Solid Propellant Screening and Preliminary Engineering Design," Aerojet Report 1 59-81F (Contract No. N00017-67-C-2415), (December 1968).
9. Bills, K. W., Jr., et. al, "Solid Propellant Cumulative Damage Program," Final Report No. AFRPL-TR-68-131, Contract No. FO4611-67-C-0102, (October 1968).
10. Bills, K. W., Jr., Campbell, D. M., Steele, R. D., and McConnell, J. D., "Applications of Cumulative Damage in the Preparation of Parametric Design Curves and the Prediction of Grain Failures on Pressurization," Aerojet Solid Propulsion Company Report No. 1341-26F, Contract No. N000-17-69-C-4423 (July 1970).

REFERENCES (CONT.)

11. Bills, K. W., Jr., Campbell, D. M., Sampson, R. C., and Steele, R. D., "Failures in Grains Exposed to Rapid Changes of Environmental Temperatures," Aerojet Report 1236-81F, Contract N00017-68-C-4415 (September 1969).
12. Farris, R. J., "Applications of Non-Linear Viscoelasticity and Cumulative Damage," Report No. 1565-26F (May 1970).
13. Farris, R. J., "Development of a Solid Rocket Propellant Nonlinear Viscoelastic Constitutive Theory," AFRPL-TR-73-50 Final Report, Aerojet Solid Propulsion Company (June 1973).
14. Bauschinger.
15. Lindsey, G. H., "Studies Pertaining to Solid Propellant Fracture," Naval Post Graduate School Report NPS-57L172011A (January 31, 1972).
16. Graham, P. H., Robinson, C. N., Henderson, C. B., "Analysis of Dilatational Failure of Heterogeneous Materials by Reaction Rate Theory," International Journal of Fracture Mechanics, 5, No. 1, p. 57, (1969).
17. Knauss, W. G., "Delayed Fracture in Viscoelastic-Plastic Solids," Int. J. Solids Structures, 6, 995 (1970).
18. Bueche, F., and Dudek, T. J., "Tensile Strength of Amorphous Gum Rubbers," Rubber Chem. and Tech., 36, p. 1 (1963).
19. Dudek, T. J., and Bueche, F., "Tensile Strength of Gum and Reinforced EPR and SBR Vulcanizates," Rubber Chem. and Tech., 37, 818 (1964).
20. Dudek, T. J., and Bueche, F., J. Appl. Polymer Sci., 8, 555 (1964).
21. Francis, F. C., and Carlton, C. H., "Some Aspects of Composite Propellant Nonlinear Behavior in Structural Applications," ICRPG/AIAA 3rd Solid Propulsion Conference, AIAA Paper No. 68-519 (June 1968).
22. Adicoff, A., and Lepie, A. H., "Effect of Tensile Strain on the Use of the WLF Equation," J. App. Poly. Sci., 14, p. 953 (1970).
23. Seth, B. R., Paper Published in International Symposium on Second Order Effects on Elasticity and Plasticity Technion, Haifa, Israel, April 1962.

REFERENCES (CONT.)

24. Andrews, E. H., "Reinforcement of Rubber by Fillers," *Rubber Chem. and Tech.*, 36, 325-36 (1963).
25. Bills, K. W., Jr., and Campbell, D. M. Aerojet Report No. 1341-26-Q-1, Pages 22 and 23, (July 1969).
26. Bills, K. W., Jr., "Study of Cumulative Damage Techniques for the Prediction of Motor Failure," Report No. 4158-81-Q-3, Table 1 (March 1967).
27. Bueche, F., and Halpin, J. C., *J. Appl. Phys.*, 35, (1964).
28. Schapery, R. A., "A Theory of Crack Growth in Viscoelastic Media," Texas A&M University Report No. MM 2764-73-1 (March 1973).
29. Schapery, R. A., "A Nonlinear Constitutive Theory for Particulate Composites Based on Viscoelastic Fracture Mechanics," Presented at the 12th Meeting of the JANNAF Structures and Mechanical Behavior Working Group (February 1974).
30. Leon, G. S., and McClintock, F. A., in Wiegand, J. H. (ed), *Study of Mechanical Properties of Solid Rocket Propellants*, Report No. 0411-10F, Contract AF 33(600)-40314, S. A., No. 1, Appendix G, Aerojet-General Corporation, March 1962.
31. Andrews, E. H., *Proc. Phys. Soc.*, 77,483 (1961).
32. Andrews, E. H., *Fracture in Polymers*, American Elsevier, New York (1968).
33. Bills, K. W., Jr., and Svob, G. J., "Establishing Mechanical Properties Criteria," *Bulletin of the 4th Meeting of the ICRPG Working Group on Mechanical Behavior*, p. 269, (October 1965).
34. Landel, R. F., and Fedors, R. F., "A Molecular Theory of Elastomer Deformation and Rupture," *Mechanical Behavior of Materials*, III, p. 496 (1972).
35. Fedors, R. F., and Landel, R. F., "A Relationship Between Network Chain Concentration and Time Dependence of Rupture for SBR Vulcanizates," *JPL Space Programs Summary 37-58*, Vol. III, pp. 180-186.

REFERENCES (CONT.)

36. Schapery, R. A., Solid Propellant Structural Test Vehicle Program, AFRPL-TR-72-29, p. 177 to 182 (April 1972).
37. Farris, R. J., "The Character of the Stress-Strain Function for Highly Filled Elastomers," Trans. Soc. of Rheol., 12, 303-314 (1968).
38. Farris, R. J., "The Influence of Vacuole Formation on the Response and Failure of Filled Elastomers," Trans. Soc. of Rheol., 12, 315-334 (1968).
39. Farris, R. J., "The Stress-Strain Behavior of Mechanically Degradable Polymers," Polymer Networks: Structural and Mechanical Properties, Edited by A. J. Chomppf and S. Newman, Plenum Pub. Co., N. Y., (1971).
40. Lindsey, G. H., and Murch, S. A., "An Isotropic Theory of Dewettable Solids," Trans. of Rheology (In Press.).
41. Pipkin and Dag.
42. Warren, N., Compressibilities of Porous Media, J. Geophys. Res. 78, 352 (1973).
43. Dong, S., Herrmann, L., Pister, K., and Taylor, R., Final Report to Aerojet-General Corporation, out of the Department of Civil Engineering, UCB, "Studies Relating to Structural Analysis of Solid Propellants," (February 1962).
44. Tobolsky, and Shen, J.A.P., 37, (1953 or 1966?).
45. Sharda, S. C., Thesis, Ex-Chemical Engineering Division, Calif. Inst. of Tech. (Year ?).
46. Blatz, P. J., Sharda, S. C., and Tschoegi, N. W., "A Constitutive Equation for Rubber Like Materials Placed on n-Measure of Strain," Paper submitted to Trans. of Rheology (In Press).

NWC TP 5684

APPENDIX A
ON VISCOELASTIC FRACTURE OF
SOLID PROPELLANT

Introduction

In this report we present a rationalization of the observed fact that, in propellants, stress-at-break seems to correlate with the square root of the relaxation modulus evaluated at time-to-break. The basis for this rationalization is the ablating-spherical-hole model of Max Williams, which has never been correctly analyzed for reasons which we shall present below. The beauty of the model however lies in the observation that the spherical-flaw model gives basically the same fracture prediction as does the penny-shaped-flaw model, the two differing only in a shape factor. The advantage of the model is that the algebra associated with its development is relatively simple. The basis for using it, or the justification, is obtained if one imagines that the applied stress (to a simple tensile bar) is concentrated around a void in some fashion that makes the void grow like a bubble expanding. This stress concentration effect means that our final results on the spherical-flaw must be related back to the observed data on a tensile bar simply by multiplying in a stress concentration factor. This is actually a somewhat crude approximation, which will be later replaced (and discussed in a subsequent progress report) by a more sophisticated randomly-flawed model which is currently under development.

Analysis

In order to set the theme for this discussion, we must understand the general theory of viscoelastic constitutive equations. In this report we restrict the discussion to linear behavior. The linear theory of viscoelasticity is conveniently represented by a Maxwell model, which is a parallel array of one rubbery spring and a distribution of Maxwell elements; each element is a series array of one Hookean spring and one Newtonian dashpot; the Maxwell elements are distributed in terms of their relaxation times. The rules for the model are: stress adds in parallel and is constant in series; strain adds in series, and is constant in parallel. With this in mind, we have the following relations:

$$\underline{\underline{t}} = \underline{\underline{t}}^R + \sum \underline{\underline{t}}^i \quad (\text{A-1})$$

$$\underline{\underline{t}}^R = 2G_R \underline{\underline{e}} + \left(K_R - \frac{2}{3} G_R \right) \delta \underline{\underline{I}} \quad (\text{A-2})$$

$$\underline{\underline{t}}^i = 2G_i \underline{\underline{e}}^{iS} + \left(K_i - \frac{2}{3} G_i \right) \delta^{iS} \underline{\underline{I}} \quad (\text{A-3})$$

$$\underline{\underline{t}}^i = 2G_i \tau_i \underline{\underline{e}}^{iD} + \left(K_i \tau_i - \frac{2}{3} G_i \tau_i \right) \delta^{iD} \underline{\underline{I}} \quad (\text{A-4})$$

$$\underline{\underline{e}}^{iS} + \underline{\underline{e}}^{iD} = \underline{\underline{e}} \quad (\text{A-5})$$

where

\underline{t} is the total stress tensor

\underline{t}^R is the stress tensor in the rubbery spring

\underline{t}^i is the stress tensor in any Maxwell element

\underline{e} is the applied strain tensor

\underline{I} is the idem-tensor

G and K are the elastic moduli

τ_i are the shear relaxation times

τ_{B1} are the bulk relaxation times

\underline{e}^{1S} is the strain tensor in the spring of a Maxwell element

\underline{e}^{1D} is the strain tensor in the dashpot of a Maxwell element

What we do now is to separate the above expressions into traces and deviators.

We have:

$$\underline{t}^R = \underline{s}^R - p^R \underline{I} \quad (\text{A-6})$$

$$\underline{t}^i = \underline{s}^i - p^i \underline{I} \quad (\text{A-7})$$

$$\underline{e} = \underline{\epsilon} + \frac{\vartheta}{3} \underline{I} \quad (\text{A-8})$$

$$\underline{e}^{1S} = \underline{\epsilon}^{1S} + \frac{\vartheta^{1S}}{3} \underline{I} \quad (\text{A-9})$$

$$\underline{e}^{1D} = \underline{\epsilon}^{1D} + \frac{\vartheta^{1D}}{3} \underline{I} \quad (\text{A-10})$$

where

\underline{s} is the stress deviator

$\underline{\epsilon}$ is the strain deviator

From (A-2), we have:

$$p^R = -K_R \vartheta \quad (A-11)$$

$$\underline{s}^R = 2G_R \underline{\epsilon} \quad (A-12)$$

From (A-3), we have:

$$p^I = -K_1 \vartheta^{IS} \quad (A-13)$$

$$\underline{s}^I = 2G_1 \underline{\epsilon}^{IS} \quad (A-14)$$

From (A-4), we have:

$$p^I = -K_1 \tau_{B1} \dot{\vartheta}^{ID} \quad (A-15)$$

$$\underline{s}^I = 2G_1 \dot{\underline{\epsilon}}^{ID} \quad (A-16)$$

From (A-5), we have:

$$\vartheta^{IS} + \vartheta^{ID} = \vartheta \quad (A-17)$$

$$\underline{\epsilon}^{IS} + \underline{\epsilon}^{ID} = \underline{\epsilon} \quad (A-18)$$

When Equations (A-13), (A-15) and (A-17) are combined, we obtain:

$$\vartheta^{IS} = \int_0^t e^{-\frac{t-t'}{\tau_{B1}}} d\vartheta(t') \quad (A-19)$$

$$\dot{\vartheta}^{ID} = \frac{\vartheta^{IS}}{\tau_{B1}} \quad (A-20)$$

$$p^I = -K_1 \vartheta^{IS} \quad (A-21)$$

Likewise, when Equations (A-14), (A-16), and (A-18) are combined, we obtain:

$$\underline{\epsilon}^{iS} = \int_0^t e^{-\frac{t-t'}{\tau_1}} d \underline{\epsilon} (t') \quad (A-22)$$

$$\dot{\underline{\epsilon}}^{iD} = \frac{\underline{\epsilon}^{iS}}{\tau_1} \quad (A-23)$$

$$\underline{s}^i = 2G_1 \underline{\epsilon}^{iS} \quad (A-24)$$

When we add everything up, we have:

$$\underline{t} = 2 \int_0^t (G_R + \Sigma G_1 e^{-\frac{t-t'}{\tau_1}}) d \underline{\epsilon} (t') + \int_0^t (K_R + \Sigma K_1 e^{-\frac{t-t'}{\tau_{B1}}}) d \vartheta (t') \quad (A-25)$$

In order to simplify the ensuing analysis in a nonessential fashion, we shall assume that all of the relaxation processes are shear processes, and that the bulk processes are purely elastic. This implies that the τ_{B1} are all zero. Then Equations (A-19, A-20, A-21 and A-25) become:

$$\vartheta^{iS} = \vartheta \quad (A-26)$$

$$\dot{\vartheta}^{iS} = 0 \quad (A-27)$$

$$p^i = -K_1 \vartheta \quad (A-28)$$

$$\underline{t} = 2 \int_0^t (G_R + \Sigma G_1 e^{-\frac{t-t'}{\tau_1}}) d \underline{\epsilon} (t') + \int_0^t K_G \vartheta \quad (A-29)$$

where

$$K_G = K_R + \Sigma K_1 \quad (A-30)$$

The stored energy in the model is the sum of the strain energies in all springs. In any one spring, the strain energy is given by:

$$W^i = \frac{1}{2} \underline{t}^i : \underline{\epsilon}^{iS} \quad (A-31)$$

$$= \frac{1}{2} (\underline{s}^i - p^i \underline{I}) : (\underline{\epsilon}^{iS} - \frac{\vartheta^{iS}}{3} \underline{I})$$

$$= \frac{1}{2} (\underline{s}^i : \underline{\epsilon}^{iS} - p^i \vartheta^{iS}) \quad (A-32)$$

$$= G_1 \underline{\epsilon}^{iS} : \underline{\epsilon}^{iS} + \frac{K_1}{2} (\vartheta^{iS})^2 \quad (A-33)$$

The stored energy is thus:

$$W = G_R \underline{\epsilon} : \underline{\epsilon} + \sum G_i \underline{\epsilon}^{iS} : \underline{\epsilon}^{iS} + \frac{K_G}{2} \vartheta^2 \quad (A-34)$$

Likewise, the dissipation rate is given by:

$$\begin{aligned} \mathcal{D} &= \sum \underline{\dot{\epsilon}}^i : \dot{\epsilon}^{iD} = \sum (\underline{\dot{\epsilon}}^i - p^i \underline{\dot{I}}) : \left(\frac{\underline{\dot{\epsilon}}^{iS}}{\tau_i} \right) = \sum \frac{\underline{\dot{\epsilon}}^i : \underline{\dot{\epsilon}}^{iS}}{\tau_i} \\ &= 2 \sum \frac{G_i}{\tau_i} \underline{\dot{\epsilon}}^{iS} : \underline{\dot{\epsilon}}^{iS} \end{aligned} \quad (A-35)$$

The spherical flaw model deals with an ablating hole of radius a in a sphere of radius b , subjected to isotropic tension at $r = b$. The displacement must have the form:

$$u = Ar + \frac{B}{r^2} \quad (A-36)$$

whereupon $e_\theta = A + \frac{B}{r^3} \quad (A-37)$

$$e_r = A - \frac{2B}{r^3} \quad (A-38)$$

$$\vartheta = 3A \quad (A-39)$$

$$\epsilon_\theta = \frac{B}{r^3} \quad (A-40)$$

$$\epsilon_r = -\frac{2B}{r^3} \quad (A-41)$$

$$\sigma_r = -\frac{4}{r^3} \int_0^t (G_R + \sum G_i e^{-\frac{t-t'}{\tau_i}}) dB(t') + 3K_G A \quad (A-42)$$

$$\sigma_\theta = \frac{2}{r^3} \int_0^t (G_R + \sum G_i e^{-\frac{t-t'}{\tau_i}}) dB(t') + 3K_G A \quad (A-43)$$

The radial stress is zero at $r = a$, giving:

$$3K_G A = \frac{4}{a^3} \int_0^t (G_R + \sum G_i e^{-\frac{t-t'}{\tau_i}}) dB(t') \quad (A-44)$$

so that:

$$u = \frac{B}{r^2} + \frac{4r}{3K_G a^3} \int_0^t (G_R + \sum G_i e^{-\frac{t-t'}{\tau_i}}) dB(t') \quad (A-45)$$

$$\sigma_r = 4\left(\frac{1}{a^3} - \frac{1}{r^3}\right) \int_0^t (G_R + \Sigma G_i e^{-\frac{t-t'}{\tau_i}}) dB(t') \quad (A-46)$$

$$\sigma_\theta = \left(\frac{4}{a^3} + \frac{2}{r^3}\right) \int_0^t (G_R + \Sigma G_i e^{-\frac{t-t'}{\tau_i}}) dB(t') \quad (A-47)$$

At $r = b$, the radial stress is S , giving:

$$S = 4\left(\frac{1}{a^3} - \frac{1}{b^3}\right) \int_0^t (G_R + \Sigma G_i e^{-\frac{t-t'}{\tau_i}}) dB(t') \quad (A-48)$$

The power input to the sphere is given by:

$$\mathcal{P} = S \cdot 4\pi b^2 \cdot \dot{u}_b \quad (A-49)$$

where

$$\begin{aligned} \dot{u}_b = & \frac{\dot{B}}{b^2} - \frac{4ba}{K_G a^4} \int_0^t (G_R + \Sigma G_i e^{-\frac{t-t'}{\tau_i}}) dB(t') \\ & + \frac{4b}{3K_G a^3} G_G \dot{B} - \frac{4b}{3K_G a^3} \int_0^t dB(t') \Sigma \frac{G_i}{\tau_i} e^{-\frac{t-t'}{\tau_i}} \end{aligned} \quad (A-50)$$

Let us define:

$$\varphi_i \equiv \int_0^t e^{-\frac{t-t'}{\tau_i}} dB(t') \quad (A-51)$$

whereupon:

$$u = \frac{B}{r^2} + \frac{4r}{3K_G a^3} (G_R B + \Sigma G_i \varphi_i) \quad (A-52)$$

$$S = 4\left(\frac{1}{a^3} - \frac{1}{b^3}\right) (G_R B + \Sigma G_i \varphi_i) \quad (A-53)$$

$$\begin{aligned} \mathcal{P} = & 16\pi b^2 \left(\frac{1}{a^3} - \frac{1}{b^3}\right) (G_R B + \Sigma G_i \varphi_i) \times \\ & \left[\frac{\dot{B}}{b^2} - \frac{4ba}{K_G a^4} (G_R B + \Sigma G_i \varphi_i) + \frac{4b}{3K_G a^3} G_G \dot{B} - \frac{4b}{3K_G a^3} \Sigma \frac{G_i \varphi_i}{\tau_i} \right] \end{aligned} \quad (A-54)$$

The stored energy is given by:

$$W = \frac{6}{r} (G_R B^2 + \Sigma G_i \varphi_i^2) + \frac{8}{K_G a^6} (G_R B + \Sigma G_i \varphi_i)^2 \quad (A-55)$$

The total strain energy in the sphere is given by:

$$U_1 = \int_a^b W 4\pi r^2 dr = \frac{32\pi}{3} \left(\frac{b^3}{a^6} - \frac{1}{a^3} \right) \frac{(G_R B + \Sigma G_i \varphi_i)^2}{K_G} \quad (A-56)$$

$$+ 8\pi \left(\frac{1}{a^3} - \frac{1}{b^3} \right) (G_R B^2 + \Sigma G_i \varphi_i^2)$$

The dissipation rate is given by:

$$\mathcal{D} = \frac{12}{r^6} \Sigma \frac{G_i \varphi_i^2}{\tau_i} \quad (A-57)$$

And the total dissipation rate is given by:

$$\dot{U}_2 = 16\pi \left(\frac{1}{a^3} - \frac{1}{b^3} \right) \Sigma \frac{G_i \varphi_i^2}{\tau_i} \quad (A-58)$$

The total surface energy is given by:

$$U_3 = \Gamma 4\pi a^2 \quad (A-59)$$

And the Griffith criterion demands this:

$$\mathcal{P} = \dot{U}_1 + \dot{U}_2 + \dot{U}_3 \quad (A-60)$$

which, after simplification, leads to:

$$0 = \dot{a} \left[\frac{\Gamma a^5}{3} - (G_R B^2 + \Sigma G_i \varphi_i^2) - \frac{4}{3K_G} (G_R B + \Sigma G_i \varphi_i)^2 \right] \quad (A-61)$$

The third term in the brackets of (A-61) can be neglected, whereupon (A-61) becomes:

$$0 = \dot{a} \left[\frac{\Gamma a^5}{3} - (G_R B^2 + \Sigma G_i \varphi_i^2) \right] \quad (A-62)$$

Equations (A-53) and (A-62) jointly relate (a, B, and Σ). Equation (A-62) explicitly states that the void does not grow ($\dot{a} = 0$) until $\left[\frac{\Gamma a^5}{3} = G_R B^2 + \Sigma G_i \varphi_i^2 \right]$.

This defines the criticality condition at which fracture starts.

We are interested in relating S to a and also determining the time-to-break, when $(a = b)$. B can be eliminated from (A-53) by Laplace transformation. However, there is an easier way to carry out the analysis without getting involved in the solution of a nonlinear integral equation. We assume that B increases exponentially with terms of the form:

$$B = Ae^{\alpha t} \tag{A-63}$$

Then (A-53) becomes:

$$\frac{\frac{5/4}{a^3} - \frac{1}{b^3}}{\frac{1}{a^3} - \frac{1}{b^3}} = B \left(G_R + \sum G_i \frac{\alpha \tau_i}{1 + \alpha \tau_i} \right) \tag{A-64}$$

In writing (A-64), we have assumed that:

$$e^{\alpha t} \gg e^{-t/\tau_i} \tag{A-65}$$

There are two cases:

- a) if t is greater than $\tau_{i\max}$, then (A-65) is good for any α
- b) if t is smaller than $\tau_{i\min}$, then (65) is good for $\alpha t > 1$

When (A-63) is substituted into (A-62), we obtain:

$$\frac{\Gamma a^5}{3} = B^2 \left[G_R + \sum G_i \left(\frac{\alpha \tau_i}{1 + \alpha \tau_i} \right)^2 \right] \tag{A-66}$$

Elimination of B yields:

$$S = 4 \left(1 - \frac{a^3}{b^3} \right) \left(G_R + \sum G_i \frac{\alpha \tau_i}{1 + \alpha \tau_i} \right) \sqrt{\frac{\Gamma/3a}{G_R + \sum G_i \left(\frac{\alpha \tau_i}{1 + \alpha \tau_i} \right)^2}} \tag{A-67}$$

Equation (A-67) determines A as a function of a , or vice versa. For the purely elastic fracture, we have:

$$S = 4 \left(1 - \frac{a^3}{b^3} \right) \sqrt{\frac{\Gamma}{3a}} \tag{A-68}$$

so that (A-61) really determines an effective modulus:

$$G_{\text{eff}} = \frac{\left(G_R + \sum G_i \frac{\alpha \tau_i}{1 + \alpha \tau_i} \right)^2}{G_R + \sum G_i \left(\frac{\alpha \tau_i}{1 + \alpha \tau_i} \right)^2} \tag{A-69}$$

The parameter α is determined by the break-time t_b which in turn, according to the model, is determined when $a = b$. Equation (A-66) yields:

$$\frac{\Gamma b^5}{3} = A^2 e^{2\alpha t_b} \left[G_R + \Sigma G_i \left(\frac{\alpha \tau_i}{1 + \alpha \tau_i} \right)^2 \right] \quad (A-70)$$

Let us now consider each of the two limiting cases:

a) when $t > \tau_{imax}$, we take $\alpha \tau_i \ll 1$, and arrive at:

$$\frac{\Gamma b^5}{3} = A^2 (1 + 2\alpha t_b) G_R \quad (A-71)$$

$$\alpha = \frac{1}{2t_b} \left(\frac{\Gamma b^5}{3A^2 G_R} - 1 \right) \quad (A-72)$$

$$G_{eff} = G_R + \frac{\eta}{8b} \left(\frac{\Gamma b^5}{3A^2 G_R} - 1 \right) \quad (A-73)$$

where

$$\eta = \Sigma G_i \tau_i \quad (A-74)$$

b) when $t < \tau_{imin}$, we take $\alpha \tau_i \gg 1$, and arrive at:

$$\frac{\Gamma b^5}{3} = A^2 e^{2\alpha t_b} G_G \quad \text{or} \quad \alpha = \frac{1}{2t_b} \ln \left(\frac{\Gamma b^5}{3A^2 G_G} \right) \quad (A-75)$$

$$G_{eff} = G_G + \frac{1}{G_G \alpha^2} \left[\left(\Sigma \frac{G_i}{\tau_i} \right)^2 - G_G \Sigma \frac{G_i}{\tau_i^2} \right] \quad (A-76)$$

where

$$G_G = G_R + \Sigma G_i \quad (A-77)$$

For intermediate values of α or t_b , (A-69) and (A-70) can be put on the computer for an assumed distribution function G_i . A very useful representation is:

$$\frac{\sum \frac{G_1}{1 + a\tau_1}}{\sum G_1} = \frac{1}{1 + k a^n} \quad (\text{A-73})$$

where $0 < n < 1$. This is the Cole distribution function.

In summary, what we have shown is that the stress-at-break is proportional to the square-root of the effective relaxation modulus-at-break (A-68), where the effective modulus is defined by A-69), and the time-to-break is introduced through (A-70).

EFFECTS OF PROPELLANT DEWETTING

The oxidizer/binder dewetting phenomenon has a number of effects on propellant response and failure behavior. The following sub-sections describe some of the major effects; namely: (1) The effect of dewetting on propellant failure criteria; (2) the effect of superimposed pressures upon vacuole formation; and (3) the dependence of low-strain moduli upon dewetting.

1. The Effect of Dewetting on Propellant Failure Criteria

Previous studies (B-1 to B-5) at Aerojet produced a simple failure criterion for solid propellants. This criterion was developed from constant load-to-failure testing using uniaxial, strip-biaxial and poker chip tests. In its simplest form, all test data, regardless of testing mode, can be reduced to a single curve. This curve represents the time-to-failure under a constant applied stress. A typical failure curve is shown in Figure B-1. The curve was obtained using data from two different cartons of a polybutadiene propellant (using the a_T values obtained by Lockheed Propulsion Company on their STV program). As shown in Reference B-1, test data from strip-biaxial and poker chip tests fall on this failure curve.

The same curve was obtained for tests performed under superimposed hydrostatic pressures (Figure B-2). However, in this case it was necessary to shift the test data along the time axis by a time-pressure shift factor, a_p . A plot of a_p versus pressure is provided in Figure B-3. These results are typical of those obtained for many other propellant formulations.

Figure B-1. EQUIVALENT CONSTANT STRESS TO FAILURE CURVE OBTAINED FROM TWO CARTONS OF THE STV PROPELLANT

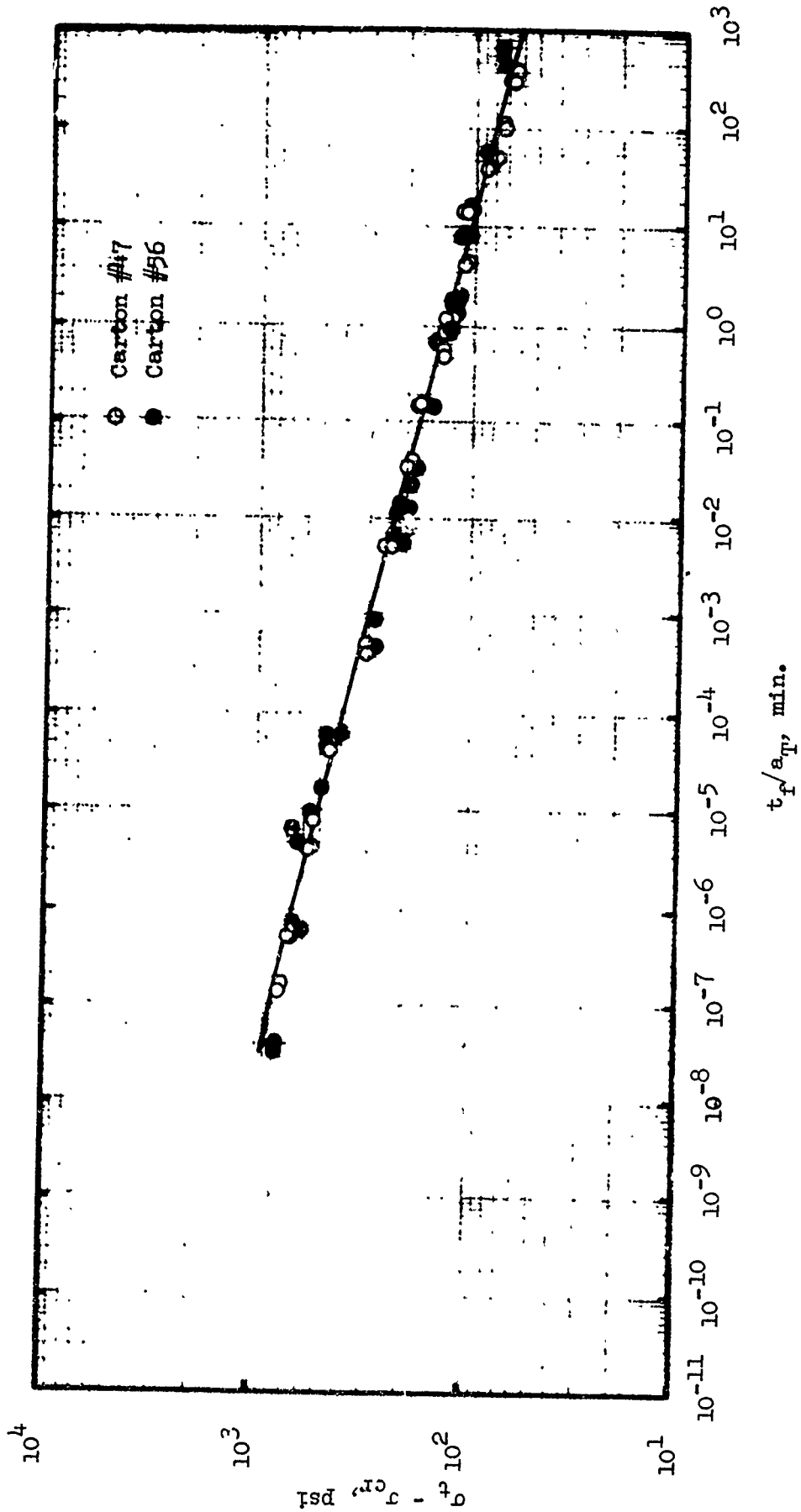


Figure B-2. EFFECT OF SUPERIMPOSED PRESSURE ON CONSTANT STRESS TO FAILURE DATA FOR THE STV PROPELLANT (PRESSURE SHIFTED TO 0 PSIG)

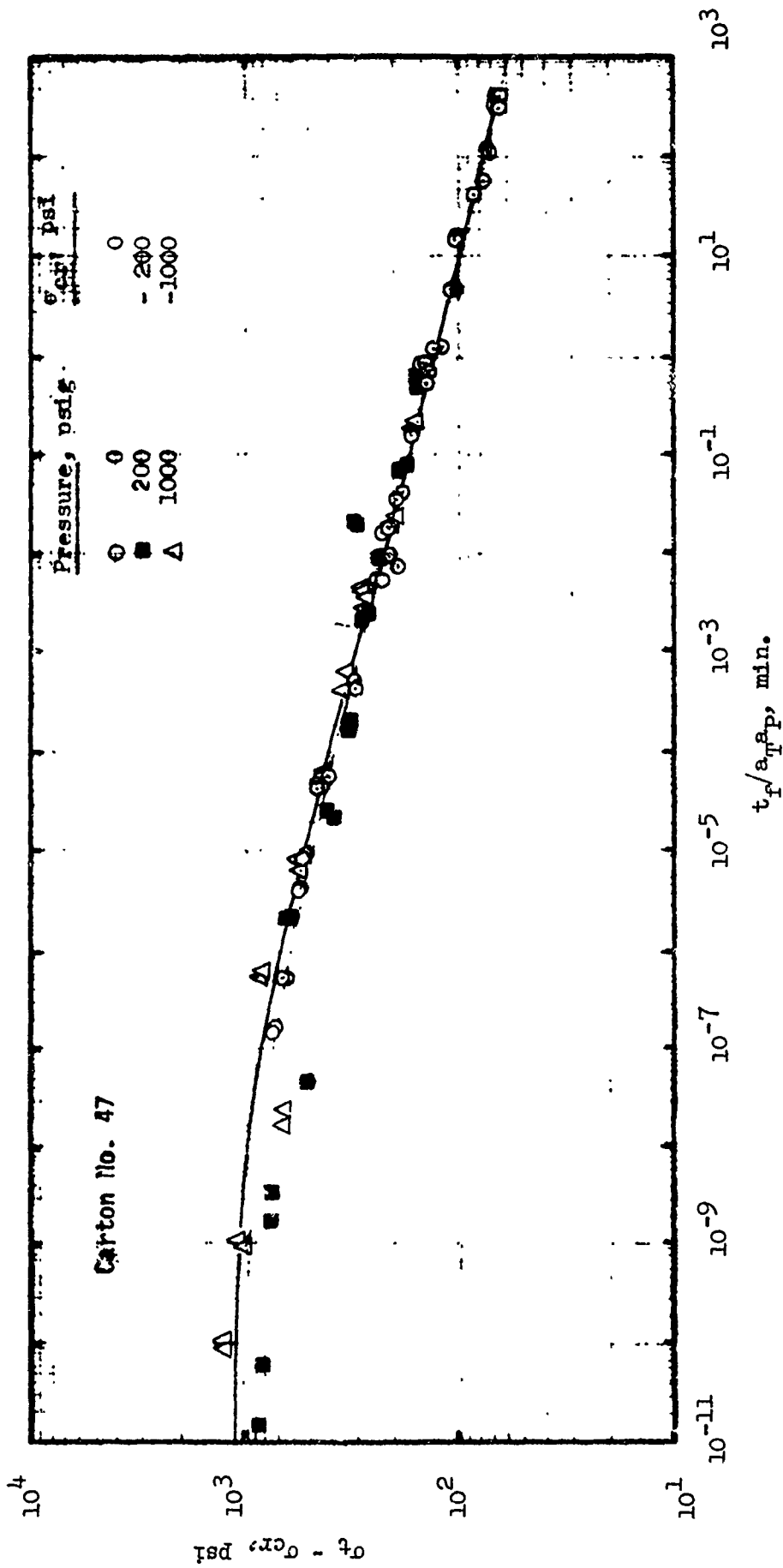
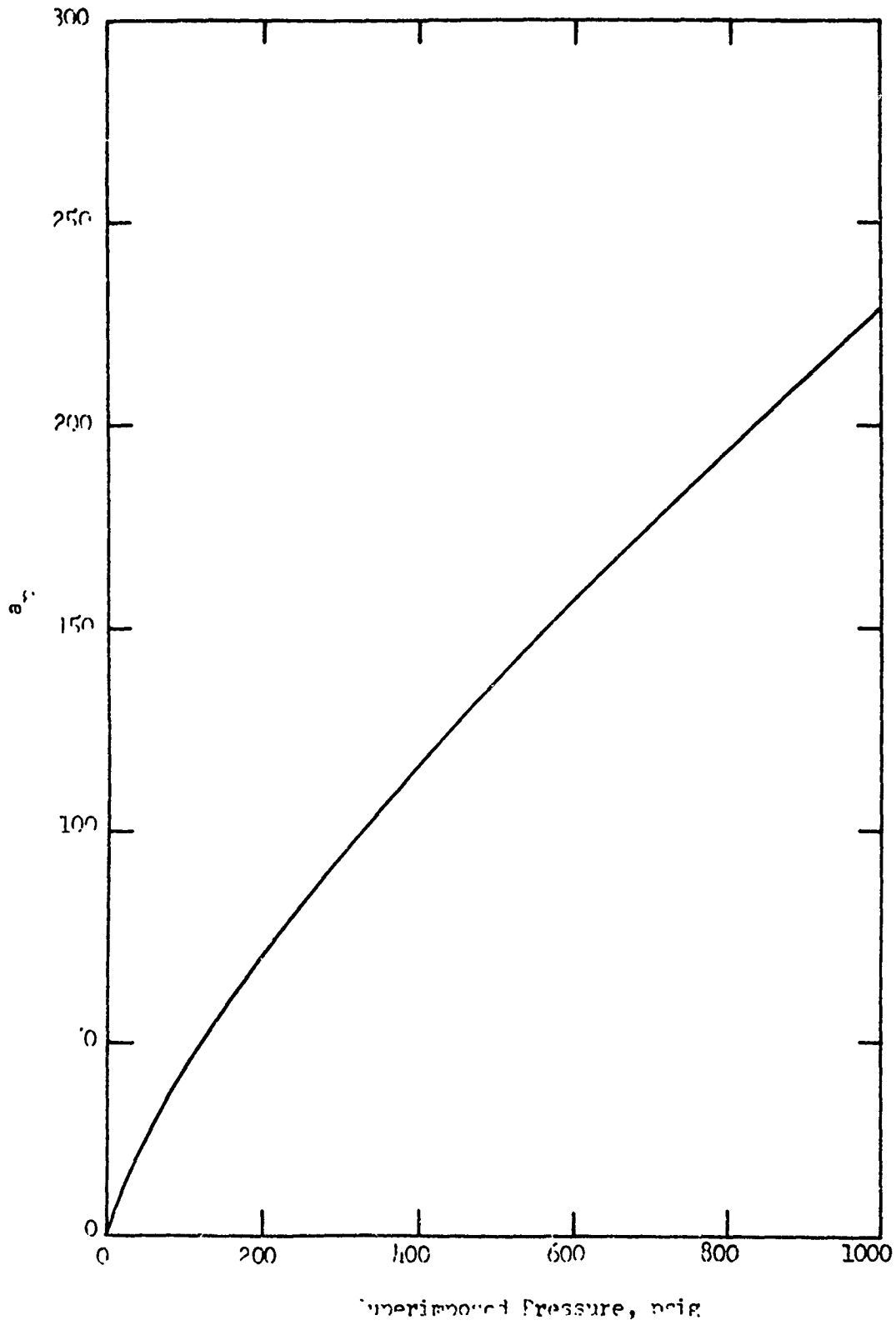


Figure B-3. TIME-PRESSURE SHIFT FACTOR FOR NEW PROPellant

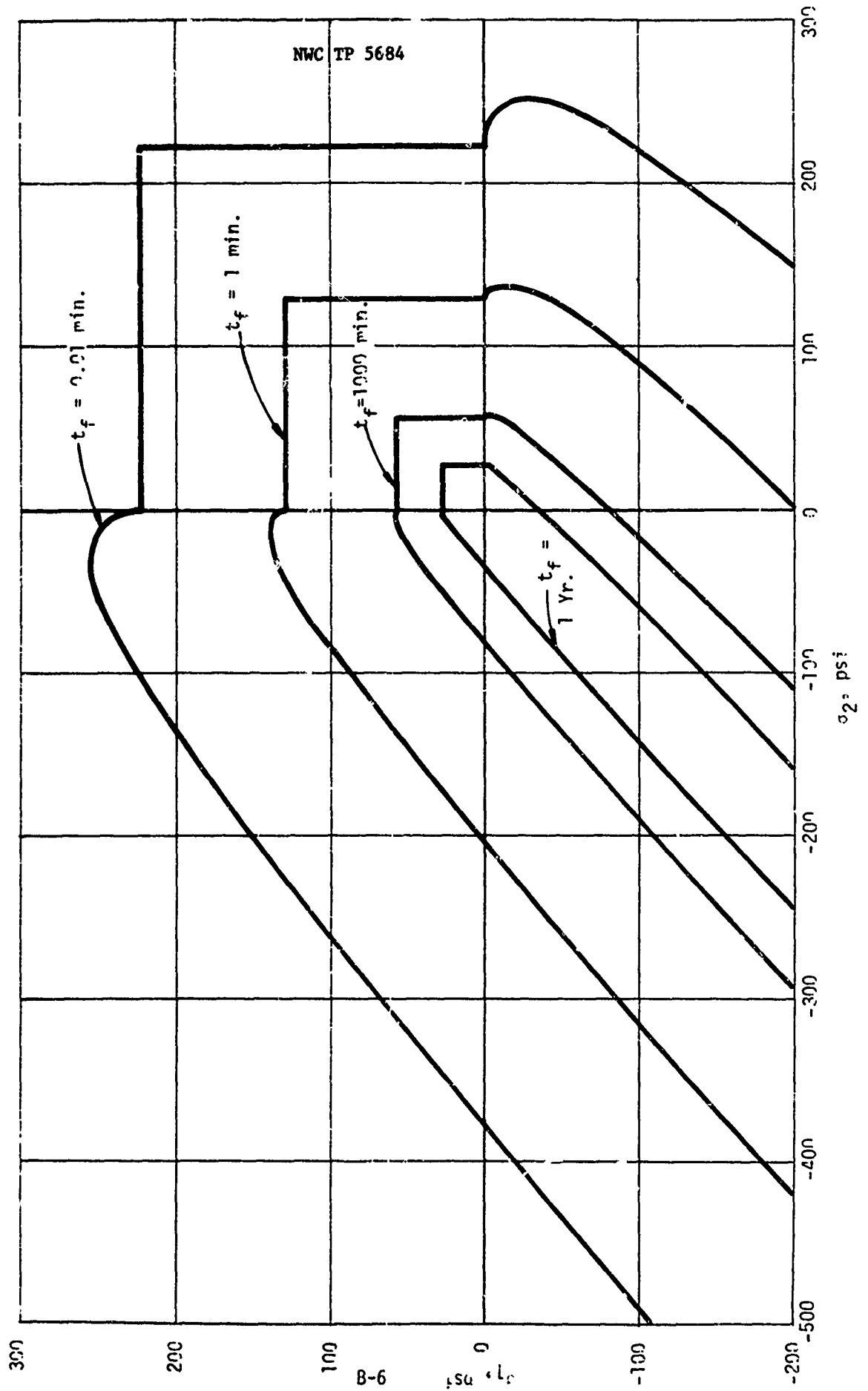


The significance of these results is best seen when they are plotted in principal stress space. The failure surface so generated is not that predicted by any of the classical theories, yet it is straightforward and easily interpreted. As a convenience in presenting the data, we shall consider the results in two-dimensional stress-space. The curves presented in Figure B-4 are crossplots from Figures B-2 and B-3 taken at discrete levels of time-to-failure under constant stress (from 0.01 min. to 1 year). Each curve represents the propellant failure criterion for a given time-to-failure.

The data in the first quadrant (where both principal stresses are tensile) are typical of the classical, maximum principal stress failure criterion. It is considered reasonable that this should be the case, since the propellant is highly dewetted prior to failure. Hence, the lateral stresses should have only minor effects upon the behavior of the propellant.

In the second and third quadrants, a surprising effect is observed. Under small compressive stresses, the strength of the propellant actually increases. This is clearly evident in the curve for the time-to-failure equal to 0.01 min., where it is seen as a marked "shoulder" on the failure surface. This shoulder occurs at each of the failure times, but is less evident at the longer times. The shoulder, in Figure B-4, is believed to occur because of an interaction between the dewetting process and the superimposed hydrostatic pressure. In the tensile quadrant, the propellant is extensively dewetted before failure. In the second quadrant, the addition of hydrostatic pressures acts to suppress dewetting. Extension of this argument suggests that dewetting will be suppressed with increasing hydrostatic pressure until, at least asymptotically, the dewetting will be completely eliminated prior to propellant failure.

Figure B-4. TWO DIMENSIONAL REPRESENTATIONS OF EXPERIMENTALLY DERIVED FAILURE CRITERIA FOR THE STV PROPELLANT AT 77°F
(At Constant Times to Failure)



By this sort of reasoning, it is possible to define the maximum uniaxial strength that the propellant might have achieved if dewetting had not occurred. As shown in Figure B-5, extrapolation of the estimated pressure-defined asymptote back to 0 psig pressure gives a uniaxial strength of 340 psi for the undewetted propellant. The dewetted propellant was found to have a strength of only 224 psi, which is about 66% of its potential strength. Thus, dewetting decreased the strength of this propellant about 34% for a time to failure of 0.01 min. The percentage reduction in strength was found to be about the same at all times-to-failure, see Table B-1.

In this section we have presented a propellant failure criterion with one possible interpretation for the mechanisms involved. The next section presents some data which suggest a different mechanism for the processes involved.

2. The Effect of Superimposed Pressures on Vacuole Formation

Farris (B-6,B-7) has shown that the effect of superimposed pressures is to delay the onset of vacuole formation. Figure B-6 was reproduced from Reference B-6, to demonstrate how increasing pressures appear to suppress the dewetting processes. An anomaly exists here, since the suppression of dewetting would be expected to make the propellant behave more rigidly and exhibit marked reductions in failure elongation. However, the opposite seems to be true, the elongation at break increasing with increasing pressure. Thus, the failure process appears to be one where (a) dewetting occurs, but because of the superimposed pressure, the vacuoles are suppressed and (b) the stretching mechanism of the propellant is restricted to local shearing processes.

Figure B-5. EXTRAPOLATION OF ESTIMATED ASYMPTOTE TO 0 PSIG
TO DEFINE UNDELETED PROPELLANT STRENGTH
(Time-to-Failure: 0.01 min.)

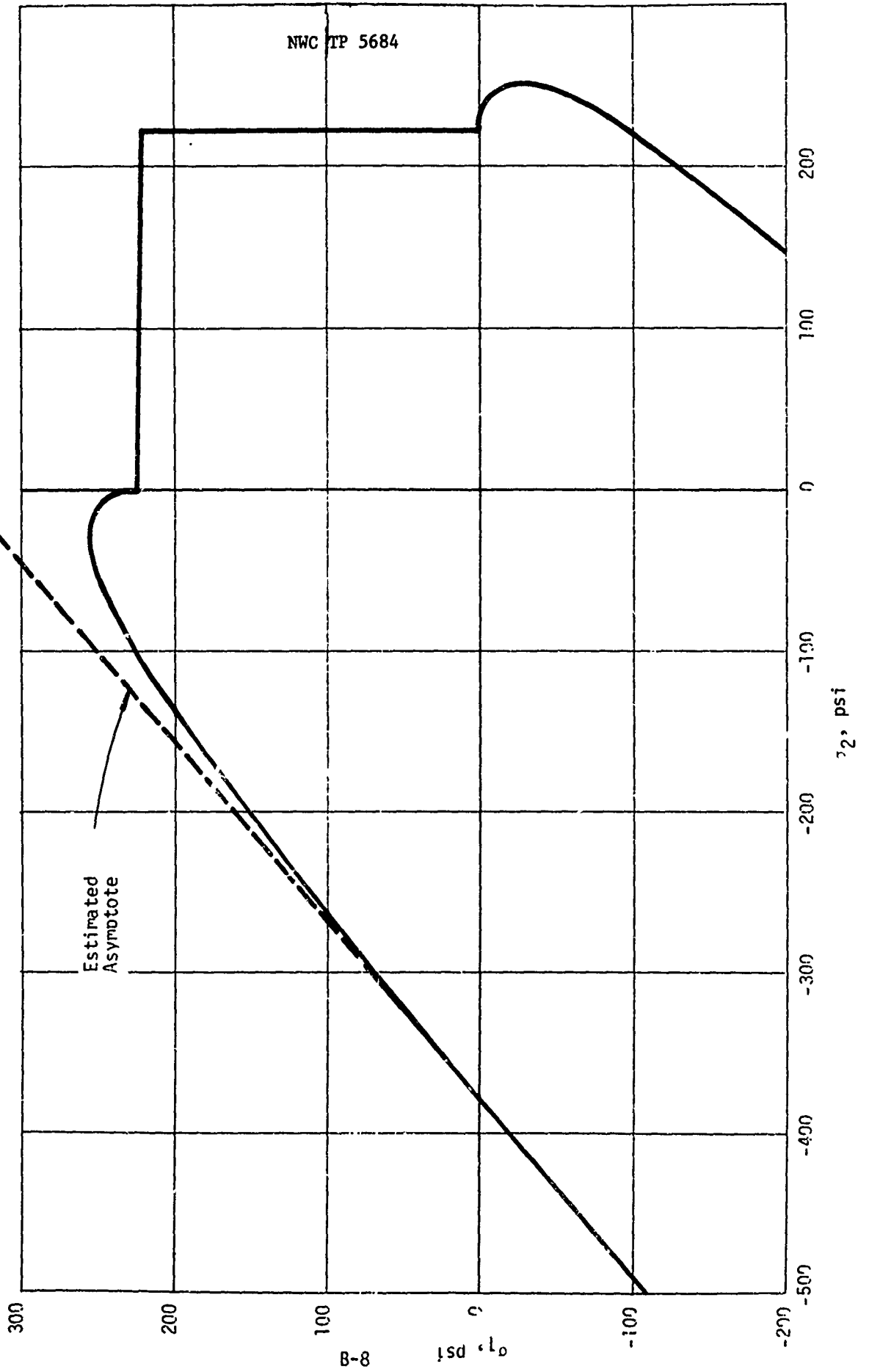


TABLE B-1

COMPARISON OF OBSERVED PROPELLANT DEWETTED STRENGTH WITH
THOSE ESTIMATED FOR THE UNDEWETTED MATERIAL

<u>Time-to-Failure</u>	<u>Estimate of Undewetted Strength, psi</u>	<u>Observed Dewetted Strength</u>	
		<u>Strength, psi</u>	<u>Percent of Estimated Strength</u>
.01 Min.	340	224	66
1 Min.	192	130	68
1000 Min.	86	58	68
1 Year	41	27.6	67

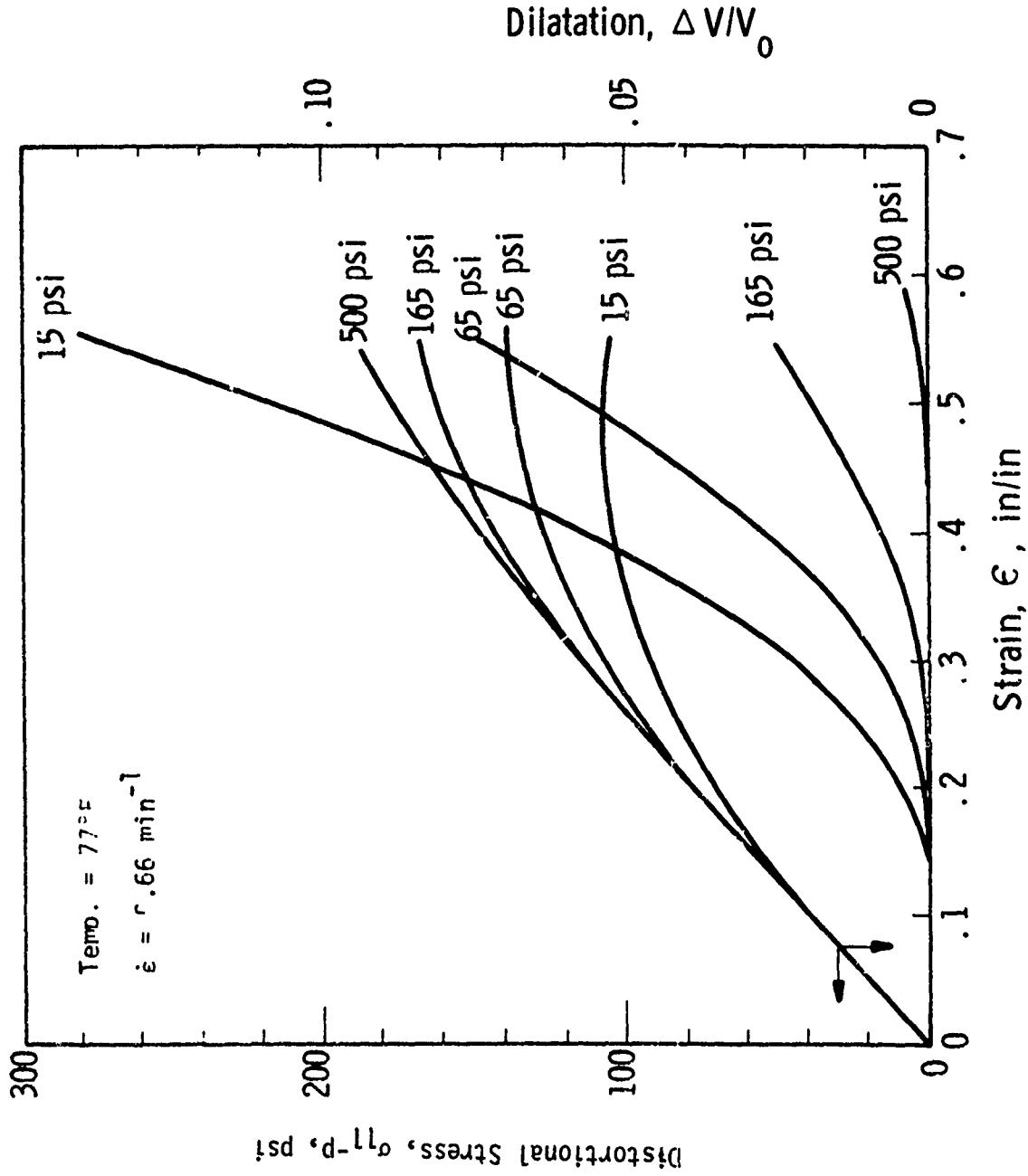


Figure B-6. COMPARISON OF THE STRESS-STRAIN AND DILATATION-STRAIN BEHAVIOR OF A HIGHLY FILLED ELASTOMER (65 Vol. %) AT A SERIES OF HYDROSTATIC PRESSURES

In summary, it appears that the propellants may fail: (1) by a maximum principal stress failure criterion at ambient pressure; and (2) by a shear failure criterion under hydrostatic pressures. The transition from one criterion to the other, as described earlier, may be restricted to a fairly narrow range of pressures.

REFERENCES TO APPENDIX B

- B-1 Bills, K. W., Jr., et. al., "Solid propellant Cumulative Damage Program", Report No. AFRPL-TR-68-131, pages 33 to 45 (October 1968).
- B-2 Bills, K. W., Jr., Peterson, F. E., and Steele, R. D., "Study of Cumulative Damage Techniques for the Prediction of Motor Failure", Aerojet-General Corporation Report No. 4158-81F, Contract No. NOW 66-0545-c (July 1967).
- B-3 Bills, K. W., Jr., Peterson, F. E., Steele, R. D., and Sampson, R. C., "Development of Criteria for Solid Propellant Screening and Preliminary Engineering Design", Aerojet-General Corporation Report 1159-81F, No. N00017-67-C-2415 (December 1968).
- B-4 Bills, K. W., Jr., Campbell, D. M., Steele, R. D., and McConnell, J. D., "Applications of Cumulative Damage in the Preparation of Parametric Design Curves and the Prediction of Grain Failures on Pressurization", Aerojet Solid Propulsion Company Report No. 1341-26F, Contract No. N000-17-69-C-4423 (July 1970).
- B-5 Bills, K. W., Jr., Campbell, D. M., Sampson, R. C., and Steele, R. D., "Failures in Grains Exposed to Rapid Changes of Environmental Temperatures", Aerojet Report 1236-81F, Contract N00017-68-C-4415 (September 1969).
- B-6 Farris, R. J., "The Character of the Stress-Strain Function for Highly Filled Elastomers", Trans. Soc. of Rheol., 12, 303-314 (1968).
- B-7 Farris, R. J., "The Influence of Vacuole Formation on the Response and Failure of Filled Elastomers", Trans. Soc. of Rheol., 12, 315-334 (1968).